ALMA MATER STUDIORUM - UNIVERSITA' DI BOLOGNA

DOTTORATO DI RICERCA IN
MECCANICA E SCIENZE AVANZATE DELL'INGEGNERIA

Ciclo XXIV

Settore Concorsuale: 09/A3
Settore Scientifico Disciplinare: ING-IND/21

DESIGN AND OPTIMIZATION OF COMPONENTS AND PROCESSES FOR PLASMA SOURCES IN ADVANCED MATERIAL TREATMENTS

Ing. Fabio Rotundo

Coordinatore
Prof. Ing. Vincenzo Parenti Castelli

Relatore
Prof. Ing. Vittorio Colombo

Co-Relatore
Prof. Ing. Lorella Ceschini

Esame finale Anno 2012

INDEX

ABSTRACT

The research activities described in the present thesis have been oriented to the design and development of components and technological processes aimed at optimizing the performance of plasma sources in advanced in material treatments.

In the first part of the present work, consumables components for high definition plasma arc cutting (PAC) torches were studied and developed. Experimental activities have in particular focussed on the modifications of the emissive insert with respect to the standard electrode configuration, which comprises a press fit Hafnium (Hf) insert in a copper body holder, to improve its durability. Based on a deep analysis of both the scientific and patent literature, different solutions were proposed and tested. First, the behaviour of Hf cathodes when operating at high current levels (250A) in oxidizing atmosphere has been experimentally investigated optimizing, with respect to expected service life, the initial shape of the electrode emissive surface. Moreover, the microstructural modifications of the Hf insert in PAC electrodes were experimentally investigated during first cycles, in order to understand those phenomena occurring on and under the Hf emissive surface and involved in the electrode erosion process. Thereafter, the research activity focussed on producing, characterizing and testing prototypes of composite inserts, combining powders of a high thermal conductibility (Cu, Ag) and high thermionic emissivity (Hf, Zr) materials, aimed at improving the electrode endurance performances.

The complexity of the thermal plasma torch environment required and integrated approach also involving physical modelling. Accordingly, a detailed line-by-line method was developed to compute the net emission coefficient of Ar plasmas at temperatures ranging from 3000 K to 25000 K and pressure ranging from 50 kPa to 200 kPa, for optically thin and partially auto-absorbed plasmas.

Finally, prototypal electrodes were studied and realized for a newly developed plasma source, based on the plasma needle concept and devoted to the generation of atmospheric pressure non-thermal plasmas for biomedical applications.

Part of the experimental results have been published in:

- V. Colombo, A Concetti, E Ghedini, F. Rotundo and S Dallavalle, *Experimental analysis of the behaviour of high current electrodes in plasma arc cutting during first cycles*, Plasma Sources Sci. Technol. 19 (2010) 065023-1 - 065023-9

- G. Cantoro, V Colombo, A Concetti, E. Ghedini, P. Sanibondi, F. Zinzani, F. Rotundo, S. Dallavalle, M. Vancini, *Plasma arc cutting technology: simulation and experiments*, Journal of Physics:Conference Series 275 (2011) 012008

- V. Colombo, A. Concetti, E. Ghedini, F. Rotundo, P. Sanibondi, M. Boselli, S. Dallavalle, M. Gherardi, V. Nemchinsky, M. Vancini, Advances in Plasma Arc Cutting Technology: The Experimental Part of an Integrated Approach, Plasma Chem. Plasma Process. DOI 10.1007/s11090-011-9338-8 (2011)

Part of the experimental results have been presented and included in proceedings in:

- V. Colombo, A. Concetti, E. Ghedini, S. Dallavalle, M. Vancini, F. Rotundo, C. Chiavari, *Experimental analysis of the behaviour of high current electrodes in plasma arc cutting during first cycles*, 19th International Symposium on Plasma Chemistry (ISPC 19), Bochum, 2009

- G. Cantoro, V. Colombo, A. Concetti, E. Ghedini, P. Sanibondi, F. Zinzani, F. Rotundo, S. Dallavalle, M. Vancini*, Plasma arc cutting technology: simulation and experiments*, 11th European Conference on High-Technology Plasma Processes (HTPP 11), Brussels, 2010

- V. Colombo, A. Concetti, E. Ghedini, F. Rotundo, P. Sanibondi, S. Dallavalle, M Vancini. (2010). *Plasma arc cutting technology: simulation and experiments*. International Conference on Gas Discharges and Their Applications (GD 2010), Greifswald, 2010

- V. Colombo, A. Concetti, E. Ghedini, F. Rotundo, P. Sanibondi, S. Dallavalle*, Advances in plasma arc cutting technology: the experimental part of an integrated approach*, 20th International Symposium on Plasma Chemistry (ISPC 20), Philadelphia, 2011

CHAPTER 1

PLASMA ARC CUTTING

1.1. INTRODUCTION

1.1.1. BASICS OF THERMAL PLASMAS

Gageous plasmas consist of a mixture of neutral particles, ions, and electrons. Due to its high energy content, it is often defined as the fourth state of matter. Since neutrals and ions are much heavier than electrons, they are referred to as heavy particle. These particles can assume different energetic configuration in such a mixture, being either in the ground state or in an excited state. A fundamental property which qualifies such a mixture as a plasma is the *quasi-neutrality*, which represents the apparent charge neutrality of a plasma overall, while, at smaller scales, the positive and negative charges may give rise to charged regions and electric fields. Another way to express the *quasi-neutrality* condition is [1]:

$$|n_e - n_i| << n_e \qquad (1.1)$$

with n_e and n_i representing respectively the number of positive and negative charges. Differently from an ordinary gas, the presence of free charge carriers (electrons and ions) makes plasma a conducting fluid.

As in any gaseous medium, kinetic temperatures in a plasma are defined by the average kinetic energy of different particles (electron, ion, atom or molecule):

$$\frac{1}{2}m\bar{v}^{2} = \frac{3}{2}kT \qquad (1.2)$$

where m is the particle mass, $(\bar{v}^{2})^{1/2}$ the velocity root mean square, k the Boltzmann

constant and T the absolute temperature (K). The use of Eq. 1.2 presupposes that particles velocities follow a Maxwell-Boltzmann distribution $f(v)$, which can be express as:

$$dn_v = nf(v)dv \tag{1.3}$$

$$f(v) = \frac{4}{\sqrt{\pi}}\left(\frac{2kT}{m}\right)^{3/2} v^2 \exp\left(-\frac{mv^2}{2kT}\right) \tag{1.4}$$

The establishment of a Maxwell-Boltzmann velocity distribution among species is related to the collisional frequency and the energy exchange during collisions. It is in particular in the case of a collision dominated plasma, where, due to the species energy exchange, heavy species and electrons among themselves will have a Maxwell-Boltzmann distribution.

Electric discharge is the most common mean to generate and maintain a plasma: the highly mobile electrons harvest energy from the discharge electric field and transfer part of it to the heavy particle through elastic collisions. Due to the high differences in mass between heavy species and electrons, many collisions are required to eliminate temperature (or kinetic energy) differences, since:

$$\Delta E_{kin} \cong \frac{2m_e}{m_h} \approx 10^3 \tag{1.5}$$

The more the energy collisional transfer is efficient, the lowest the difference between electrons and heavy particles temperature will be. However, even with excellent collisional coupling (high collision frequency), there will always be a difference in electrons and heavy particles temperature (respectively T_e and T_h). Nevertheless, a plasma can be considered in kinetic equilibrium ($T_e = T_h$) if the energy the electrons pick up from the electric field between one collision and the following one is very small when compared to the mean electron kinetic energy. Since the pressure p is proportional to particle density n, i.e. inversely proportional to the electron mean free path (λ_e), and the electric field intensity E is proportional to the energy acquired by the electron between two collisions, the parameter E/p is an indication of the kinetic equilibrium between species. In particular, for small values of E/p, the electron temperature approaches the heavy particle temperature. This condition, united with

chemical equilibrium as well as certain limitations on the gradients in the plasma, constitute the basics requirements for Local Thermodynamic Equilibrium (LTE).

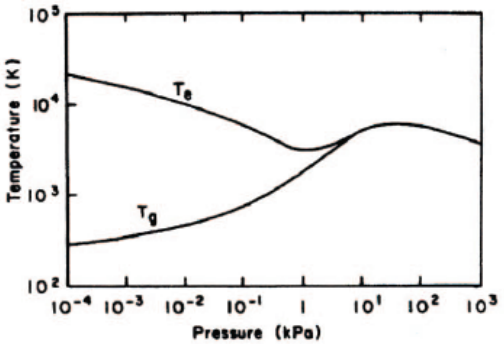

Fig. 1.1 Behaviour of electron temperature (T_e) and heavy-particle temperature (T_h) in an arc plasma [1].

Those plasmas satisfying simultaneously the kinetic equilibrium which are in (or close to) LTE conditions are commonly defined as *thermal plasmas*, i.e. the electron temperature approaches the heavy particle temperature, the velocity distribution function follows a Maxwell-Boltzmann distribution and the population density of the excited states follows a Boltzmann distribution. In thermal plasmas, composition is described by the Saha equations, which must be considered a mass action law. Plasmas are typically classified according to electron density and temperature (Fig. 1.2). Thermal plasmas are usually characterized by E/p of about 1 V/(m-kPa) (usually p>0.1 MPa), electron temperatures in the order of 10^4 K and electron densities ranging from 10^{21} to 10^{26} m^{-3}.

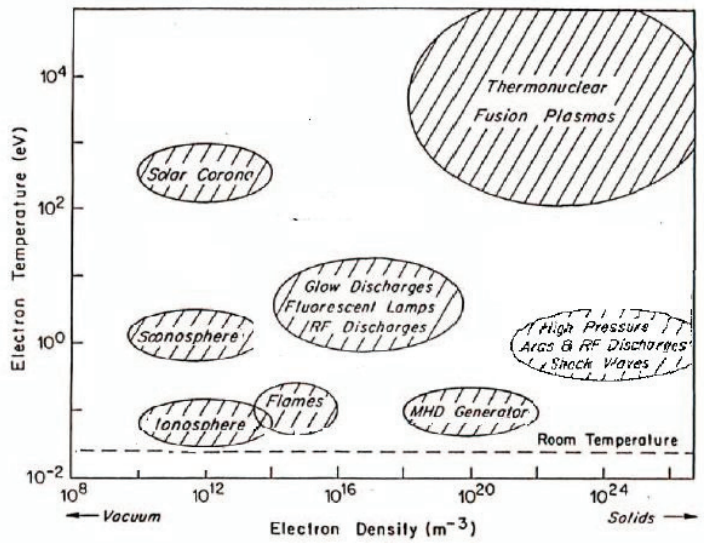

Fig. 1.2 Classification of plasmas [1].

Since gases are insulators at room temperature, in order to make the gas electrically conducting it is necessary to induce an electrical breakdown, i.e. to generate a sufficient number of free charge carriers. Typical thermal plasmas discharges can be sorted into [1]:

- *high intensity arcs*, characterized by a DC current (I > 50 A) flowing through two electrodes (cathode and anode) at pressure p>10 kPa;

- *thermal RF discharges*, characterized by a time varying magnetic field, generated by a coil surrounding the plasma, which maintains the discharge; they are classified as inductively coupled plasma, or *H* discharge, in contrast to the *E* discharge, where the discharge is maintained by an high-frequency electric field, not well suited for thermal plasmas generation;

- *microwave discharges*, where the discharge is sustained by a electromagnetic waves, with typical frequency ranging between 1 MHz and 10 GHz and pressure from 10^3 Pa to several hundreds kPa.

High intensity arcs, which are of particular interest for the present work, are characterized by a steep potential drops in front of the electrodes, and relatively small potential gradients in the arc column. Thus, the arc can be divided into three parts: the cathode region, the anode region, and the arc column. Only in the latest, plasma conditions approach a LTE state.

The electrical neutrality of a plasma is especially valid for thermal plasmas which are characterized by relatively high charge-carrier densities. Charge imbalances within a plasma are restricted to regions of the order of the so called Debye length [1]. Imbalances of charges can also arise in regions in the vicinity of a solid or liquid boundary, e.g. on plasma-confining walls, on electrodes and around probes. Those regions are named *plasma sheaths.*

1.1.2. METAL CUTTING THROUGH THERMAL PROCESSING

Common cutting processes used in today's manufacturing industries can be sorted in two main families: mechanical cutting and thermal cutting. The former includes those

technologies involving removal of material by mechanical action of a power-driven tool, in contact with the workpiece; the latest exploits heat generation to melt the material and momentum of a gas flow to remove it. In thermal processing, cut quality depends upon final geometry, dross formation and material deformation as a consequence of the thermal cycling. Further that cut quality, fundamental parameters which drive the choice of a particular cutting technology are productivity and related costs. Thermal cutting processes include *laser cutting*, *oxy-fuel cutting* and *plasma arc cutting*.

In *laser cutting*, a laser beam impinges on the workpiece in order to heat and sever it. The energy transfer to the workpiece occurs by means of monochromatic photons constituting the beam, which is focalized though a lens between the generator and the workpiece. The controlled spot of the laser beam allows for very high energy density (typically 10^6 – 10^8 W/cm^2) and narrow cuts. Part of the material is vaporized and removed by means of a flux of working gas. CO_2 lasers are among the most common and powerful lasers in use today. Despite its relatively recent introduction in industrial thermal cutting, it owns an important market share. Main limitations are high costs, power efficiency and non-transportability of the beam (i.e. of the lens system), and limitations on maximum cutting thicknesses. All materials, conducting and non conducting, can be treated with this technology.

Oxy-fuel cutting technology made its apparition in industrial cutting over a century ago. Main application is steel cutting, since the process is facilitated by the exothermic oxidation reaction:

$$2\ Fe + O_2 \leftrightarrow FeO + 274.6\ kJ/mol \qquad (1.5)$$

Since this reaction occurs between 1600 K and 1800 K, oxygen-acetylene preheat flames are used to raise the surface of the workpiece. Pure oxygen is then made to impinge the heated area in a high pressure stream. Only low carbon steels can be cut with this technology, with thickness varying from 10 mm to 1500 mm. After cutting, the workpiece is characterized by strong thermal distortion and uneven walls, making further machining often necessary.

In *plasma arc cutting (PAC)*, a plasma jet is formed between a cathode, inside the

plasma torch, and an anode. Both conducting and insulating materials can be treated: for the formers, the workpiece act as an anode and the plasma arc its transferred to it; for the latest, a non-transferred configuration is adopted, in which the torch comprises the anode and the plasma is internally generated then directed toward the workpiece, with delivered energy density usually ranging between 10^5 and 10^6 W/cm^2.

PAC occupies in many respects an intermediate position in between its main competitors [2]: oxy-fuel and laser cutting (Fig. 1.3). The plasma process is generally faster than the other methods, except than for very high thicknesses (>100 mm), where oxy-fuels shows higher velocities and maximum thickness capacity (up to 150 mm), although PAC cutting quality is superior. For medium thickness (3-20 mm) laser needs very high power and, due to poor energy transfer efficiency, high operating costs. Maximum thickness for laser cutting are of the order of 25 mm. On the other hand, oxy-fuel cutting produces very high thermal deformation for this thickness range, resulting in low cutting quality.

For thin plates, laser cutting quality is still higher. Nevertheless, through fine regulation of currents and jet diameter, PAC is becoming a competitor by increasing itscutting quality, so that high-precision cuts are often referred to as “laser like”. Moreover, the equipment and operating costs of PAC are intermediate between very expensive lasers and the cheap equipment for oxy-fuel cutting.

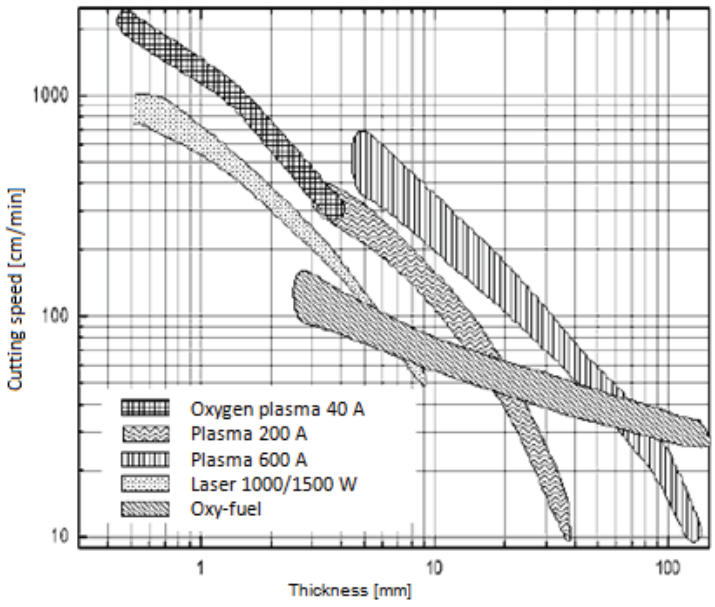

Fig. 1.3 Mild steel cutting velocities for different thermal processes [3].

Summing up, PAC often represents the best compromise between cost, productivity and cut quality, competing with laser for low thickness and with oxy-fuel for large thickness. There is a wide range of different PAC systems, from relatively simple, light manual systems designed to be used in small shops, working at relatively low current (not exceeding 120 A), to powerful systems, coupled with CNC cutting machines and controls for mechanized cutting, using very high currents (up to 400 A for oxygen cutting and to 1000 A for argon–hydrogen mixture cutting).

PAC is nowadays a widely used industrial process to cut different metals in different and elaborated shapes. R&D programs on PAC aim at increasing maximum thickness and separable materials range, cutting velocity, quality and productivity.

1.2. PLASMA ARC CUTTING OVERVIEW

1.2.1. THE CUTTING PROCESS

In plasma arc cutting process, a workpiece is severed by using a constricted arc to melt a localized area, removing the molten material with a high-velocity jet of ionized gas issuing from a constricting nozzle. As anticipated, in PAC processes a transferred arc is established applying a voltage difference between the cathode and the workpiece, acting as anode. Fig. 1.4 shows the main gas and water flows involving a PAC torch in a common configuration.

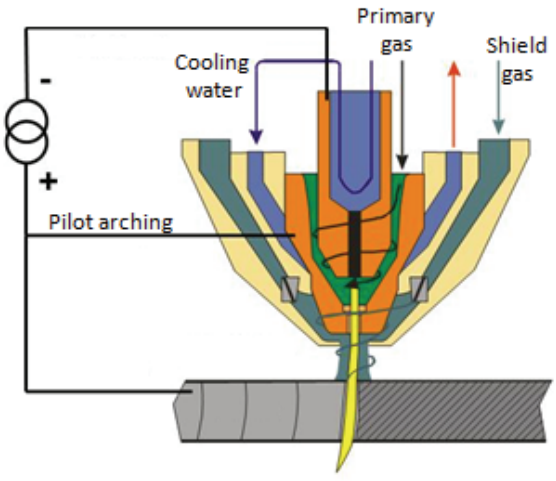

Fig. 1.4 Standard configuration for a a PAC torch.

A primary gas, to be ionized, flows around the electrode and exit through a constricted opening. The constricting action is accomplished through a water cooled nozzle. The arc constriction is essential to increase the arc temperature and to achieve the desired energy density. A secondary flow is in charge of protecting the nozzle from molten metal drops, originating from the workpiece. This gas exit through an another water cooled component, named shield, which also protects the nozzle and obstacles the establishment of double arching (electrode-nozzle-workpiece) phenomena.

The cutting procedure comprises different phases and arc configurations, reported respectively in Fig. 1.5 and Fig. 1.6, which will be described in the following paragraphs.

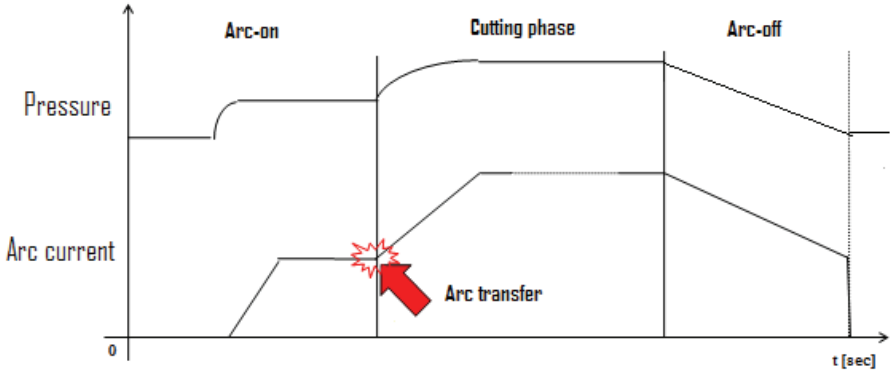

Fig. 1.5 Typical PAC cycle.

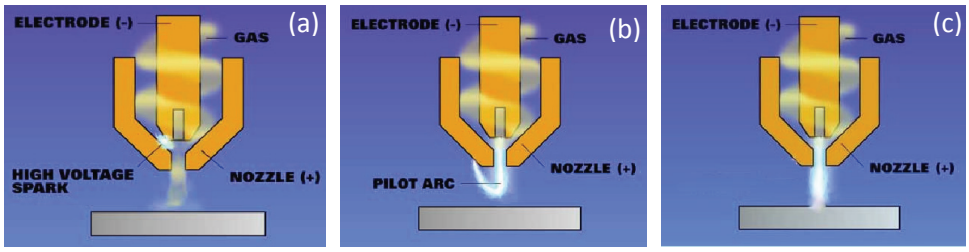

Fig. 1.6 (*a*) Arc ignition; (*b*) pilot arching and (*c*) arc transfer.

Arc ignition

Arc ignition starts with igniting a pilot arc: namely, an arc discharge between the electrode (cathode) and the nozzle. The ignition is usually achieved by means of short high frequency (HF) high voltage pulse applied between the two abovementioned components. Once a channel of ionized gas is established in correspondence of the minimum distance between them, a continuum voltage is applied, establishing the pilot arc.

Arc transfer

Once the pilot arc is established, a primary gas flow pushes the pilot arc out of the nozzle, first creating an arc loop protruding out of the nozzle (Fig. 1.6 *b*), and then, provided the workpiece is at suitable distance and at the same voltage of the nozzle, the arc transfers to it. Simultaneously, the cathode arc attachment moves to the centre of the cathode; power supply controls are designed to recognize the transfer event and, consequently, to exclude to nozzle from the circuit, which now closes through the workpiece acting as anode.

Cutting phase

Once arc transfer is accomplished, the arc current is gradually increased from the relatively low pilot arc values to the nominal values. At the same time, the gas passing from the primary channel is switched from the starting one (nitrogen for instance), to a different one (air or oxygen for steel cutting). The gas pressure is also increased gradually, together with current, to limit cathode erosion phenomena, as later described.

The cutting phase can start from the edge of a plate, or, when necessary due to the workpiece shape or other machining reasons, by piercing the plate, before moving the torch (manually or through CNC control) to obtain the desired cut geometry. During piercing, molten metal deposits on top of the plate, threatening to bridge the torch and the workpiece with the risk of welding them together. Further potential damage for the torch comes from molten droplets flying upwards. As a consequence, during piercing, the torch-to-plate distance (*stand-off*) is increased with respect to the standard one, which is maintained during the remaining cutting phase. Moreover, a shield gas (or secondary gas) is blown toward the plate to protect the torch from flying droplets both during piercing and moving cut phases (Fig. 1.4).

During cutting, the primary gas is supplied with a tangential component through a swirl ring, aiming at stabilizing the arc position and increasing cut quality. Indeed, the tangential component of the swirl pushes colder gas particles to the external part of the jet due to centrifugal forces, concentrating the hot plasma in the jet centre. This, together with the constriction induced by the nozzle orifice, contributes to stabilize the arc and to achieve higher current density in the arc centre, and, consequently, higher temperature and energy density, which are required for high definition cuts. A contribution to this phenomenon, which is called thermal pinch and causes the arc

column to contract, can also be supplied by the cold secondary gas. In the hot region, electron concentration measurements showed that the plasma is close to the LTE, although in some region close to the work-piece the electron concentration was found to be higher than the corresponding LTE value [2].

The hottest central zone, characterized by a high electric conductivity and hence responsible for carrying the electric current, possesses low density and, as a consequence, generates negligible mass flow. In view of its temperature, the relatively cold zone wrapping the plasma column is not-conducting. On the other hand, it is responsible for most of the mass flows and momentum necessary to remove the molten material.

The choice of arc currents, gas types and pressure, stand-off and cut velocities depends upon materials and thicknesses to be cut. In industrial automatic cutting, the stand-off is controlled in retro-action by monitoring the arc voltage.

Arc-off phase

Once cutting is finishes, the arc current and pressure are gradually decreased to zero. This phase, as well as the arc transfer phase (or arc on) phase, is particularly important for electrode erosion phenomena, as later discussed.

1.2.2. CUTTING QUALITY

The ISO9013 norm [4] defines the standards of the so called *high definition* in thermal cutting quality. It can be applied to oxy-fuel, laser and plasma arc cutting, respectively in the 3 - 300 mm, 0.5 – 40 mm and 1 – 150 mm thickness ranges. The norm indentifies in particular the parameters to be used to evaluate the effects of thermal cutting and the respective measure procedures to be applied.

Specifically, the norm defines the *cutting speed* as relative velocity between the torch and the workpiece; *kerf width* as the distance between separated surfaces at the upper edge of cut; *drag* as the projection of the distance between the two points of a drag line in the cutting direction.

The norms sets in particular specific limits concerning the following geometrical features of the machined workpieces: perpendicularity or angularity tolerance; profile element height; melting of top edge (rounding at the top of the cut); gouging (presence

of scourings or kerves of irregular width).

Influence of cutting speed

The speed at which the plasma torch moves has a strong influence on cut quality. Over a maximum velocity U_{max}, incomplete cut penetration would be obtained. This velocity depends upon plate thickness, nozzle orifice diameter (hence plasma column diameter) and arc current. At lower U values, but still approaching U_{max}, the cut would be complete but part of the material would stuck on the bottom of the plate, as the gas flow would not have enough time to remove it, giving rise to the so called "high velocity dross" and thus requiring further machining. On the other hands, despite lower U values would in general allow for better cut perpendicularity, too low cutting speeds would result in low velocity drosses, as a larger portion of the workpiece would be molten, and the cutting kerf would become too wide.

It is then clear that satisfying cut quality is achieved only when the cutting speed stays inside an interval said *dross free window*. This interval gets narrower as the plate thickness increases, while, on the other side, it increases with higher arc currents, which unfortunately results in higher cathode erosion and consequently shorter consumables working life. The dross free interval is also influenced by the work-piece chemical composition. Typical cutting speed for mild steel thick plates is in the order of 20 mm/min.

Bevel angle

The Bevel angle (β) is the one indentified between the cut wall and the direction perpendicular to the cutting plane (Fig. 1.7). 0° Bevel angle represents a straight cut, which cannot be obtained in common practice with this technology. The top of the kerf is usually wider than its bottom. Moreover, since the swirl component is usually clockwise, the tangential velocity of the flow sums with the one of the torch on the left side, and the cut is not symmetric, i.e. angles β_{left} and β_{right} are not equal.

Typical Bevel angles for PAC are of 1-3° for the best side and 4-8° for the worst side. Positive Bevel angle can be related to conditions like too high stand-off or cutting speed, low arc current and eroded nozzle. In this configuration, the arc supply the majority of its energy to the upper part of the workpiece, creating a wider *kerf* in this zone. Negative Bevel angles, on the other hand, can be related to low stand-off and

cutting speed, too high arc current, as the plasma jet would have the possibility of melting a greater amount of material from the bottom of the plate.

The case of positive and negative Bevel angles can be the signal of strong damage of the nozzle, which may have lost its symmetry, or misalignment of the nozzle and electrode.

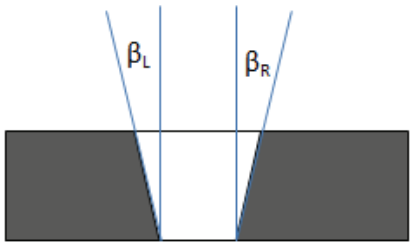

Fig. 1.7 Bevel angles.

Gas management

At industrial level, the choice of the primary/secondary gas combination is driven by the possibility of having the best possible compromise among cut quality, cutting speed and operational costs. Moreover, the gas combination strongly depends upon the materials to be cut. Most common gases are air, oxygen, nitrogen and argon-hydrogen mixtures.

Although it needs to be de-hydrated, filtered and compressed, air is the most cheap working gas. Good cutting velocity and quality can be reached with stainless steel, mild steel and aluminium, but oxides and nitrides can cause strong porosity on the cut walls and worsen the materials weldability. Rather than as primary gas, it is often adopted ad shied gas. Typical lifespan of consumables components in this configuration is of the order of 600 cuts.

The industrial standard for cutting mild steel, which represents the main market for PAC, is to use oxygen/air respectively as primary/secondary gas. This configuration allows for the best cutting quality and cutting speed, also due to the exothermic reaction between iron and oxygen (Eq. 1.5). This plasma configuration produces in fact a fine dispersion of iron oxide particles, with low surface tension, easy to be expelled from the kerf. Main drawbacks are higher costs and strong erosion of the electrode. The use of N_2 at arc ignition is suggested to prolong the electrode life. Superior and cutting speed and cut quality (i.e. no or less post-cut machining required), justifies the use of oxygen despite its higher costs.

N_2 is the most commonly used primary gas for cutting aluminium and stainless steels up to 15 mm thickness, due to good cut quality and excellent consumables durability it provides. It is usually coupled with air as secondary gas. Alternative shield gas are CO_2, which gives better surface finishing but has higher costs, or water, allowing for smooth surfaces. For higher thicknesses, the H35 (35% H2, 65%Ar) mixture is adopted as resulting plasma achieves higher temperatures, resulting also in better surface quality and straight cuts, although security requirements for this gas mixture are higher. N_2 is typically used as secondary gas with the H35 mixture.

1.2.3. CONSUMABLE COMPONENTS FOR A PAC TORCH

Main components of a plasma torch are illustrated in Fig. 1.8. One can distinguish the torch body, which holds the power supply, gas and water and connections, and a series of components which faces or are very close to the plasma environment: the electrode (cathode), the nozzle and the shield, further than gas diffusion rings. These components are the so called "consumables" since, due to their interaction with the plasma, they undergo modifications at subsequent cutting cycles which make their periodic substitution necessary.

Materials specification and geometry depends on plasma current and operating gas, i.e. on materials and thickness to be cut, especially in high definition PAC. Some specifications of PAC torches consumables are given below.

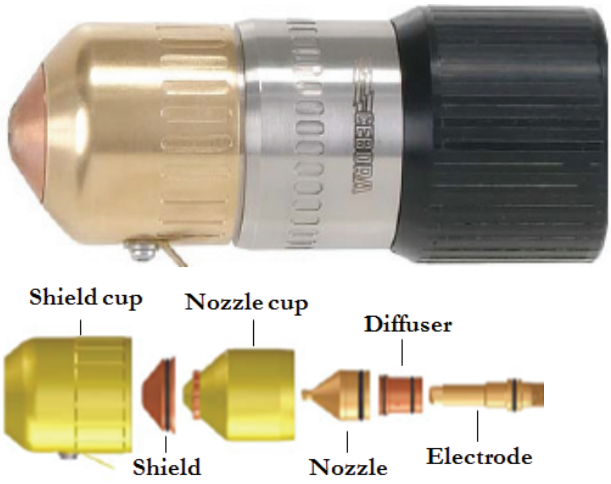

Fig. 1.8 PAC torch (Mod. Cebora CP250G) and relative consumable components.

Cathode (Electrode)

The cathode (generically referred to as the electrode) is the heart of the PAC torch: it supplies the electrons necessary to sustains the arc, mainly through thermoionic emission. Due to the temperatures and pressure fields it faces during cutting and transient phases, this component suffers significant erosion phenomena which limit its in-service life, especially when operated in oxidizing atmospheres. Should the cathode work improperly, the cutting quality would be immediately deteriorated.

Conventional plasma electrodes comprise a water cooled tubular holder machined from a high thermal conductivity material, and an emissive insert facing the plasma chamber and characterized by a relatively low work function. The former has the main duty of conducing electricity towards the insert and removing heat from it. Commonly used materials for the electrode body are copper (Cu), cooper alloys, silver (Ag) and silver alloys.

The conventional insert material for torches operating in inert atmospheres is tungsten (W). When cutting mild steels thicker than 20 mm, oxygen or oxidizing atmospheres are widely used to improve cutting speed and cutting quality. Under these conditions, tungsten electrodes erode dramatically [2], also due to the low melting point (MP) of its oxide (WO_2, MP≈1500°C [5]), although tungsten alone has a very high melting point (about 3400° C.). Typical inserts for oxygen cutting consist of a refractory material, with a high MP and a relatively low work function (w_f) at high temperatures, such as zirconium (Zr: w_f =4.05 ± 0.1 eV [6], MP=1852°C [7]) or hafnium (Hf: w_f =3.9 ± 0.1 eV [6], MP=2222°C [7]), which forms high melting oxides (2812° C for HfO_2 [2]). At high temperature, Zr reacts with air faster than Hf: at 740 °C they show approximately the same reaction rate, whilst already at 900 °C Hf reacts with air at one-half the rate of Zr [8]. Although Hf inserts last approximately 1.5 times more than the Zr ones, their wear rate in oxygen plasma cutting is still higher than that of electrodes containing tungsten when used in an inert gas [2]. When Hf inserts are used with oxygen as working gas, the effective thermionic emitter is hafnium oxide (HfO_2). It is worth noticing that Hf oxide behaves as a thermal and electrical insulator at room temperature, whilst only in its molten state (i.e. at temperatures higher than 2812°C [2]) it shows good thermal and electrical conductivity, low work function and low vapour pressure.

Some significant physical properties of typical electrode body (Cu and Ag) and insert materials (Hf and Zr) are reported in Table 1.1.

	Cu	Ag	Hf	Zr
Crystal structure	cfc	cfc	α-hcp (<1760 °C) β-bcc (>1760 °C)	α-hcp (<862 °C) β-bcc (>862 °C)
Melting temperature (°C)	1085	962	2222	1852
Boiling temperature (°C)	2567	2163	3100	4377
Thermal conductivity (W/m K)	398 (at 27°C)	428	22.3 (at 50°C)	21.1
Electrical conductivity (% IACS)	103.06	108.4	-	4.1
Electrical Resistivity (nΩm)	16.7	14.7 (at 0°C)	351	450
CTE (µm/m K)	16.5	19	5.9	5.85
Work function (eV)	4.65 ± 0.05	4.0 ± 0.15	3.9 ± 0.1	4.05 ± 0.1

Table 1.1 Physical properties of typical materials for PAC electrodes (at room temperature if not differently specified).

Nozzle

In arc cutting, the required heat fluxes at the workpiece are typically in the range 100 - 200 kW/cm^2. This specific power requires the arc for thermal cutting to be extremely constricted, resulting in high current densities and correspondingly high temperatures in the axis of the arc, even at relatively low amperages (20 A).

In the plasma arc, the lower the temperature gets, the lower the easiness in current flow (electric conductivity) gets. If the plasma at the outer part of the discharge circumference is cooled, electrons hardly flow in there, and the current concentrates into the core part, giving rise to the thermal pinch phenomenon. To attain this effect, in the plasma torch a water cooled nozzle is used to squeeze the plasma generation into a narrow range. The resulting constricted arc is more stable and uniform than a non-constricted one, allowing for better cutting quality.

Being directly in contact with the high temperature plasma arc, the nozzle needs a high thermal conductivity. Moreover, its work function has to be low enough to allow for pilot arc ignition, but not too low in order to prevent destructive double arching. In view of these requirements, copper is a conventional material for PAC nozzles.

Gas diffusion ring

The main function of the diffusion (or "swirl") ring is to regulate the swirling action of the gas flow around the electrode, in order to centre the plasma arc and to constrict the plasma arc. Small, angled holes supply the gas with the desired trajectory. Swirl diffusion rings are typically made of ceramics or plastics.

Shield

The shield provide protection of the nozzle from the molten spatter during piercing and cutting phases. Moreover, being electrically insulated, its presence reduces the probability of double arching. A secondary gas is forced to pass between the nozzle and the shield, providing cooling of the components, further protection from molten metal droplets and better constriction of the plasma arc. Typical materials for this components are plastics, ceramics or copper.

1.2.4. LIMITS TO PAC CAPABILITY INCREASE

Together with cathode erosion, one of the phenomena that limits the increase in capability of PAC systems is double arcing. In particular, this phenomenon is known to cause catastrophic damage of the nozzle and of the electrode.

In the standard operational configuration, the nozzle is electrically neutral and the arc connects the cathode and the workpiece, whereas during a double arching, the arc divides into two: one part connecting the cathode and the nozzle, the other connecting the nozzle and workpiece. Factors that favours double arching are: high arc current, narrow and/or long nozzle orifice, low gas flow and insufficient gas swirl. Moreover, it is recognized that when consumables are used, double arching is more easily triggered. Nemchinsky et al [2] suggested the following explanation. It is experimentally verified that the higher is the arc current or the narrower the nozzle or the longer the orifice, the higher is the voltage drop inside the nozzle. For instance, with an arc current of 300 A, a nozzle orifice diameter of 0.2 cm and length of 0.5 cm, an assumed plasma electrical conductivity of 100 Ohm^{-1} cm^{-1}, (corresponding to the plasma temperature equal of about $20 \cdot 10^3$ K), the voltage drop inside the nozzle is about 50 V, even assuming that the plasma jet occupies uniformly the whole nozzle orifice cross-section. Before double arcing, equal electron and ion fluxes to the nozzle make the macroscopic total current to

this component equal to zero (the nozzle is electrically floating). However, electron collects only in a small portion of the nozzle and then flow to the remaining portion to balance to ion flux. Since the electron collecting section of the nozzle is very short with respect to the ion collecting one, the voltage drop between the metallic nozzle and the plasma at the nozzle exit reaches very high values. This voltage is applied across the cold layer that separates the hot plasma and the nozzle, preventing the arc from attaching to it. Since the thickness of the cold envelope could be very low, the strong electric field caused by the arc-nozzle voltage drop could be very close to the threshold value necessary to develop an electrical breakdown of the cold gas, facilitating double arching.

As the cathode erodes during its service life, the insert loses its starting geometry and emissive material is ejected and partly deposited on the nozzle inner surface. This facilitates double arching for different reasons. First, the electrode erosion leads to a loss of axy-symmetry of the plasma chamber, and possible cathode attachment slight shifting from the insert centre. As a consequence, the plasma jet loses in turn its axial symmetry and the cold boundary layer thickness at some location at the nozzle exit is thinner, favouring electrical breakdown. Second, the cathode erosion products, made of hafnium (metallic) and hafnium oxide (insulating), have relative low work function, which makes the arc attachment easier. Moreover, a thin film of erosion products on the nozzle surface, being small, is charged to the local floating potential, lower than the local plasma potential. Hence, the voltage across this thin film located at the nozzle exit can be almost as high as the voltage across the cold gas envelope. The resulting electric field at the edge of the inclusion can be strong enough to trigger a cold gas breakdown, although the average electric field over the clean nozzle surface is lower. To attain this effect, the deposited layer should be as thin as possible, but still non-transparent for electrons at voltages in the range of a few tens to hundred volts.

1.3. ELECTRODE EROSION

1.3.1. EROSION MECHANISMS

Cathode erosion is an outstanding challenge for many plasma arc cutting systems,

in particular when operated in oxidizing atmospheres and at high current levels (above 200 A). The industrial potential of such systems is limited by the durability of the consumable components and by the costs related to their substitution and loss of working time. The cathode is the most critical component in terms of durability. Its erosion rate increases with arc current and pressure, limiting the capabilities of the plasma cutting technology in terms of cutting speed, thickness of the workpiece and overall economy.

The Hf-based materials emitted from the cathode at the beginning of its service life deposit both on the cathode itself and on the nozzle, so possibly inducing a loss of axial symmetry of the plasma chamber, a local perturbation of heat transfer conditions and a reduction of the boundary layer thickness, with important drawbacks both on cut quality and on consumables service life. Moreover, the Hf based droplets deposited on the inner nozzle surface have relative low work function, which makes the electrical breakdown even easier [2], so inducing more easily destructive and non destructive double arcing phenomena [9].

In plasma arc systems at high currents, the refractory cathode operates by means of thermionic emission enhanced by the Schottky effect [2, 10]. Temperatures achieved during the process are determined by a balance between the heating process due to ion bombardment and cooling due to heat conduction and electron emission.

The mechanisms involved in the erosion phenomena of a PAC cathode have yet to be fully understood, together with factors that positively or negatively influence the erosion rate. It is known that total cathode erosion results from the different contribution of *constant current erosion* in steady states and *cyclic erosion* during transients [2, 11, 12], and brings to the formation of a crater or cavity in the insert. Since the catastrophic electrode failure occurs at some specific crater depth, it is often convenient to express the cathode erosion in terms of cathode cavity depth.

One possible explanation is that when the torch is used with an oxidizing gas such as oxygen or air, the gas tends to rapidly oxidize the copper. As the copper oxidizes its work function its believed to decrease [2] and, at relevant cavity depth, oxidized copper begins to support the arc (Fig. 1.9). As a result, copper melts, resulting in early destruction and failure of the electrode

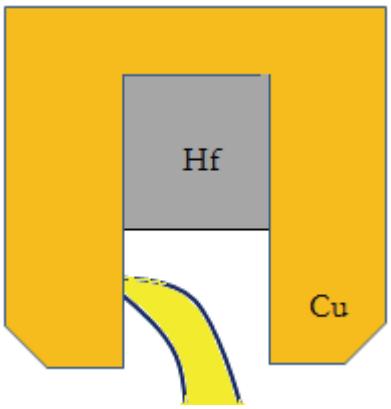

Fig. 1.9 Schematic of arc attachment to the copper body holder internal walls.

Before analyzing the different erosion mechanisms, a description of the forces acting on the molten pool is required.

Forces on the molten pool

Droplet ejection is believed to be the main cause of cathode erosion [2, 12]. Droplets form and are ejected as a consequence of the different forces acting on the molten hafnium pool.

According to a model proposed by Peters et al [12], the molten pool can be approximated as a thin circular disc with a rounded boundary, whose radius at the hedge (r) is smaller than the radius of the disc corresponding to the arc root (R). The pressure due to surface tension, P_{st} , insists on the pool boundary balancing the internal pressure of the fluid volume. Just before droplet detachment occurs, P_{st} can be expressed as:

$$P_{st} = \frac{\sigma}{r} \tag{1.6}$$

where σ is the surface tension and r is the radius of the edge of the circular pool boundary just before droplet detachment.

The interaction of the radial component of the current density j_r with the self-induced magnetic field, in the azimuthal direction, induces an electromagnetic pressure on the insert surface:

$$P_{jxB} = \frac{\mu_0}{4\pi} A j^2 \tag{1.7}$$

where A is the area of the arc root and a uniformly distributed current density j is

assumed. This pressure is relevant with small arc diameters and high current densities [12].

Another flow exerts significant pressure on the cathode surface. The fully ionized status of the near-cathode plasma (*cathode sheath*) implies that plasma supplies the cathode with the maximum possible ion current density. In particular, in the cathode sheath the ions flowing from the plasma (ion current) contributes to the 30-50% of total current in normal conditions, but its fraction can achieve 75% [12, 13]. The current density at the cathode attachment can be estimated as [2]:

$$j \sim e\, v_i\, p/kT \tag{1.8}$$

where p is the plasma chamber pressure, e is electron charge, T is plasma temperature and v_i is ion thermal velocity. In the case of a temperature $T \sim 1$ eV (11650 K), $p = 4$ bars, the current density j is about $4 \cdot 10^4$ A cm^{-2}, that at the arc current of 200 A, results in a arc root of radius $R \sim 0.3$ mm [2]. Similar values were actually observed at these conditions both in the case of a tungsten cathode and in the case of the hafnium cathode [2, 14].

The number of ions impacting the cathode per unit area and per unit time is $n = \eta \cdot j / e$, where the ion current fraction of the total current is assumed to be η. The ion current pressure can be then expressed as the momentum change of these impacting ions [12]:

$$P_{ion} = \eta j \sqrt{\frac{2 m_i V}{e}} \tag{1.9}$$

where known ion mass is m_i, the sheath voltage at the cathode is assumed to be V and e is the electron charge.

According to this model, the forces on the molten pool due to the plasma ($P_{j\times B}$ and P_{ion}) are partially balanced by the surface tension forces (P_{st}), and thus the radius of droplets formed at the edge of the molten pool is inversely proportional to these forces. Therefore, the ejection of smaller droplets is in particular expected during the arc ignition phase, when the ion pressure is larger, while larger droplets are expected during subsequent cutting or arc-off phases.

One further force acting on the on the molten pool is the aerodynamic drag caused by the swirling gas flow. Its magnitude is higher on the periphery of the arc, where the

molten pool is in close contact with the cold swirling plasma gas. Moreover, in this peripheral area, the current density and electromagnetic forces are smaller. Hence, the effects of the gas swirl flow are particularly relevant during those phases in which there is little or no current flow and the cathode is in a molten state, such as during shutdown.

Peters et al. [12] calculated the expected Hf particle diameter, according to this model, for a oxygen plasma operated at 200 A. In this configuration, the current density in the highly constricted arc is about 10^8A m^{-2}. They found that, for a Hf insert in a oxygen plasma environment, maximum particle diameter should not exceed 55 μm, and detected that most of droplets were actually under 50 μm. A value of 1.5 N m^{-1} for pure Hf was used for the value of surface tension, although the molten material is hafnium oxide rather than pure Hf; moreover, the lowering of the surface tension by the dissolved oxygen, which would decrease the diameter value, was not considered.

Constant current erosion

Constant current erosion in Hf cathodes occurs during the steady state cutting phase and depends upon factors such as gas pressure, arc current, and gas flow pattern near the insert surface.

The physical process triggering constant current erosion is the evaporation of the cathode material due to its high temperature. It is possible to calculate the flux of the evaporating atoms by knowing the cathode temperature. However, experimental tests show that the real erosion rate is significantly lower than expected [2]. In fact, a significant amount of the evaporated atoms return back to the cathode and the net erosion is due to the small difference between the flux of the evaporated atoms returning particles [15, 16].

To understand this phenomena, one should consider the forces acting on the evaporated atoms, such as the electric force, electron–ion drag and the gas flow drag. Due to the high plasma ionization potential, the evaporating atoms from the molten pool are almost immediately ionized. Close to the cathode, a strong electric field retains the ion to the cathode surface while, at bigger distances, it is the electron–ion friction which drags the evaporated atoms back to the emissive insert. At even farther distances, the gas flow drag dominates, as the plasma flow velocity increases with the distance from the cathode. Fig. 1.10 shows a distance identifying a point of ‘point of no return’, after which the ions lose the possibility of returning back to the cathode. It is then clear that

the velocity pattern close to the cathode has crucial importance on the net erosion.

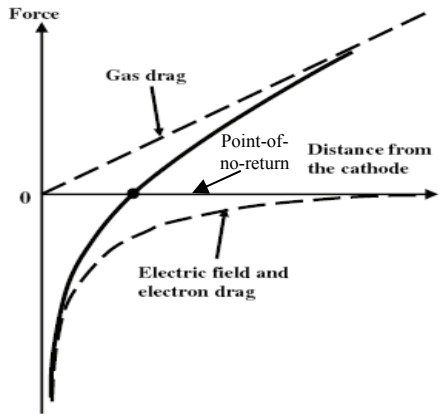

Fig. 1.10 Schematic of forces acting on the evaporated particle in the near-cathode plasma as a function of the distance from the electrode [2].

Although there is no available model to calculate with sufficient accuracy the erosion rate during constant current phases, experiments for Hf cathodes [2] detected an escape coefficient in the 0.005–0.01 range, confirming that majority of evaporated atoms are sent back to the cathode. This fraction raise to 1–5% for tungsten emissive inserts [2, 15].

It was previously described that, in order to stabilize arc position, to increase cut quality and to protect the nozzle, plasma gas is supplied in the arc chamber with a swirl component through a swirl ring. However, due to the abovementioned reasons, together with the positive effects, the plasma gas swirl increases the cathode erosion, as shown in Fig. 1.11. In particular, the higher is the swirl component, the stronger is the gas flow drag near the cathode, thus shifting the 'point of no return' closer to the emissive insert surface.

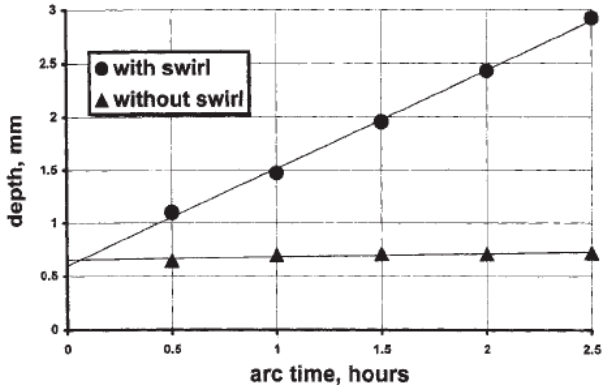

Fig. 1.11 Erosion cavity depth with and without gas swirling as a function of arc time for Hf cathode at 400 A, 4 bars [14].

Another experiment showed that the erosion rate for Zr inserts decreases with time for long arc duration tests [17]. The authors explained this behaviour by considering that an erosion crater is created and deepens during arcing. A stagnation zone forms inside this crater, slowing down of the gas flow, thus increasing the probability of the evaporated atom/ion returning to the cathode. One again this experiments highlighted the importance of the gas flow pattern on the constant current erosion rate.

Higher pressure in the plasma chamber induces higher erosion rate, in compliance with theory, as highlighted in Fig. 1.12, showing the cathode cavity depth as a function of arcing time for different chamber pressures for the hafnium cathode. Indeed, according to models developed by Neumann in [18] and by Benilov and Marotta in [19], current density in a cathode spot is directly proportional to gas pressure. Thus, in order to support the higher current density with proper thermoionic emission at the cathode attachment, the electrode temperature in the cathode spot should be higher, thus increasing the erosion rate.

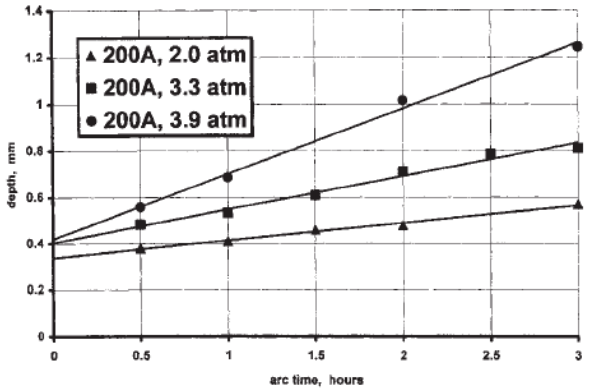

Fig. 1.12 Cavity depth *vs* arc time for Hf cathodes at 200 A at different plasma arc chamber pressures [14].

According to the model reported in [19] the current density and, therefore, the cathode spot temperature, does not depend much on the arc current, which is in contrast with experimental practice. In the model, the available area of the cathode spot was assumed to be very large. In reality, this area is limited. Hence, the cathode spot cannot expand as much as it would have at an infinite cathode surface with rising current. This constraint implies a temperature increase and in turn enhances the erosion as the current density rises.

Cyclic erosion.

Further than constant current erosion, hafnium cathodes in an oxygen atmosphere are characterized by the so called 'cycling erosion', related to the process of switching the arc on and off. Therefore, total erosion depends on the number of starts further than aching time, as shown in Fig. 1.13. Since in industrial application of PAC cuts could be relatively short and the number of cutting cycles could be high, this cyclic erosion, occurring both at switching the arc on and during switching the arc off, represents a significant or even dominant portion of the total erosion.

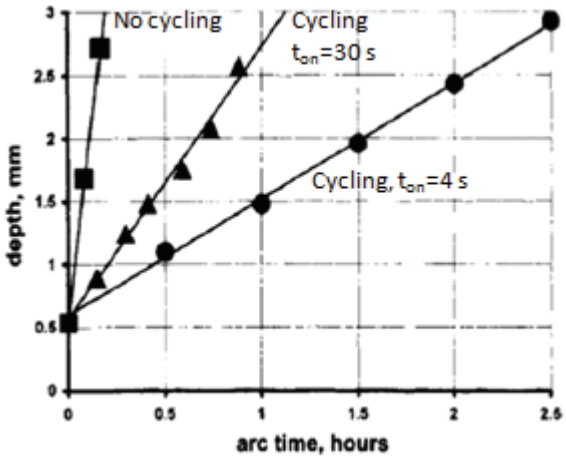

Fig. 1.13 Cavity depth *vs* arc time without cycling and with cycling for Hf cathode at 400 A [14].

Arc-on erosion.

One hypothesis on arc-on erosion links its origin to the removal of an insulating layer of hafnium oxide [11, 14, 20]. Although the specific mechanism of this removal is not completely understood, the following qualitative explanation was supplied in [2], based on the experimental experience that the gradual increase in the arc current decreases the arc-on erosion.

As previously highlighted, the arc is first ignited between the nozzle and the hedge of the copper holder, where the distance between the two component is the minimum one. The arc is then moved toward the emitter periphery and finally to the insert centre. The heat wave generated by the arc moves with a different velocity with respect to the arc attachment, heating the emissive surface and, after a certain transitory, melting it. As discussed in section 1.2.3, concerning the insert materials, the superficial Hf oxide has to be melted to behave as a proper thermoionic emitter. Moreover, the arc

attachment expands as the arc current increases during its migration toward the insert centre. Should the arc attachment movement and expansion (i.e. the current increase rate) occur too rapidly with respect to the Hf oxide layer melting, the expanding arc attachment would have to remove this solid layer before further moving. Possibly, this removal process would happen through a series of thermal shocks, breaking the Hf oxide layer and causing massive particle ejection, although the specific mechanism of this removal is not yet completely clear.

Arc-off erosion.

During arc off, droplets flying in the plasma chamber were observed in [12]. According to the authors, when shutting down the arc, the imbalance of the fluidynamic drag forces, magnetic and ion pressure on the molten surfaces causes relevant droplets ejection. They also observed that cathode behaviour during the shutdown is independent to the type of gas flow (oxygen or nitrogen), although, on the other hand, appeared to be very dependent on the type of current ramp-down employed. In particular, when the current ramp down is slow and lasts as long as the pressure transient, the molten pool is very stable and very few droplets are ejected. On the contrary, if the current is ramped down very quickly, (around 1 ms as for an emergency stop), many large particles are ejected, as the pressure drops more slowly than the current, leading to strong imbalance of the forces acting on the molten pool and in particular because the molten metal surface is exposed to the high velocity gas flow. The solidification time has been measured to be of the order of 6–8 ms for a 200 A current arc, and the droplet ejection has been observed during this entire time period.

Another hypothesis advanced by Nemchinsky et al. [2, 11] considers the effect of the plasma gas dissolved in the molten pool. During cutting operation, there is high-pressure hot plasma gas in contact with a molten layer of emissive materials. Hence, atoms, molecules and ions of this plasma gas easily penetrate this layer and dissolve in it. Moreover, due the plasma pressure (typically a few atmospheres), the gas particles' concentration in the molten pool is relevant. At arc-off, the pressure in the plasma gas drops rapidly. This steep depressurization is the consequence of the rapid ion–electron recombination and the association of atoms into molecules, which leads to a decrease in plasma concentration, and to the fact that the central hot part of the nozzle orifice,

where the plasma concentration was low, is now able to carry much higher gas flow rates. This fast reduction in ambient pressure induces the gas liberation from the molten puddle. Some gas exits from the melt in the form of bubbles, which drag and carry away with them liquid metal droplets, thus generating erosion. The craters on the surface on tungsten cathode, observed in [20] after termination of a 400 A arc in a hydrogen atmosphere, supports this hypothesis [2].

1.3.2. CRITICAL PATENTS REVIEW

The state of the art in plasma arc cutting technologies is mainly outlined by a relevant amount of patents literature, rather than by journal scientific papers. In particular, due to the high impact of the electrode durability on PAC industrial potentials at high current levels, different solutions to improve the electrode endurance performances have been developed. In the present section, a review of the most relevant patents concerning this subject is accomplished.

The basic patent on plasma arc cutting (PAC) was applied for by Gage in 1955 [21]. His invention arose as a result of his work aimed at improving the directional stability of the open arc used for TIG welding. In its original version, PAC was used primarily for cutting stainless steel and aluminium by means of nitrogen or argon–hydrogen plasma gas. In this inert environment, tungsten electrodes have been used for many years as high current electrodes in arc devices. The addition of emissive -oxides, such as thoria, yttria and calcia, to the refractory electrode was also well known to increase the current carrying capacity. Such electrodes could be used in a substantially non-consumable fashion up to current levels of thousands of amperes.

The expired *US patent 3,198,932* (1964) [22], by Union Carbide Inc., claimed the use of an electrode comprising “an insert made of a material which is a good electron emitter, or which becomes a good emitter upon reaction with a reactive gas”, such as methane or oxygen. Proposed material were in particular: zirconium, thorium, lanthanum and strontium. The preferred embodiment, which was widely adopted in industry for many years, comprised a water cooled copper holder having embedded therein an insert of zirconium.

The patent also claimed the addition of silver powder to the emissive material, to improve the heat transfer from the insert without substantially increasing the work function of the insert.

Further improvement in heat dissipation is claimed to be achieved providing a metallurgical bond between the insert material and the holder. For example, silver can be melted and a Zr insert, plated with a zinc film, can be dipped therein, thus applying a silver coating. Then silver is melted into the cavity of insert holder. The zirconium insert with the silver coating is inserted into the cavity. Heat is then applied until the silver flows around the insert. According to later *US patent 5,200,594* (1993) [23], this solution does not result in an improvement in the operation life of the main electrode as high as expected. The zinc film separates easily from the insert of zirconium. Moreover the silver soldering material melts and forces the insert to separate from the base electrode.

In the '932 patent, the preferred geometrical shape for the insert is cylindrical, but the use of ring or tubular shaped inserts or irregular shaped inserts, as well as multiple inserts, is also claimed.

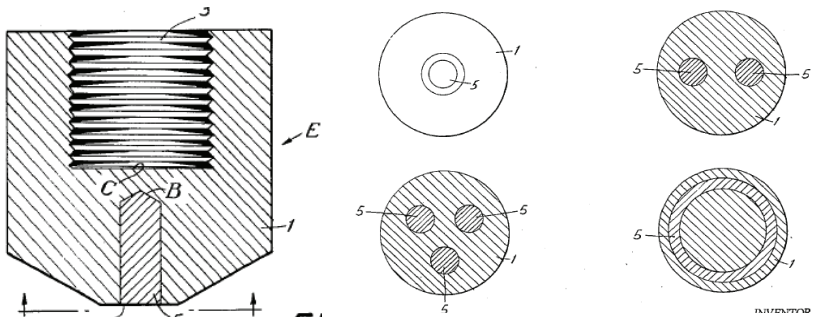

Fig. 1.14 Insert configurations as described in *Us pat. 3,198,932* [22].

The expired *Us pat. 3,546,422* (1970) [24] by Bykhovsky et al. claimed the introduction of a gasket (i.e. a distant piece) between the electrode insert and holder, to increase the cathode life. The gasket material is inert with respect to the cathode material (zirconium) and the cathode holder material (copper or copper alloy) and is preferably selected among tungsten, tantalum, molybdenum, niobium, vanadium or chromium.

Background of the invention was the conventional zirconium cathode, which was known to have an extremely short service life (not over 4 hour) at arc currents of 250 A in active media. One of the main causes of excessive wear of the zirconium cathode is identified by the authors in the deterioration of the thermal and electrical contact with copper cathode holder, according to the following process. The high interfacial temperatures cause the formation of intermetallic compounds at the point of contact, these compounds having a far lower heat and electrical conductivity than copper or zirconium. The layer of intermetallic compounds interferes with the withdrawing of heat from zirconium, which leads eventually to its ultimate destruction.

The thickness of this claimed gasket solution should be "sufficient to rule out the diffusion of copper into zirconium". The gasket can be inserted by electrodeposition or by vacuum spraying of these metals on the cathode or cathode holder, or fitted into the cathode holder by a mechanical method.

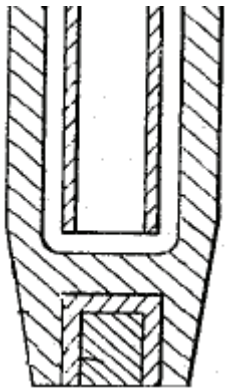

Fig. 1.15 Gasket (distant piece) between the electrode insert and holder, as claimed by *US pat. 3,546,422* [24].

Hafnium as emissive material is for the first time introduced by the expired *US patent 3,597,649* (1971) [25], by Bykhovsky at al., aiming at extending the cathode life service in active media. Hafnium was selected for the cathode because, when reacting with the oxygen, nitrogen and carbon contained in the plasma-generating gas, it is covered with a film on the working surface consisting respectively of high-melting oxides, nitrides or carbides of hafnium. These films have a relatively low electron work function of electrons. Besides, the structure and the thermal and physical characteristics of the film was claimed to hamper the further reactive diffusion of the active components of the plasma-generating medium.

In *US pat. 3,930,139* (1975, expired) [26], Bykhovsky at al. disclosed the use of hafnium insert with yttrium and neodymium oxides as dopants, fastened to the end face of the Cu holder, "in thermal and electrical contact with said holder through a metal distance piece" of aluminium or Al alloys, with a configuration similar to the one shown in Fig. 1.15 for [25].

The authors stated that the rapid burning-out of the standard nonconsumable electrodes with the hafnium inserts is, in the first place, attributable to the breakdown of the copper holder. When operating in oxygen, as the erosion of the active insert increases and an arc column immerses into the forming crater, the copper melts and rapidly oxidizes in the vicinity of the active insert. The oxidized melt being formed flows off into the crater and onto the active insert, leading to its contamination and a sharp increase in the erosion velocity, especially with electrodes operating in oxygen with an intermittent cycle. According to the authors, their previous attempt at separating the hafnium insert and copper holder with an inert spacer ("gasket") of vanadium, niobium, tantalum, chromium, molybdenum and tungsten [24] was not successful, as oxides formed on the above metals when operating in oxygen were characterized by high vapour pressure and evaporated rapidly, thereby not being capable of protecting copper from the effect of an arc column. On the other hands, the employment of the metal spacer of aluminium (0.01-0.2 mm thickness) or its alloys provides, according to the author, a full and useful service life of the nonconsumable electrode, when operating in oxygen, along the entire height of the active insert since the aluminum oxide formed on the metal spacer is a high-melting compound having a melting point of 2043 °C. This film thereby acts as a thermal shield protecting the copper holder from both overheating and oxidation. The authors also claims that in the electrodes operating in oxygen, yttrium oxide stabilizes hafnium oxides formed on the emitting surface and increases their thermostability. Moreover, the role of neodymium oxide, as a dopant, consists in enhancing the electrical conductivity of the hafnium oxide being formed. Improved electrical conductivity would reduce heat liberation on the active insert and contribute to a prolonged service life.

Since cutting quality is dependent on arc stability, in order to stabilize the arc position in proximity of the insert centre and avoid its migration, the authors of *US pat. 3,944,778* (1976, expired) [27] disclosed an electrode assembly for a plasma torch in

which the central portion of the effective area of a high-heat insert (e.g. tantalum, tungsten, hafnium) is overheated. To obtain this result, a chamber, substantially symmetrical to the insert axis, is formed in the holder between the high-heat insert and the holder being cooled. As the inner space of the proposed electrode assembly is filled with a substance (e.g. titanium, austenitic steel, air, argon, etc.) whose coefficient of thermal conductivity is lower than that of the material of the holder which is being cooled, heat transfer is reduced and local overheating is attained.

In order to achieve this effect of arc stabilization, it is necessary to make the height of the thin insert lower than the diameter. Such a thin insert undesirably results in a short operation life, making this solution practically unsuitable for high performance industrial processes at high currents.

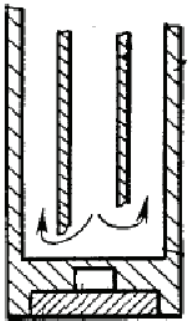

1.16 Low conduction chamber aimed at stabilyzing the arc attachment, as described in *US pat. 3,944,778* [27].

An electrode for electric arc processes composed of a water-cooled holder into which is fitted a case hardened or diffusion coated insert of zirconium or hafnium is claimed in *US pat. 4,766,349* (1988) [28] by Aga AB Inc., expired in 1996 due to failure of maintenance fee payment. The diffusion zone consists of carbide, nitride, boride or silicide, (i.e. compounds with very high melting points), in order to suppress detrimental reactions between the holder and the insert.

The authors state that tests on previously patented solutions showed unsatisfactory performance with electrodes working in active media. In particular, three different electrodes were prepared according to different arrangements described above. The electrodes were tested in a plasma arc cutting device and with air as the arc gas, although tests conditions were not specified.

According to the authors, in electrode with a hafnium insert fitted into a copper

holder, the hafnium-copper phases that are formed have low melting points resulting during operations in the formation of a drop at the tip of the cathode, which accelerates the deterioration of the electrode.

If an aluminum foil is used between the copper holder and the hafnium insert (as disclosed in *US pat. 3,930,139* [26]), alloying will occur during operation and in a zone between the holder and insert, as there is a lowest liquidus point of about 1350°C, according to the Hf-Al system. If the aluminum foil is eliminated an alloying zone will be formed with a lowest liquidus temperature of about 900°C as found in the Hf-Cu system. According to the authors, the different liquidus temperatures mentioned explain the higher operational time operation for hafnium-copper electrodes with aluminum foil interlayer.

In electrodes with interlayers comprising transition metals (*US pat. 3,546,422* [24]) an alloying zone between the holder and insert with melting temperatures similar to electrodes containing interlayers of aluminum is expected from authors.

In the disclosed invention, the surface zone is formed by case hardening or diffusion coating of zirconium and hafnium inserts in order to create a diffusion zone (*10* to 100 μm thick) with melting points in the range of 2000°-4000° C. Moreover, in order to prevent its deterioration during operation, the holder with surface hardened insert is given a corrosion stable and heat reflecting finish of nickel, chromium, nickel-chromium or platinum metal applied by e.g. electroplating, PVD or CVD. These compounds, by forming a diffusion zone, should prevent reactions to occur between the core of the insert and the holder. Furthermore, carborizing of hafnium should supply a zone of low electrical resistivity and a high thermal conductivity between the core of the insert and the copper holder.

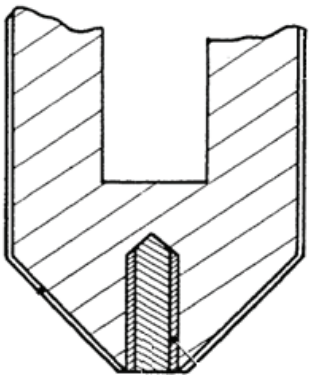

Fig. 1.17 Diffusion zone in Hf/Zr insert according to *US patent 4,766,349* [28].

In European pat. *EP 437915* (1992) [29] and *US pat. 5,097,*111 (1993) [30] by Esab Inc., a “sleeve” of silver (or “other metal having a relatively high work function”) is positioned to surround the insert and form an annular ring (Fig. 1.17). The annular ring aims at preventing the arcing from the copper holder. According to the authors, as the copper oxidizes, its work function falls. Although this statement is not supported by data, and the work function of the copper oxide is still higher than the one of Hf oxide at room temperature, it is know that at certain erosion levels the oxidized copper which surrounds the insert begins to support the arc in preference to the insert (Fig. 1.9), as also stated in previously mentioned patents. When this happens, both the copper oxide and the supporting copper melt, resulting in the early destruction of the electrode.

In this invention by Esab, the ideal sleeve materials should be characterized by high thermal conductivity, high resistance to oxidation, high melting point, high work function (at least about 4.3 eV), and low cost. According to the authors, the best compromise is silver. Since silver and any oxide which it forms are very poor emitters, the arc will continue to emit from the emissive insert. The non-emissive sleeve can be metallurgically bonded into the cavity by brazing.

The EP version of the described patent was first opposed by Kjellberg Inc., and finally lapsed between 2009 and 2010 due to non payment of due fees in EU contracting countries.

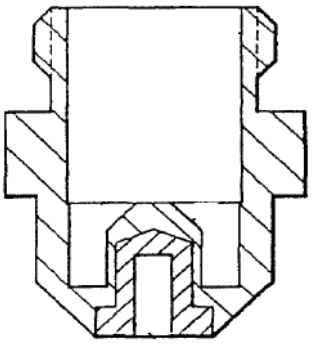

Fig. 1.18 Silver sleeve configuration for electrode according to *EP 437915* [29].

With later *US pat. 6,020,572* (2000) [31] and *EP 0980197* (2003) [32], a continuation in part of [29, 30], Esab stated that the performance of such electrodes can be further improved if the non-emissive separator formed of silver is alloyed with 0.5 to 4 percent of copper or other metals (aluminum, iron, lead, zinc), as service life was

discovered to be quite sensitive to the specific composition of the silver alloy used, although the mechanisms involved were not detailed. According to these patents, the sleeve is plastically formed and press-fitted into the electrode body hollow, prior to press-fitting the emissive insert. The '*197* European patent finally lapsed because of non-payment of due fees.

In *US pat. 5,200,594* [33] and *EP 0465109* (1992) [34], Daihen Inc. described an electrode for use in a plasma arc working (cutting/welding) torch characterized by an insert of refractory metal (such as Hf or Zr) with a double coating of nickel ("electro-plated") and a noble metal ("plated"). Moreover, the electrode is characterized by a room, formed between the bottom face of said hollow and the end face of said insert of refractory metal, fulfilled with a low melting material (Fig. 1.19).

According to the authors, the plated nickel essentially does not form the nickel oxide. As a result, the heat generated during the working of the plasma arc working torch is dissipated rapidly through metallic Ni. The electrode is not over-heated providing a longer operation life.

The authors states that during the work of a plasma arc torch, the insert of refractory metal is heated to a temperature of about 600° C at the end terminal facing to the bottom face of the hollow. The material having a low melting point melts during the work of a plasma arc working torch and causes the thermal connection between the end face of the insert of refractory metal and the bottom face of the hollow of the base electrode. Accordingly, the heat generated at the insert of refractory metal is transmitted rapidly to the base electrode through the thermal connection. Superior duration of the presented solution with respect to conventional Hf electrodes are reported by the authors, although without specifying detailed test conditions.

The patent expired, as its priority dates 1990. Commercial electrodes with the presented configuration are available e.g. for 120 A torches.

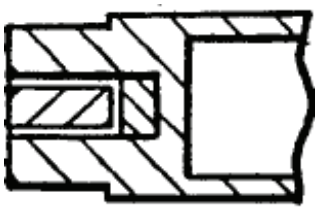

Fig. 1.19 Electrode configuration as described in *US pat. 5,200,594* [33]

US pat. 5,310,988 (1994) [35], by Hypertherm, aimed at improving the electrode useful life through the optimization of the Hf insert diameter "as a function of the level of a current carried out by the electrode".

In fact, the area required for emitting varies as a function of the maximum operating current. However, in order to have higher heat conduction, this emitting area should be the minimum area of the insert. Thus, the insert has a diameter that is at least of the same size of the molten emission spot produced on the emitting surface by the selected operating current but, preferably, it has a slightly larger diameter to ensure that the arc does not impinge on the adjacent copper body.

This patent gave rise to the European one *EP 0641269* [36] under the same title; finally revoked (in 21.11.2003) after a long and intricate opposition procedure started by the competitor Air Liquide.

US pat. 5,464,962 (1995) [37], again by Hypertherm, is a continuation in part of *US pat. 5,310,988* [35] and it is aimed at "minimizing the deposition of high emissivity material on the nozzle" due to massive ejection phenomena that take place at high current levels during first starts, by shaping the emission surface in order to define a concave recess in the Hf insert.

Since the emissive surface has a generally planar initial shape in conventional torches, the high emissivity material melts during operation of the torch and is ejected from the insert until the emission surface has the generally concave shape. This concave shape has a curvature which is a function of the current level of the torch, the diameter of the insert and the gas flow pattern in the torch.

In the disclosed electrode, the emission surface may define a recess which is generally concave, generally cylindrical or other shapes: according to the authors, while emission surfaces defining certain recess shapes are desirable due to their ease of manufacture, the initial shape of the recess is less important than its overall dimensions (Fig. 1.20). Since the amount of high emissivity material initially removed corresponds to that amount ejected from the conventional electrode during the first several starts, the improved electrode offers wear rates comparable to conventional devices.

A try and fail procedure was followed by Hypertherm to define a optimal initial shape, as later discussed in Chapter 2. The high emissivity material is removed using a ball end mill.

This solution is still widely used by Hypertherm as its introduction provided a significant consumables performance increase. This patent gave rise to the European one *EP 0772957* [38] under the same title; finally lapsed (11.07.2005) for non-payment of due fees in all European designated contracting states.

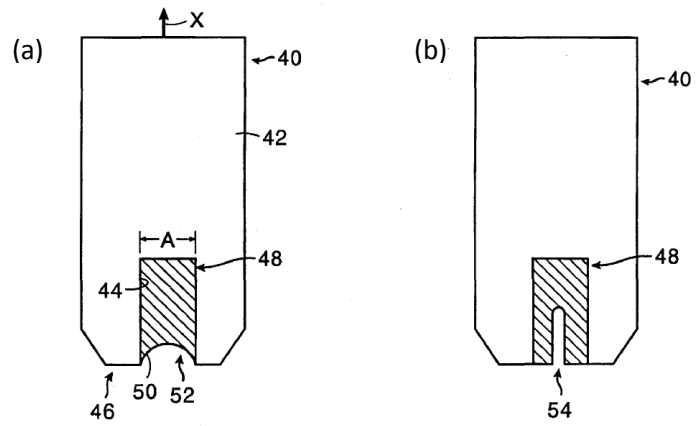

Fig. 1.20 Electrode configuration as described in *US pat. 5,464,962* [37].

US pat. 6,066,827 [39] (2000), by Esab, discloses an "electrode with emissive element having conductive portions", primarily concerned with decreasing start erosion with oxidizing gas.

The oxide which forms on the emissive (Hf) insert upon cooling, subsequent to the operation of the torch, constitutes an electrically resistive layer. Hf oxide retains its conductive properties only when hot. As seen in the previous section concerning cathode erosion, the arc expansion during arc on causes thermal "shocks" and subsequent cracking of the brittle hafnium oxide, contributing greatly to the start erosion problem and increasing the possibility of detrimental double arcing. The conductive portion, constituted by a material such as silver or copper, provides a conductive path which allows the arc to be supported until the oxide layer reaches an operating temperature, thereby preventing thermal cracking and removal of the oxide layer.

One particularly preferred embodiment includes a plurality of emissive filaments, which defines an array of adjacent emissive portions the front face of the electrode (Fig. 1.21 *a*). In another embodiment, a single diametrically extending layer constituents the conductive path (Fig. 1.21 *b*). According to the patent, the emissive element assembly can also include a relatively non-emissive separator, composed of a metallic material

having a work function of at least about 4.3 eV, such as silver or silver alloys.

Authors state that in cycling tests at 300 A, with an arc for four seconds and then without an arc for four seconds, for approximately 30 minutes, the electrodes of the present invention exhibited significantly reduced overall erosion compared to the standard electrodes and were capable of achieving more starts.

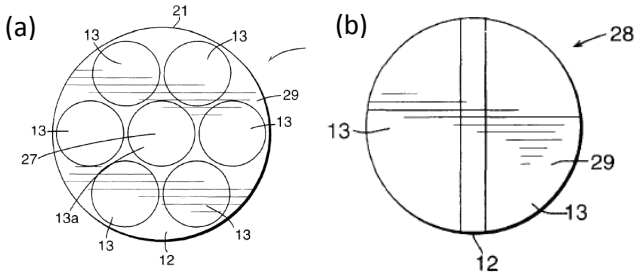

Fig. 1.21 Two different embodiments for the electrode configuration according to *US pat. 6,066,827* [39].

For a traditional cylindrical insert, the size of the emitting surface is increased for higher current capacity operations [2, 35]. Therefore, the removal of heat from the centre of the insert to the surrounding electrode body becomes difficult. With *US pat. 6,130,399* [40] and *EP 1099360* [41] (2003), Hypertherm tries to "overcome certain inherent limitations existing in the traditional cylindrical insert design", to improve the electrode service life particularly for high current processes. In view of this goal, the insert is designed to facilitate the removal of heat and, in some embodiments, comprises a high thermal conductivity material further than a high emissive material.

In one aspect, the present patent presents different insert shape, such U- or ring-shaped inserts of Fig. 1.22, to optimize the heat removal.

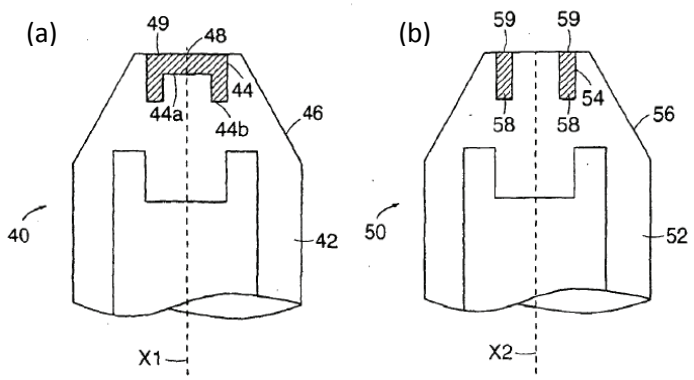

Fig. 1.22 Insert configurations claimed in *EP 1099360* [41].

In another aspect, the insert (Fig. 1.23 *a*) is a composite structure realized rolling up a layer of high thermal conductivity material placed on a layer of high thermionic emissivity material. In another embodiment, the insert includes a cylindrical member formed of high thermal conductivity material and a plurality of parallel bores filled with a high thermionic emissivity material (Fig. 1.23 *b*). In yet another embodiments (Fig. 1.23 *c*), the insert is formed by "sintering a composite powder mixture of a high thermal conductivity material and a high thermionic emissivity material".

The authors claims that the patented solutions improved service life, especially for higher current operations (I>200A), and minimized double arcing, thanks to the improved heat removal configuration.

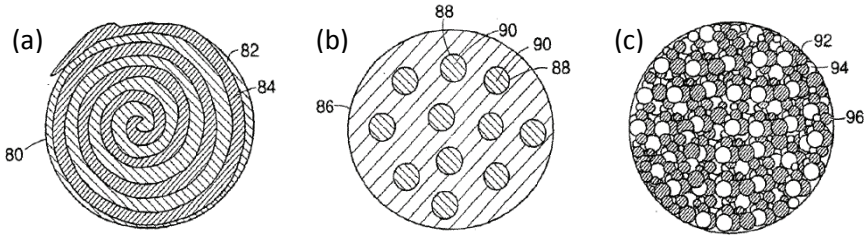

Fig. 1.23 Examples of the composite insert configurations as claimed in *EP 1099360* [41].

Many conventional electrodes are assembled by pressing the emissive insert into the metallic holder, or by pressing the emissive insert into a relatively non-emissive sleeve or separator that is then pressed into the metallic holder. The interfaces between the press-fit emissive element, separator and holder are relatively well defined, and therefore negatively affect heat removal and consequently the operational life span of the electrode.

To overcome this limit, *EP 1263268* (2002) [42], by Esab, describes an electrode for a plasma arc torch wherein an intermetallic compound is formed between the emissive element and the separator, and an eutectic alloy is formed between the separator and metallic holder, by means of independent heating steps. First, the separator and the emissive element are brought in surface-to-surface contact, heating the assembly between 926÷982° C for about 1 hour, to form an intermetallic compound about 0.01 mm thick. In a second step, the assembly is positioned in a cavity of a Cu

holder, in surface-to-surface contact. After the assembly is in place, an eutectic alloy is formed between by heating a copper metallic holder and a silver, particularly to about 777-779° C (the declared eutectic forming temperature for these materials) for about 0.02-20 minutes. The assembled electrode can also be crimped to provide improve the strength of the assembly.

According to authors, the method do not require brazing materials, coatings, or other layers between the emissive element, separator, or metallic holder, thereby reducing cost and complexity of fabricating the electrode. The patent is still in force in some of the European contracting, such as Italy, Germany or Great Britain, whereas it lapsed some EU countries due to non-payment of due fees.

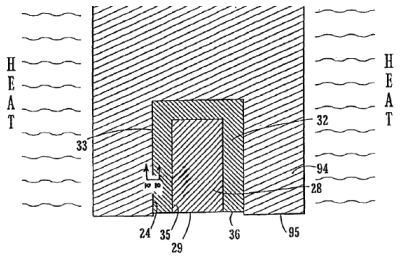

Fig. 1.24 Second heating step of the electrode assembly according to *EP 1263268* [42].

In the subsequent application *US pat. 6,563,075* (2003, in force) [43] and *EP 1322144* (2003, deemed to be withdrawn in 2010) [44], Esab disclosed an alternative and faster method of forming an intermetallic compound between the emissive element and the separator by "heating a relatively non-emissive material until it melts and dipping the emissive element therein before cooling the assembly". As a result, the intermetallic compound is claimed to be formed significantly faster (about 1 minute) than by conventional methods.

In conventional inserts, the arc starts to be emitted from the copper holder when the consumption depth d of the insert reaches a limit value d_{max}. The invention object of *US pat. 6,583,378* [45] (2003, expired in 2011 due to failure of payment of due fees) by Komatsu Inc., claims of prolonging the electrode lifetime of plasma machining electrodes having a hafnium or zirconium insert protruding from the tip of the copper holder, in oxygen PAC. The protrusion is characterized by a length L not larger than the diameter D of the insert, (preferably not larger than 0.5 mm) without rounded angles.

According the invention, the protruding portion makes the insert longer and increases the volume of the insert subject to consumption, so that the electrode lifetime is prolonged. The insert and the holder are preferably joined together by a metallurgical method, such as silver brazing. At least during the generation of the pilot arc, a plasma gas containing at least 5 mol % nitrogen is used.

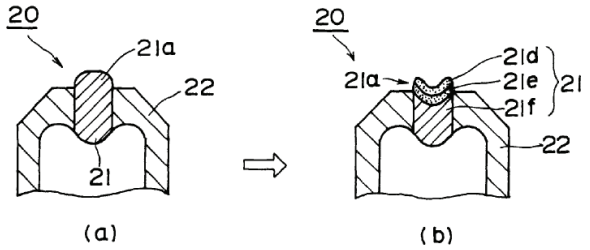

Fig. 1.25 Insert configuration claimed in *US pat. 6,583,378* [45]: as supplied (a) and after cutting (b).

In some cases, conventional tungsten electrodes in which the insert protrudes from the tip face of the holder are used [45]. During the generation of an arc, the electrode surface of tungsten electrodes is usually solid, except for the vicinity of the cathode spot where the temperature is highest. In hafnium or zirconium inserts, however, a considerable portion of the insert surface can be liquid. Therefore, if the hafnium or zirconium insert protrudes from the holder, the protruding portion becomes liquid, so that this portion may be blown off. As a consequence, to retain the liquid hafnium in electrodes using conventional hafnium inserts, the surface of the inserts of new electrodes is coplanar with the tip face of the holder or even somewhat depressed toward the inside [37, 38].

According to the present invention, if the hafnium or zirconium insert protrudes outward, this protruding portion is not necessarily blown off by the arc generation, but may be retained at the electrode tip under specific conditions. According to the authors, which presents results only for 120 A piercing, the use of a oxygen-nitrogen gas mixture containing at least 5 mol % nitrogen protect the protruding Hf from being blown off during first arc ignition. Starting from the subsequent cut, the oxidized Hf layer with high melting point should protect the surface of the protruding portion of the insert, so limiting blowing off, even when starting an arc with pure oxygen.

The effectiveness of the present invention at high currents (over 200 A) has not been proved nor discussed.

EP 1481574 (2004, in force) [46] and *US pat. 7,098,422* (2007, in force) [47] by Kjellberg Inc. disclose an electrode assembly in which between the insert and the metallic holder shell there is provided a "boundary layer in a graded form", made up of solid solutions of the two metals or metal alloys, or an intermediate layer, which is made of another metal alloy having a work function greater than that of the core material. In one embodiment, the spacing between a sleeve-shaped copper part and a bar-shaped element (preferably Hf), can be filled with a silver powder, and the appropriate intermediate layer is allowed to form with a respective graded transition towards the Hf surface and towards the copper part due to compressing forces during extrusion molding process or hot isostatic pressing.

According to the authors, such an electrode element provides low thermal and electrical transition resistances as a result of the more intimate contact with the graded transitions of the different metals and metal alloys, and the service life can be increased significantly. Moreover, intermediate layers are allowed to be formed with a significantly lower layer thickness so that the expensive use of silver can be limited.

Although silver electrodes provide excellent heat transfer characteristics, they are very expensive and generally not cost effective. Copper electrodes are cost effective, but do not equal heat transfer characteristics of a silver electrode and thus have a shorter electrode life. Several companies manufacture silver and silver/copper composite electrodes using a variety of manufacturing techniques including brazing, soldering, press fitting and other methods. However, these methods of manufacturing silver/copper electrodes do not produce a sufficiently high-strength joint at the silver/copper interface and risk of possible leaking of cooling fluid at the silver/copper interface. More generally, these silver/composite electrodes do not offer the heat transfer characteristics of an all silver electrode.

US pat. 7,659,488 [48] (2006) and *EP 1369000* [49], by Hypertherm, discloses a composite electrode which can be made of a metallic material (e.g. Ag) with high thermal conductivity in the forward portion electrode body, adjacent the emitting surface, and the aft portion of the electrode body is made of a second low cost, metallic material with good thermal and electrical conductivity (e.g. Cu). The two portions are joined by a direct welding process, such as friction welding, (e.g. inertia friction welding), percussive welding, ultrasonic welding, or explosion welding, thus forming "a

hermetic seal between the two portions of the electrode". To maximize cooling, the forward (Ag) portion can also extend back to the area of cooling fluid flow and is therefore directly cooled. This construction is believed to provide an electrode that has superior heat transfer properties and does not leak cooling fluid.

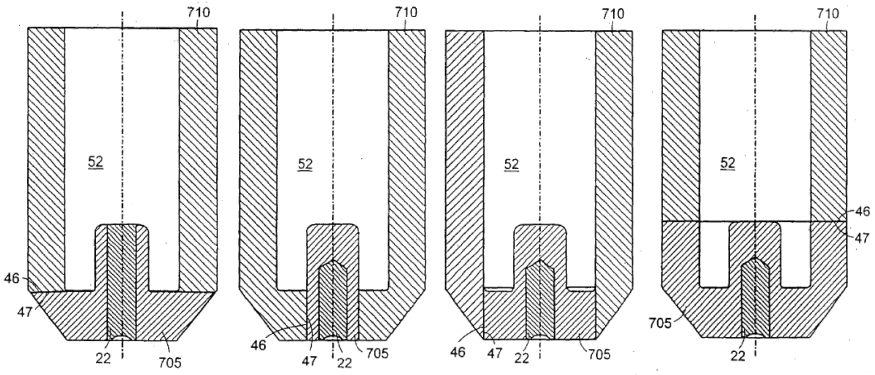

Fig. 1.26 Composite electrode according to *US pat. 7,659,488* [48].

When assembling (Hf) inserts of traditional cylindrical configuration into straight-walled bores, the insert tends to expand radially, in particular near the top of the bore, giving rise to a wedge shape, due to force distribution (Fig. 1.27). The resulting configuration initially secures the insert, but any movement of the insert towards the opening of the bore considerably decreases the surface contact and retention stability of the insert.

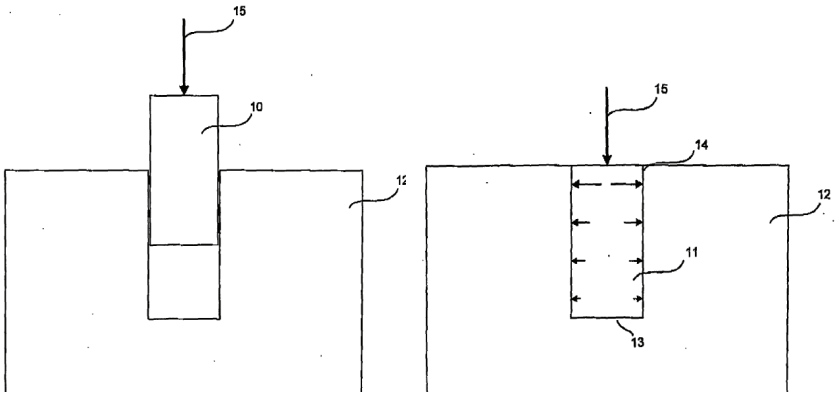

Fig. 1.27 Force distribution for standard press fit cylindrical inserts [50].

During the operations, torch conditions such as temperature gradients and different thermal expansion coefficient contribute to reduce the retention force holding

the insert in place, thus allowing the insert to move in the bore or to fall completely out. Furthermore, the movement of the insert also causes the insert-electrode interface degradation, which would reduce the thermal and electrical conductivity of the interface and thereby the operational life of the electrode.

In *EP 1765046* [51] (2007, in force in some European countries such as Italy or Germany, although opposed by Air Liquide) and [52], Hypertherm described an improved electrode for use in a plasma arc torch aimed at "improving retention of the insert in the electrode, establishing proper retention forces". One aspect of the invention features an electrode body characterized by a hollow cylindrical cavity which has smaller diameter in its deeper part. This discontinuity in diameters can define a step surface, which can be located anywhere along the length of the cavity, although far from the emitting surface (Fig. 1.28). The diameter of the insert can be smaller than both diameters of the bore such that the insert can easily fit in. When the insert is press fitted, the forces are greater near the step surface due to surface friction from the expanding insert, advantageously located away from the exposed portion of the insert which sustain the plasma arc during torch operation. Different bore and insert shape are disclosed to attain this retention effect and to enhance thermal conductivity in the present patent

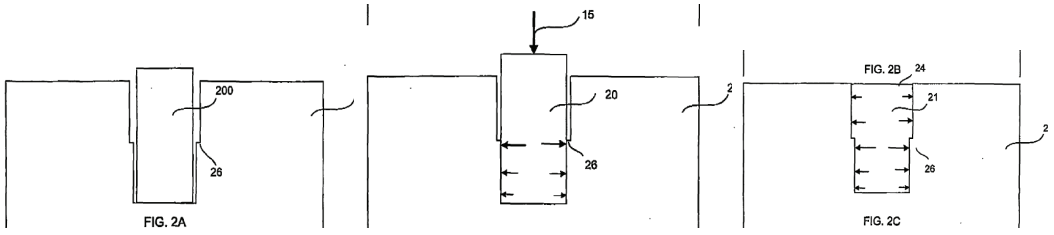

Fig. 1.28 Force distribution for improved electrode configuration according to *US pat. 125755* [50].

CHAPTER 2

EXPERIMENTAL ANALYSIS AND PERFORMANCE OPTIMIZATION OF HIGH CURRENT Hf CATHODES DURING FIRST CYCLES IN PAC TORCHES

ABSTRACT

Plasma arc cutting torches which are object of the experimental work described in this chapter make use of standard electrodes consisting of a cooled copper body and a Hf cylindrical insert. As discussed in the first chapter, PAC process performances are extremely affected by cathode erosion phenomena under operative conditions in which oxidizing plasma gases (oxygen and air) and high current levels (above 200 A) are used in presence of an Hf emitter, typically set for cutting mild steel (MS) plates thicker than 20 mm.

In the first section of the present chapter, the behaviour of Hafnium (Hf) cathodes at the beginning of their service life when operating at high current levels (250A) in the plasma arc cutting (PAC) process has been experimentally investigated with the final aim of understanding the phenomena that take place during those initial cutting cycles (*CCs*) and optimizing, with respect to expected service life, the initial shape of the electrode emissive surface. The experimental tests were carried out in realistic operative conditions for cutting mild steel plates with oxygen/air as plasma/shield gas. Starting with an electrode having a plane new emissive surface, subsequent *CCs* have been accomplished checking each time the dimension of the growing concave recess naturally created on the insert and the amount of Hf oxide (HfO_2) collected on the nozzle surface. Morphological and compositional analysis of the tested electrodes and nozzles led to a detailed description of Hf erosion mechanisms,

modifications of the Hf insert morphological structure and effects of HfO_2 deposits on the nozzle inner surface. Conclusions can be drawn concerning the optimization of dimension of the initial recess of the Hf insert fit to avoid massive deposition of material on the nozzle inner surface that would cause a strong reduction of electrode and nozzle service life and a rapid degrading of cut quality.

In the second section of the present chapter, the microstructural modifications of the Hf insert in PAC electrodes operating at 250 A were experimentally investigated during first cycles, in order to understand those phenomena occurring on and under the Hf emissive surface and involved in the electrode erosion process. Standard electrodes were subjected to an increasing number of cutting cycles (*CCs*) on mild steel plates in realistic operative conditions, with oxygen/air as plasma/shield gas. Microstructural analysis was performed for each electrode at different erosion stages by means of scanning electron microscopy (SEM) equipped with energy dispersive spectroscopy (EDS) and Raman spectroscopy. Electrodes cross sections were also observed by means of optical microscopy (both in bright field and in reflected polarised light) after chemical etching. In the insert, three typical zones were found after cutting: monoclinic HfO_2 layer; thermally-modified transition zone with O_2-Hf solid solution; unmodified Hf. The erosion cavity and the oxide layer thickness increase with the number of cutting cycles. Macrocracking was observed in the oxide layer, while microcracking and grain growth were detected in the remelted Hf. Moreover, detachment was found at the Hf/Cu interface. Conclusions can be drawn on the erosion mechanism involved, also based on thermodynamics and kinetics of the Hf high temperature oxidation.

2.1 EVOLUTION OF THE Hf INSERT MORPHOLOGICAL STRUCTURE DURING FIRST CUTTING CYCLES

2.1.1 INTRODUCTION

It is known that the cavity deepening rate of the Hf emitter at high current level in oxidizing atmosphere is high during the first arc ignitions, to successively decrease and become approximately constant [2]. To avoid the negative effects induced by a natural deepening of the concave pit in an Hf insert initially flat, the emission surface

can be otherwise shaped with a concave recess, so neatly removing a volume of emissive material that would anyhow be removed during the first few starts in a random or massively disordered way, also badly conditioning the subsequent erosion process. When used in a torch, this solution accounts for a minimal deposition of emissive material on the nozzle, so reducing nozzle wear and double arcing phenomena, together with an increase in arc stability and cut quality.

With reference to patents (and related technology) aimed at the reduction of Hf cathode erosion at high current levels, two patents, strongly related to each other, are of particular interest among the ones described in the first chapter: “Improved electrode for high current density plasma arc torch” - *US 5,310,988* [35] and “Electrode for a plasma arc torch” - *US 5,464,962* [37], both published by Hypertherm. The first patent is aimed at improving the electrode useful life through the optimization of the Hf insert diameter “as a function of the level of a current carried out by the electrode”. The second patent is a continuation in part of the first one and it is aimed at “minimizing the deposition of high emissivity material on the nozzle” due to massive ejection phenomena that take place at high current levels during first starts, by shaping the emission surface in order to define a concave recess in the Hf insert.

As highlighted in the Section 1.3.2, the evolution of patent *status* in the EPO (European Patent Office) environment on this specific subject has opened up the possibility of producing and commercializing at an industrial level in Europe high current electrodes with an optimized initial recess depth on the Hf emitter surface; together with the necessity of validating a general experimental procedure supporting the design of the electrodes for each particular plasma source, with its typical set of geometrical and operating conditions.

In order to define electrode design procedures, Hf erosion phenomena on the emitter surface and modifications of the Hf insert morphological structure during first cutting cycles (*CCs*) were investigated under realistic operative conditions. In particular, the consequences of massive Hf ejections and the influence of the emissive surface initial shape on plasma arc behaviour and on Hf erosion rates was analyzed. Experimental results enabled us to validate the iterative experimental procedure for the optimization of the shape of the initial recess of the Hf insert as a function of the operating conditions and for a particular plasma source (without losing the generality of

approach), with the final aim of improving the service life and cut quality of consumables.

2.1.2 EXPERIMENTAL SET-UP

The erosion tests on the electrodes have been accomplished through a Cebora plasma cutting system, comprising the power supply Plasma Prof 254 HQC, equipped with the remote high frequency unit HV18 and the Gas Console PGC1-2 for manual gas settings, together with the multi-gas plasma torch CP251G (Fig. 2.1). The system can operate in the current range 25-250 A. Experiments have been accomplished under operative conditions typically used in cutting of MS plates thicker than 20 mm, with O_2 as plasma gas and air as shield gas at 250 A.

Fig. 2.1 Plasma Prof 254 HQC with the multi-gas plasma torch CP251G.

For every cycle, piercing at the optimum torch piercing stand-off is followed by 20 seconds of linear cutting at the optimum torch stand-off and at reduced velocity (0.3 m/min vs. the optimum of 2.1 m/min); cutting velocity is known for affecting only slightly erosion rate and the use of a reduced velocity accounts for metallic material savings. The standard electrodes tested with an arc current of 250 A use a press fit Hf insert with an emission surface diameter of 2 mm associated to a nozzle with 1.9 mm orifice diameter (Fig. 2.2).

Fig. 2.2 Standard Hf insert – Cu body electrode and Cu nozzle.

Morphological modifications of the tested electrodes at different *CCs* have been measured by means of a Hommelwerke T2000 contact profilometer (Fig. 2.3). Moreover, mean profiles of each electrode at subsequent erosion stages were calculated by interpolating six radial profiles from every 3D topography. Both the Hf volume eroded from the initially plane emissive insert, and the HfO_2 volume deposited on the cathode surface, were detected. Scanning electron microscopy (SEM) of the tested electrodes has been performed to validate the topographies reconstruction. Qualitative evaluation of the HfO_2 deposition on the inner nozzle surface has been carried out by stereo-microscopy using a new nozzle at each *CC*.

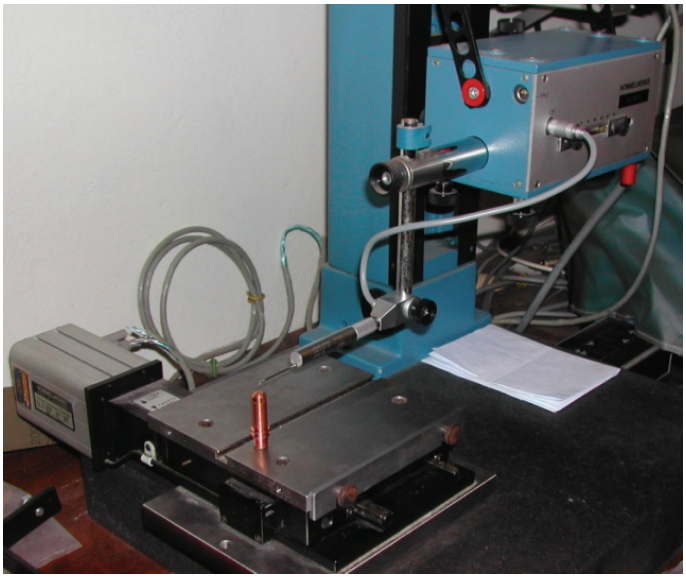

Fig. 2.3 Stylus profilometer measurement set-up.

2.1.3 EXPERIMENTAL PROCEDURE

In this work a modified experimental procedure will be presented, with respect to the one described in the abovementioned patents, highlighting the reasons for the proposed changes and their effect on the optimization process.

2.1.3.1 HYPERTHERM INC. EXPERIMENTAL PROCEDURE

In particular, the Hypertherm patent "Electrode for a plasma arc torch" - *US 5,464,962* describes a try-and-fail experimental procedure that is to be carried out in order to optimize the initially concave shape of the emission surface "as a function of the operating current level, the diameter of the insert, and the plasma gas flow pattern in the torch". The procedure starts with a first trial machining of the electrode tip to establish the concave insert recess on the emission surface and testing the electrode with subsequent *CCs* in realistic operating conditions. The recess shape and the nozzle condition were checked after each *CC*. If double arcing consequent to massive Hf deposition on the nozzle took place, the erosion test was stopped and the experimental procedure was re-started with a deeper trail concave recess, until double arcing phenomena would disappear. The initial shape of the concave recess that gave inducing the absence of double arcing would be selected as optimal.

2.1.3.2 MODIFIED EXPERIMENTAL PROCEDURE

In general terms, the optimal shape of the initial recess of the Hf insert is strongly dependent upon "typical operating and geometric conditions" of the torch being optimized. Moreover, the recess shape deriving from the Hypertherm experimental procedure could be significantly affected by the initial trial one.

For these reasons, a modified experimental procedure is proposed here, starting the investigation with an initially plane insert emission surface and analyzing the evolution of the recess depth naturally created during the first few *CCs* while using these information for defining subsequent optimization steps.

The proposed modified experimental procedure can be divided into different stages. The first stage is characterized by a series of tests accomplished on electrodes with an initially planar insert emission surface. The erosion tests were stopped after

every *CC* to check the eroded Hf volume and the overall nozzle condition. Modifications of the Hf insert morphological structure were also monitored and this first test was stopped when the emissive surface morphology reached a stabilization phase as a function of the number of *CCs*; that is to say when massive Hf ejections stop and only slight ejections of Hf-based solid particles take place; this phenomenon being related to the cyclic erosion process leading to a constant deepening rate of the cavity for the electrode's entire service life. The dimension of the recess that was naturally created on the emissive surface at the end of the first stage was taken as reference point to design some intermediate spherical recesses to be tested on erosion during *CCs* in the second stage of the procedure. The Hf eroded volume, the overall nozzle condition and the Hf insert morphological structure evolution over *CCs* were monitored, in order to identify the stabilization phase for each tested electrode. The modifications occurring on the emissive surface morphology of tested electrodes allowed the identification of the optimal spherical recess.

2.1.4 BEHAVIOUR AND ANALYSIS OF ELECTRODES WITH NO INITIAL RECESS

2.1.4.1 ELECTRODE EROSION TESTS

Erosion tests on electrodes with no initial recess have been accomplished in order to study the behaviour of the Hf insert during first ignitions under real cutting conditions. The current level has been set at 250 A; piercing and cutting (20 s) phases on a 25 mm thick MS plate have been accomplished under the optimum conditions for stand-off and gas inlet pressures.

At the first stage, three series of tests were carried out. For each series, five tests were completed, each characterized by an increasing number of *CCs* to which each electrode was subjected; each test has been started with a new electrode, associated with a new nozzle for each *CC*, in order to later investigate on the quantity of Hf-based particles deposited on the nozzle during each arcing process. Overall, 15 electrodes and 45 nozzles were used for each test. Unfortunately, the complexity of the phenomena involved in cathode erosion [2, 11, 12, 14] during first cycles allows only a partial repeatability of the effects related to concave recess generation and morphological modifications in the Hf pellet.

Fig. 2.4 shows the erosion cavity depth for each electrode of the above-mentioned test series. These first results highlighted how the erosion morphology and cavity depth of each emissive insert after a certain number of *CCs* were strongly affected from the electrode status at the end of the previous CC. This strong dependence leads to difficulties in reconstructing the typical behaviour of one electrode over five *CCs*, using data coming from a limited number of electrodes (for example, five) ideally identical at the beginning of their service life.

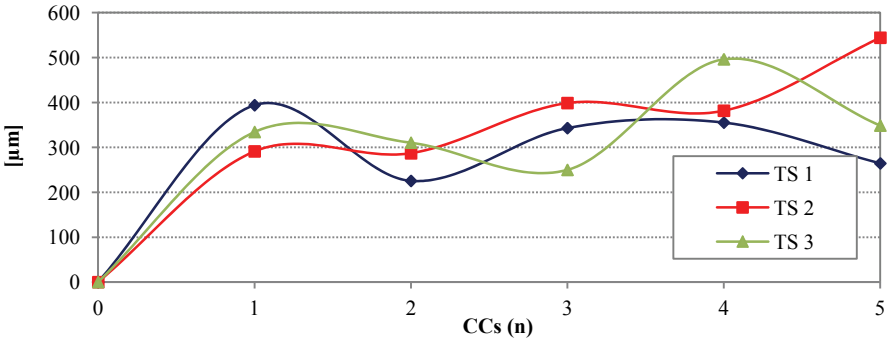

Fig. 2.4 Erosion cavity depth as a function of *CCs* for TS1-TS3.

Thus, in order to better understand the erosion mechanisms that each electrode underwent during first cycles, four more tests (E1–E4) were accomplished with a different experimental procedure. For each test, one electrode with no initial recess underwent five *CCs*; a new nozzle was used for every *CC*. 3D topographies and volume measurements were recorded for each electrode after every *CC* (Fig. 2.5).

2.1.4.2 Morphological and compositional analysis

After the first arc ignition, all the tested electrodes evidenced the presence of a concave recess in the Hf emissive insert, and an annular zone with Hf deposit surrounding the insert boundaries on the cathode surface, as shown for electrodes E1 and E2 in the topographies in Fig. 2.6. Moreover, the SEM macrograph in Fig. 2.7 exhibits the presence of a fine dispersion of HfO_2 surrounding the massive Hf deposit, together with HfO_2 droplets. Finally, some of the Hf-based particles ejected from the insert are deposited on the inner nozzle surface, as shown in Fig. 2.8 *a*.

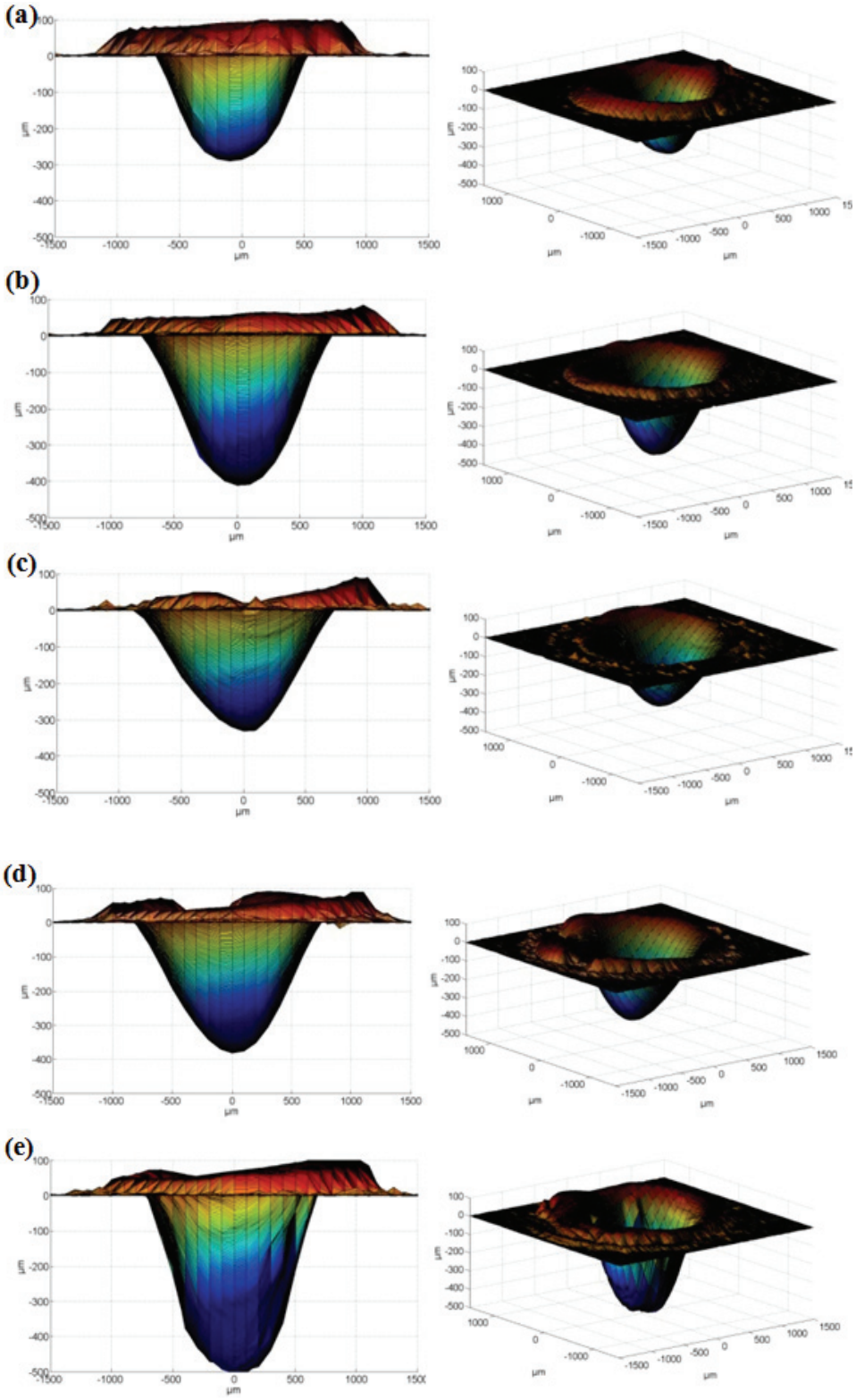

Fig. 2.5 Different views of the electrode E1 topography after (*a*) 1 *CC*, (*b*) 2 *CCs*, (*c*) 3 *CCs*, (*d*) 4 *CCs* and (*e*) 5 *CCs*.

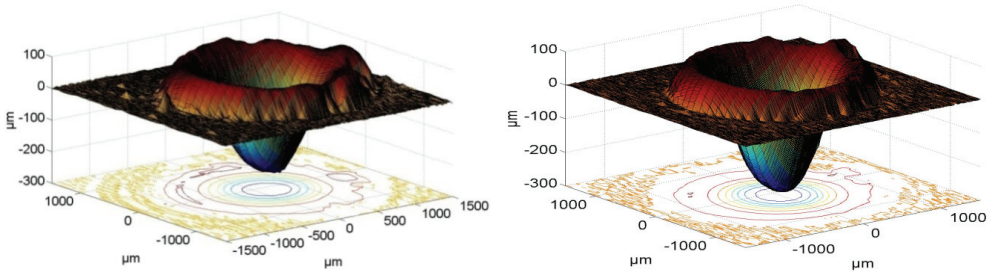

Fig. 2.6. 3D topographies and contour map views of the emissive surface of electrode (*a*) E1 and (*b*) E2 after 1 *CC*.

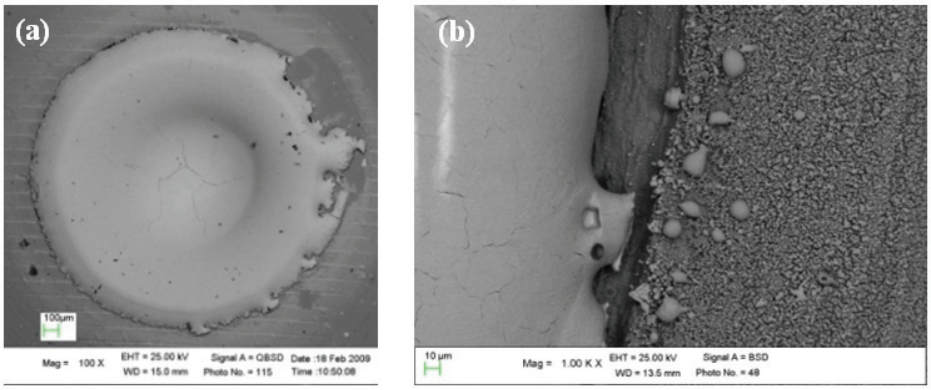

Fig. 2.7 (*a*) SEM micrograph of electrode *E1* after 1 *CC* and (*b*) particular of the finely dispersed HfO_2 and droplets around the deposited hafnium.

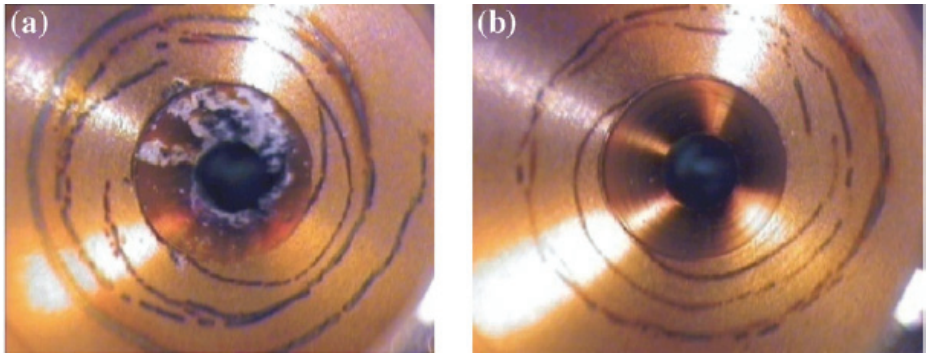

Fig. 2.8. Stereomicroscopy images of the inner surfaces of nozzles associated with electrode E1 after (*a*) 2 *CCs* and (*b*) 3 *CCs*.

Fig. 2.9 describes the detailed evolution of the cross-sectional mean profiles (calculated by interpolating six radial profiles from each topography) of all the tested electrodes as a function of the number of *CCs*. Fig. 2.10 describes the detailed evolution of the volume measurements, computed by integrating the electrode surfaces from each topography, of all the tested electrodes, as a function of the number of *CCs*. In the histograms of Fig. 2.10, the erosion volume is a measure of the concave recess naturally established on the emitter surface, while the deposited volume is the volume of the Hf

deposited on the electrode surface, around the emitter surface; the net volume is the difference between the erosion volume and the deposited volume.

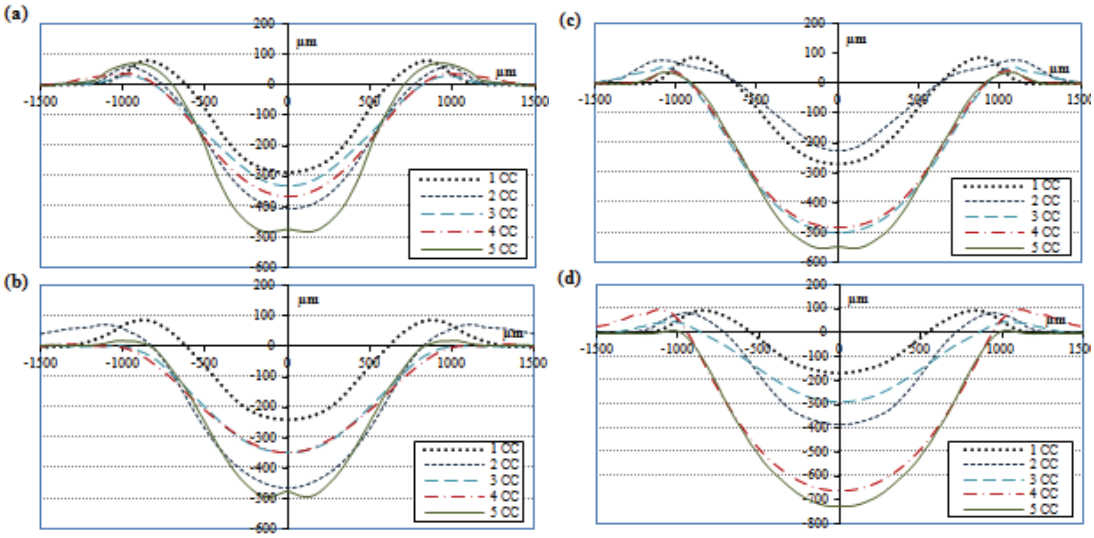

Fig. 2.9 Trend of the cross sectional mean profiles, from 1 *CC* to 5 *CCs*, of the electrodes *(a) E1*, *(b) E2*, *(c) E3* and *(d) E4*.

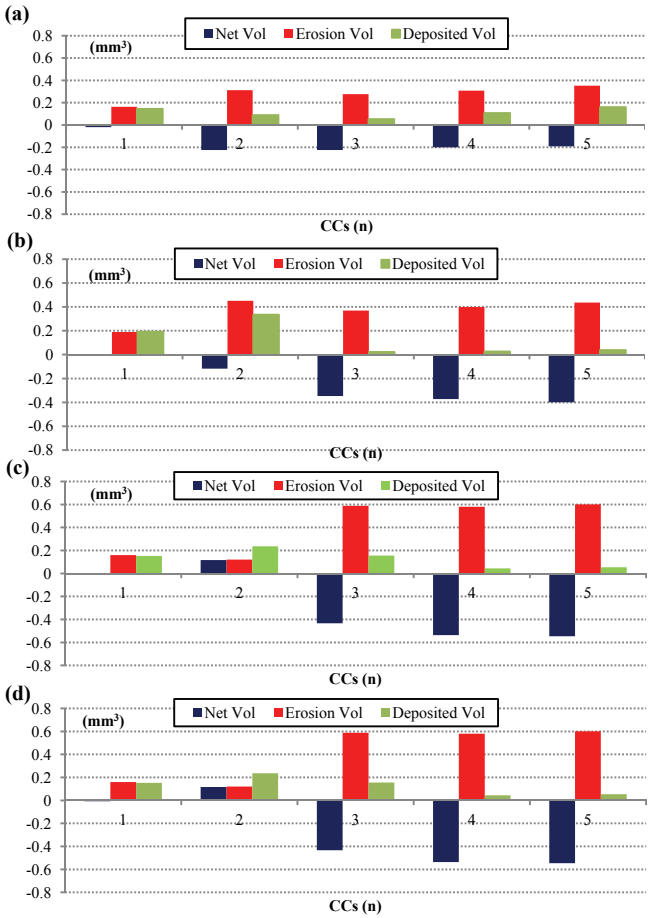

Fig. 2.10 Trend of the measured volumes, from 1 *CC* to 5 *CCs*, of the electrodes *(a) E1*, *(b) E2*, *(c) E3* and *(d) E4*

For E3, after 2 *CCs*, and E4, after 1 *CCs*, the deposited volumes exceed the erosion ones; this result could be explained by taking into account the microstructure of the Hf insert after a few *CCs*, as shown in the cross-sectional view of Fig. 2.11. It is possible to observe three zones: unmodified Hf, thermally affected Hf and a HfO_2 layer. The latter can be characterized by cracking and porosity, while the Hf affected by thermal cycling can be characterized by cavities (as previously shown in [12]) due to the oxygen diffusion and oxide formation processes. These phenomena, together with the higher density of the pure Hf (13.31 g cm^{-3} [8]) with respect to the density of monoclinic HfO_2 (9.7 g cm^{-3} [52]), could affect the amount of hafnium oxide deposited on the cathode surface, leading to an increase in both the measured values of the deposited volumes and in the thickness of the superficial layer of the emissive insert, so decreasing the measured erosion volumes. The microstructure of the insert after cutting will be deeply analyzed in the second section of this Chapter.

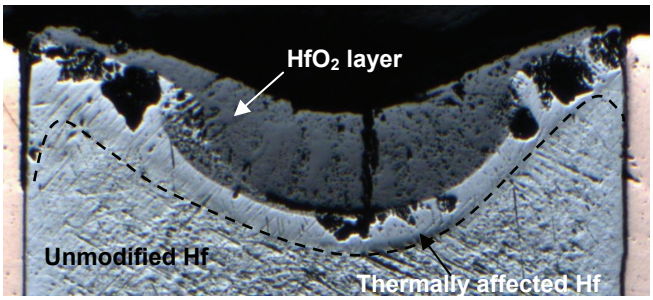

Fig. 2.11 Cross sectional view of an Hf insert after 3 *CCs*, showing the typical microstructure comprising unmodified Hf, thermally affected Hf and HfO_2 layer.

The evolution of the eroded volumes (Fig. 2.12 *a*) of the four examined electrodes (which show a trend similar to the one of the maximum cavity depth, Fig. 2.12 *b*) suggests how the erosion behaviour of each insert is only partially determined by the morphology of the emitting surface as measured at the previous step. For 3 out of 4 electrodes (E1, E2, E4), the deepening of the erosion cavity increases up to 2 *CCs*; between 2 and 3 *CCs* the maximum erosion depth tends to slightly decrease, as does the erosion volume. Thereafter, erosion depth for electrodes E1 and E2 increases slightly up to five *CCs*, achieving depth values similar to those measured after two *CCs* (about 470 μm, Fig. 2.12).

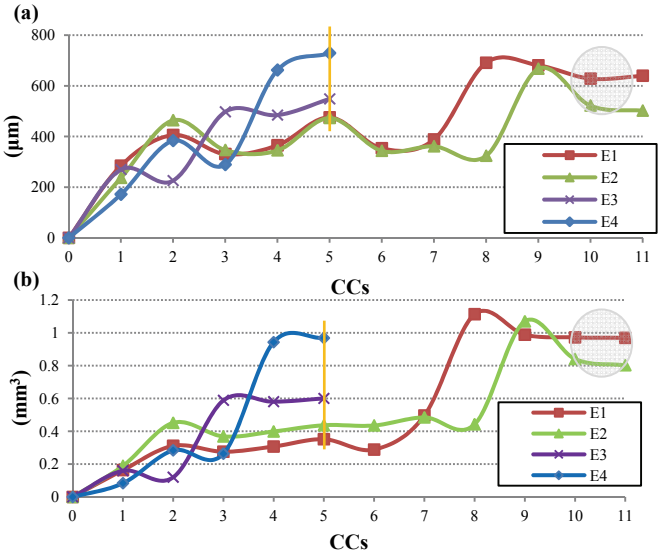

Fig. 2.12. Trends of *(a)* the maximum recess depth and of *(b)* the calculated eroded volumes, as a function of the number of *CCs*, for electrodes with no initial recess.

In contrast, electrode E4 cavity depth changes from 290 to 660 μm between three and four *CCs*, whilst the recess depth tends to remain almost constant thereafter. Electrode E3 behaves differently, as the recess depth decreases from one to two *CCs*, then deepens after three *CCs*, whereas it remains almost constant at about 500 μm between three and five *CCs*. Qualitative correspondence was found between the amount of Hf detected on the nozzles' inner surfaces and the deepening rate of the erosion cavity: massive HfO_2 deposits were found when the cavity depth increased significantly (Fig. 2.8 *a*), while nozzle inner surfaces were found to be almost clean when the erosion volume and the recess depth decreased or remained almost constant (Fig. 2.8 *b*). Only for electrode E3 a limited amount of Hf was detected on the nozzle inner surface after two *CCs*, whilst the erosion volume decreased. Since E3 underwent a strong deepening between two and three *CCs*, this decrease in the erosion volume is related to the microstructure of the HfO_2 layer and to the thermally affected Hf (as already shown in Fig. 2.11), which were probably particularly affected by cracking and porosity at that stage.

These results show how the low repeatability of the erosion process (due to the complex interactions and phenomena taking place in the plasma chamber) is further reduced by the process of formation of the natural concave recess, when starting with an initially planar emitting surface. The evolution of the recess shape, together with the erosion volume and nozzle inner surface analysis, allow some considerations about the

optimal initial shape that an emissive insert should be given when operating at high currents in PAC [35, 37]. Electrodes E1 and E2, between two and five *CCs*, maintained their cavity depth and erosion volume as almost constant, while no or extremely limited Hf emission and deposition on the nozzle inner surface was detected, showing how the Hf volumes eroded during the first two *CCs* could be removed from an optimized emissive insert. Due to this particular behaviour, they have been tested for an increased number of starts, in order to better study the evolution of the spontaneously established recess, and they have been considered as a reference point to start an experimental procedure for the optimization of the recess shape. The design of the emissive surface could be deduced from the analysis of the 3D topographies and mean profiles carried out for the considered phases.

2.1.4.3 INCREASED NUMBER OF CUTTING CYCLES

Electrodes E1 and E2 were subjected to 11 *CCs*. They are both characterized by massive Hf ejection events after the first five *CCs*; in particular, the eroded volumes skip from 0.31–0.43 mm^3 to about 1 mm^3 and the maximum recess depth reaches a level of about 0.7 mm. As shown in Fig. 2.12, the levels of eroded volume and maximum recess depth that electrodes E1 and E2 reach, in a stabilized manner, after 11 *CCs* are similar to those reached after five *CCs*, with a nonlinear trend, by electrodes E3 and E4. They both reach the stabilization of the emissive surface morphological structure after nine *CCs*.

2.1.5 BEHAVIOUR OF ELECTRODES WITH INITIALLY OPTIMIZED RECESS

On the basis of the results obtained from tests on electrodes E1 and E2 after 5 *CCs*, two (non-trial) spherical recess shapes have been designed:

- from electrode E2 a spherical recess with an initial recess depth of about 500 μm and an initial recess volume of 0,43 mm^3 (electrode Es1);
- from electrode E1 a spherical recess with an initial recess depth of about 400 μm and an initial recess volume of 0,31 mm^3 (electrode Es2).

Both electrodes were subjected to subsequent *CCs* in order to find stabilization in the emissive surface morphology. After 5 *CCs* both electrodes reached the stabilization

phase and were characterized by similar levels of maximum recess depth and eroded volume.

In particular, at the end of the test series, results were as follows (Fig.s 2.13 and 2.14).

Electrode Es1 was characterized by:

- a reduction of the maximum recess depth (from 510 µm to 421 µm)
- a slight increase of the recess volume (from 0,43 mm^3 to 0,55 mm^3)

Electrode Es2 was characterized by:

- a slight increase of the maximum recess depth (from 395 µm to 432 µm)
- a significant increase of the recess volume (from 0,31 mm^3 to 0,53 mm^3)

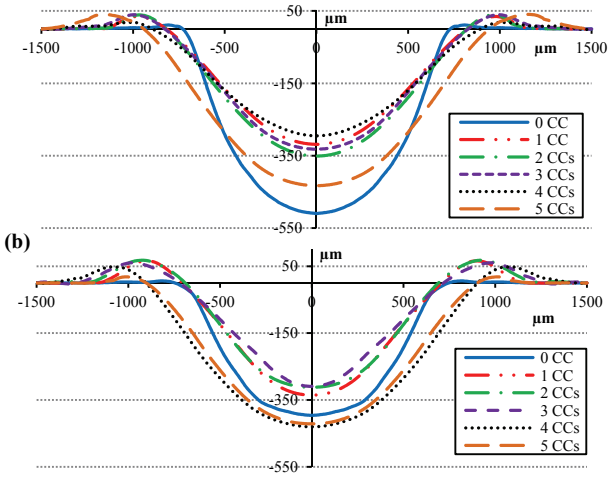

Fig. 2.13. Trends of the cross sectional mean profiles, as a function of the number of *CCs*, for electrodes *(a) Es1* and *(b) Es2*.

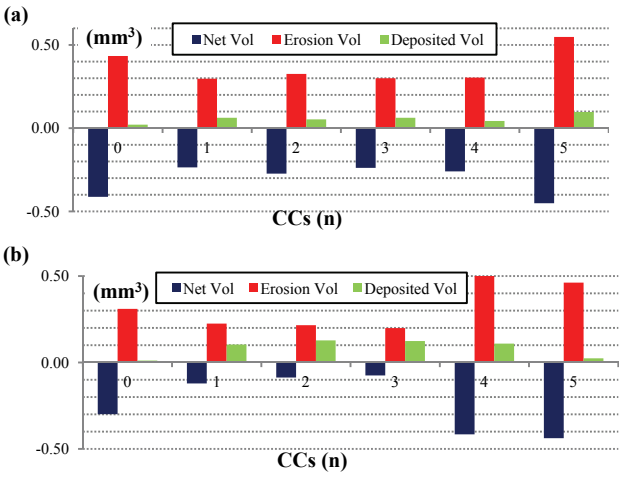

Fig. 2.14. Trends of the measured volumes, as a function of the number of *CCs*, for electrodes *(a) Es1* and *(b) Es2*.

The initial Hf emitter surface morphology of electrodes Es1 and Es2 closely reproduces the recess depth naturally created on electrodes E1 and E2 after five *CCs*. For this reason, electrodes Es1 and Es2 after five *CCs* and electrodes E1 and E2 after 10 *CCS* can be considered at the same service life stage; therefore, it is significant to evaluate differences between their resulting morphology of the emission surface at that life stage, in order to highlight the influence of the emissive surface initial shape on the electrode behaviour during first *CCs*. Experimental evidence shows that for both electrode Es1 and Es2 the erode volume levels and the recess depth were significantly reduced with respect to those reached on E1 and E2 after 10 *CCs* (Fig. 2.15). Moreover, both eroded volume and maximum recess depth levels of Es1 and Es2 reached a similar value after erosion tests, although fresh electrodes were characterized by a slightly different initial shape of the spherical recess. This result enabled us to consider the recess shape obtained at this stage with electrodes Es1 and Es2 as a reference point to design the optimized spherical recess.

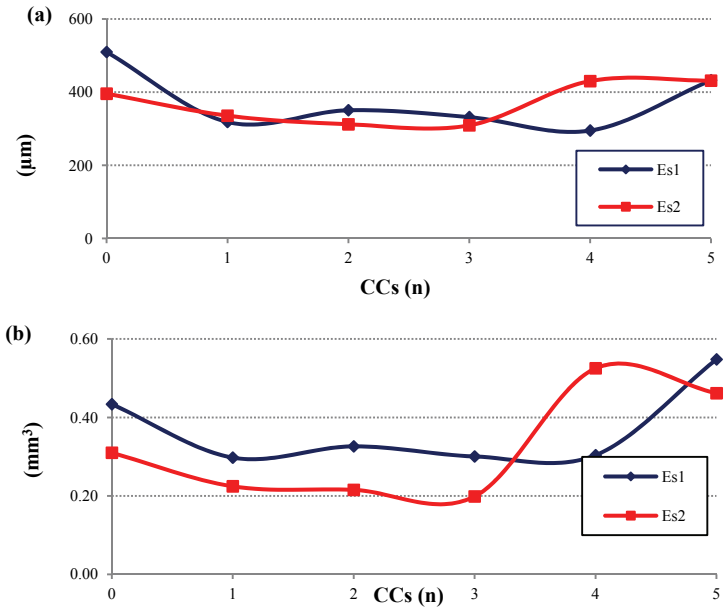

Fig. 2.15. Trends of *(a)* the maximum recess depth and of *(b)* the measured eroded volumes, as a function of the number of *CCs*, for electrodes *Es1* and *Es2*

2.1.6 CONCLUSIONS

The behaviour of high current electrodes in plasma arc cutting were investigated by means of morphological analysis during first cycles. An iterative experimental

procedure for the optimization of the initial recess shape of the Hf insert have been validated, starting the investigation with an initially plane emission surface and defining subsequent optimization steps on the basis of the evolution of the recess depth naturally created during the first few *CCs*.

The process of cathode erosion at this stage was found to be only partially deterministic. Thus, 3-D morphology of a set of electrodes (E1 - E4) was reconstructed after each of 5 cutting cycles. The results obtained during tests with electrodes characterized by an initially planar emission surface were a reference point for the design of two spherical recess shapes (Es1 - Es2), also tested on erosion during first cutting cycles. Results obtained from tests on electrodes Es1 and Es2 enabled us to identify optimal values for both the maximum recess depth and the erosion volume of the initial recess, for the specific geometrical and operative conditions under which erosion tests were accomplished.

Experimental evidences showed that an initial planar emission surface gives rise to massive Hf ejections during first *CCs*, inducing a preferred concave shape on the emitter, with consequent massive Hf deposition on the inner nozzle surfaces that negatively affect cut quality and nozzle service life; in patent literature, both these effects have been highlighted: as previously showed, by the abovementioned Hypertherm experimental procedure, but also in the Kabushiki Kaisha Komatsu patent "*Transferred Plasma Arc Torch*" - US 5214263 (May 25, 1993) [53]. In particular, the Komatsu patent highlights that any loss of axial-symmetry in the plasma chamber can negatively affect cut quality; experimental results reported in the patent are mainly based on an artificially induced loss of axial-symmetry of the electrode, by grinding out a portion of the tip of the electrode holder; but it is well known that the deposition on the nozzle inner surfaces of Hf-based products can raise similar consequences.

Moreover, the modified experimental procedure developed in the present work showed that the optimization of the initial recess shape of the Hf emitter surface not only minimizes the deposition of HfO_2 on the nozzle, as affirmed in [37], but positively affects the subsequent trend of the Hf erosion rate, improving the electrode's service life on the whole.

2.2 MICROSTRUCTURAL MODIFICATIONS OF HAFNIUM CATHODES DURING FIRST CYCLES

2.2.1. INTRODUCTION

The mechanisms involved in the erosion phenomena of a PAC cathode have yet to be fully understood, together with factors that positively or negatively influence the erosion rate. As discussed in the first chapter, cathode erosion results from the different contribution of constant current erosion in steady states and cyclic erosion during transients. The different erosion contributions result in the formation of a concave cavity on the Hf emitter, whose deepening is particularly high during first cycles, as highlighted in Section 2.1 and in [54], and a significant amount of the emitted Hf oxide deposits on the electrode copper body and on the nozzle inner surface, negatively affecting both the cut quality and the consumables service life [9].

For all the above mentioned reasons, it is of particular importance the investigation of the erosion mechanisms during first cutting cycles. Although different papers addressed the issue of hafnium cathode erosion [2, 11, 12, 14] none of these focused on the phenomena taking place under the Hf surface from a microstructural point of view.

The objective of this section was to investigate the microstructural modifications occurring in Hf cathodes during first plasma arc cutting (PAC) cycles at high current levels in oxidizing atmosphere, in order to gain further insights and to draw conclusions concerning the factors involved in the erosion mechanism.

2.2.2 EXPERIMENTAL SET-UP

Erosion tests due to cutting cycles (*CCs*) were performed on a Cebora plasma cutting system, able to operate in the current range 25-250A, comprising the power supply Plasma Prof 264 HQC, a remote high frequency unit HV18, a Gas Console PGC1-2 for manual gas settings and a multi-gas plasma torch CP251G. All the tests were carried out at 250 A, under those conditions typically used when cutting mild steel plates thicker than 20 mm, by means of O_2 as plasma gas and air as shield gas. Pressure in the plasma chamber was set at 5.4 bar. In these experimental tests, current and pressure transients were optimized to achieve a good compromise between arc stability

and balance of forces acting on the insert surface. Current was linearly increased to the set-up value in about 0.4 s during arc on, and linearly ramped-down in about 40 ms during arc-off. Every CC consists of a piercing and a 20 s linear cut performed at 0.3 m/min, both at the optimal stand-off distance from the plate. This velocity is reduced with respect to the optimal one (2.1 m/min) in order to save material, as it is known that it doesn't affect significantly the erosion rate.

The electrodes investigated in the present work comprise a water cooled oxygen-free Cu holder and a press-fit Hf insert with a 2 mm emission diameter. The press fit Hf insert was fabricated from commercially pure Hf wire (Zr < 2 wt%). Nozzles associated to each electrode were characterized by a 1.9 mm orifice. A series of 6 electrodes was tested at 1 to 5 and at 13 *CCs*. The surface of each electrode at different erosion stages were analyzed by means of scanning electron microscopy (SEM), performing the elemental analysis through energy dispersive spectroscopy (EDS), whilst phase composition was analysed by micro-Raman spectroscopy (λ=514.5 nm).

In order to characterize the electrode cross section, the portions of the cathodes comprising the Hf insert were first cut and then mounted in epoxy resin (Fig. 2.16). 320P grit paper sheets were used to polish the samples, parallel to the electrode axis, until the Hf insert was reached. Finer grit paper sheets (up to 2000P) were used when approaching the insert cross section, while mirror polishing was obtained by means of 3 μm and 1 μm diamond suspensions.

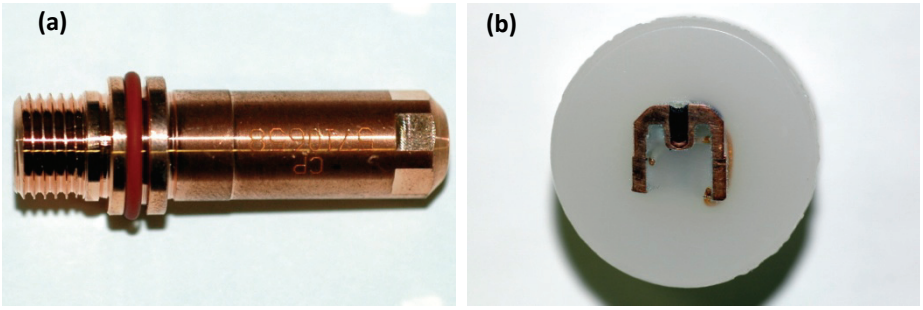

Fig. 2.16 Standard electrode lateral view (*a*) and cross section mounted in epoxy resin (*b*).

Cross sections of electrodes, which underwent an increasing number of *CCs*, were observed by means of Scanning Electron Microscopy (SEM) and Optical Microscopy (OM). Chemical etching was accomplished according to ASTM E 407-07, so as to identify grain boundaries and to address grain growth phenomena: Cu etching

was performed by means of an acidic saturated solution of $FeCl_3$ in ethanol, whereas Hf was etched by an acidic solution of 40%vol. Hf, 40%vol. HCl and 20%vol. HNO_3. Etched cross sections were observed by means of OM under reflected polarized light. The oxide layer thickness and the length of the Cu/Hf detachment were evaluated at different erosion stages.

2.2.3 RESULTS AND DISCUSSION

2.2.3.1 AS-SUPPLIED ELECTRODES

When observed in the as-supplied condition (Fig. 2.17), the insert surface appears to be flat (as shown by the cross-section in Fig. 2.17 *c*), except for concentric lines due to the final machining process (Fig. 2.17 *a-b*). The contact between the copper holder and the Hf insert is provided around the entire pellet circumference.

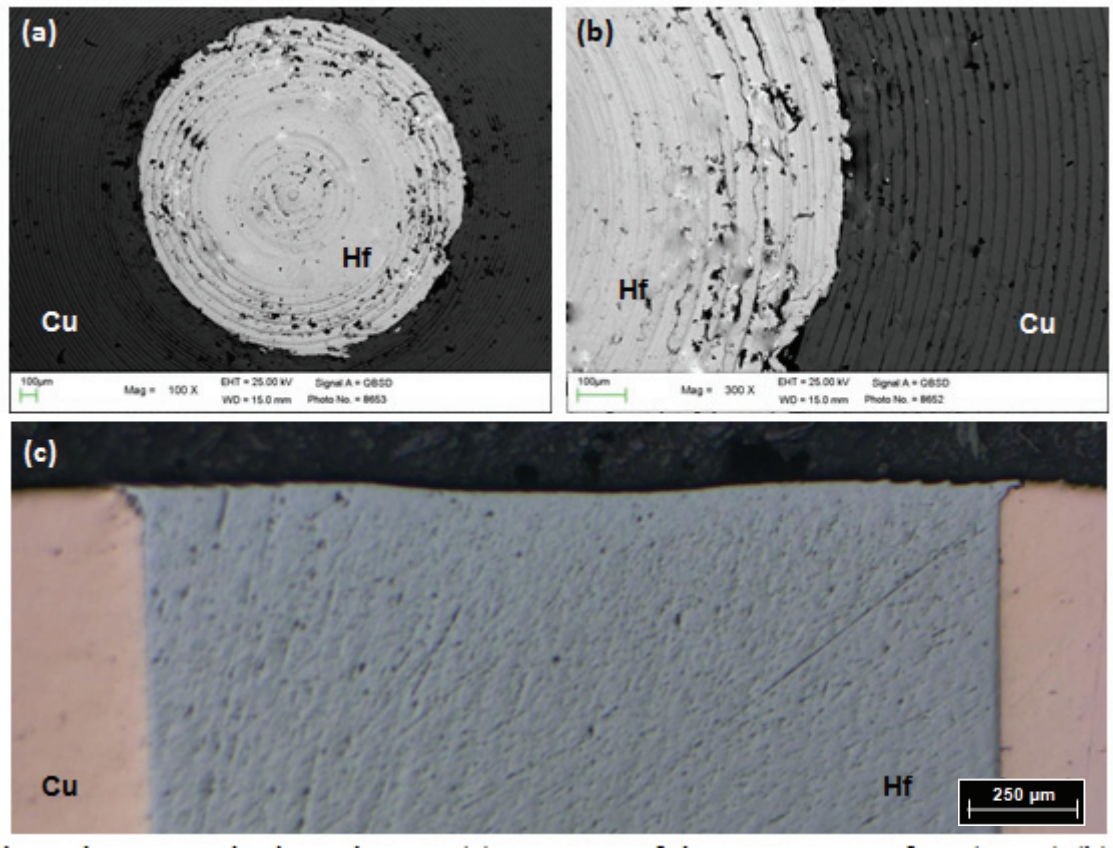

Fig. 2.17. Electrode in the as supplied conditions: (*a*) top view of the emissive surface (SEM); (*b*) concentric lines due to the final machining process (SEM); (*c*) Hf insert cross section (OM).

2.2.3.2 ELECTRODE AFTER 1 *CC*

After 1 *CC*, finely dispersed Hf-based particles and small droplets were found on the copper holder around the emissive Hf surface, as shown with different magnifications in Figs. 2.18 *a-b*. The morphology of the insert surface suggests that the top layer underwent melting, and the macroscopic cracks in the central area (Fig. 2.18 *a*) formed during solidification. Observing the dispersion of the Hf-based particles on the copper sleeve in Fig. 2.18 *a*, it is also possible to notice the presence of a tangential component in the ejection trajectory ("swirl trajectories" in Fig. 2.18 *a*), which is possibly related to dragging effect of the gas swirl in the plasma chamber. However, once ejected, small particles could be entrained in a vortex or, more generally, run through a complex path before being deposited on the copper body with a swirl-like trajectory. Thus, no direct relationship between the small particle ejection and the aerodynamic swirl drag can be proved. Nevertheless, it is known that the presence of the plasma gas swirl badly affects cathode erosion [14], although it allows for the on-axis stabilization of the arc, nozzle protection and improvement of the cutting quality [2]. The electrode cross section, observed with OM, shows the formation of a slightly concave recess in the centre of the insert. Three different typical zones can be identified on the basis of microstructural observation and by means of the EDS analysis (Fig. 2.18 *c*): (a) surface layer of HfO_2, whose thickness is approximately constant (70 μm in the insert centre); (b) a thermally modified zone, with a denser appearance, where oxygen forms a solid solution with hafnium, also affected by the development of cracks and discontinuities due to oxygen diffusion and oxide formation process; (c) unmodified Hf.

The formation of Hf oxide is expected, as Hf begins to react with air or oxygen to form HfO_2 at about 400 °C. The free-energy/temperature diagrams [55] show that Hf forms highly stable HfO_2; the stability of this oxide decreases with increasing temperature, but this is balanced by the higher oxidation rate. The presence of HfO_2in the top layer, which, as previously discussed, underwent melting (Fig. 2.18 *a*), suggests that in this zone temperatures achieved at least the melting point of this oxide (2812°C). From the analysis of the ejected Hf-based products on the electrode sleeve after 1 *CC*, the single droplets can be associated to the different cutting phases. For instance, the Hf oxide droplet shown in the cross section of Fig. 2.19 *a* and *b* is covered by a fine dispersion of HfO_2. Since this dispersion is believed to be mainly associated to

evaporation phenomena [2] during the steady state cutting phase, one possible conclusion is that this droplet was ejected during the arc-on phase, than covered by the fine Hf-based dispersion. Both covered and non-covered (Fig. 2.19 *c*) HfO_2 droplets were found in the 1 *CC* case, confirming that the massive ejection of emissive material during first cycles occurs both during the arc-on and arc-off phases [11].

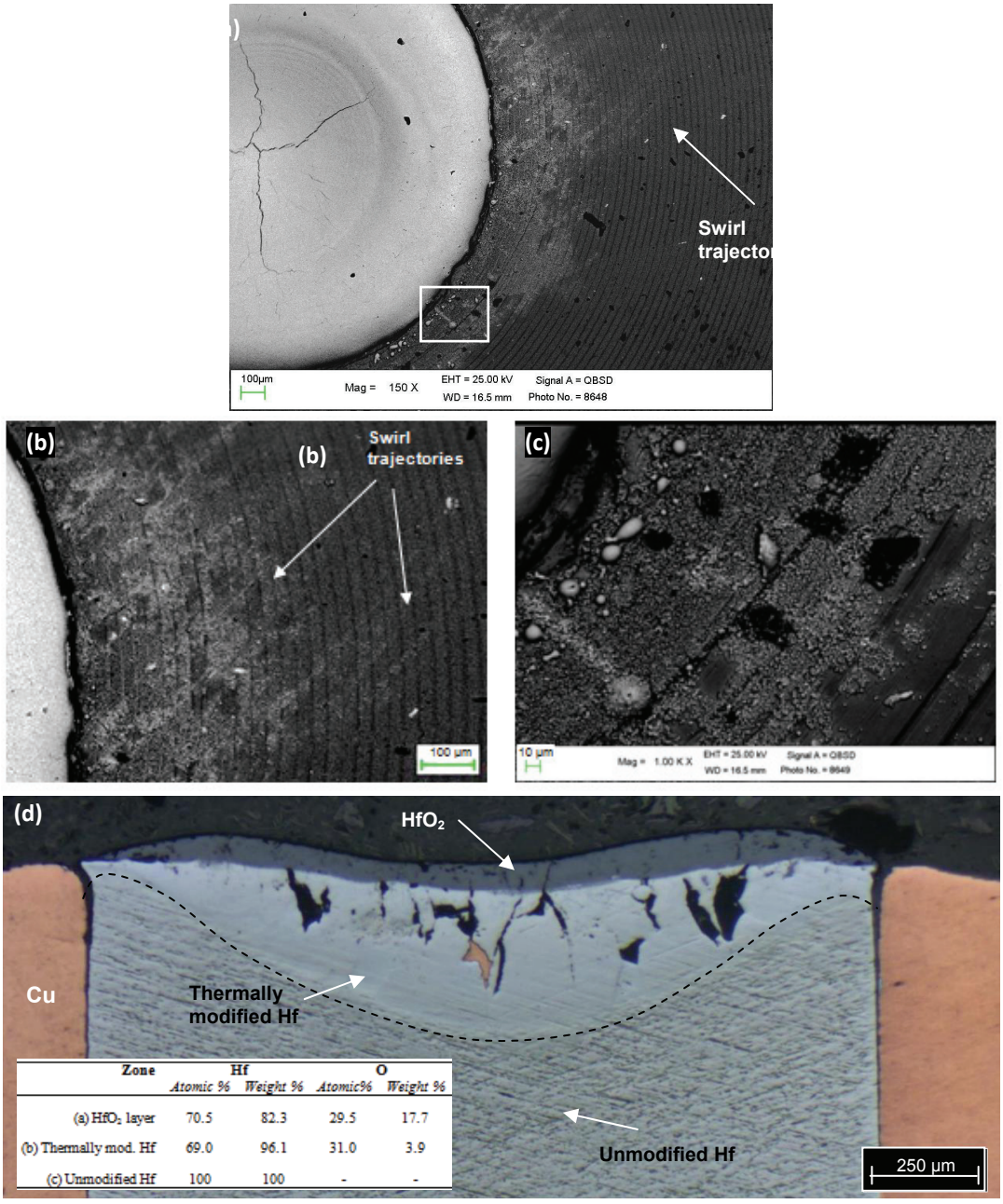

Zone	Hf		O	
	Atomic %	*Weight %*	*Atomic%*	*Weight %*
(a) HfO_2 layer	70.5	82.3	29.5	17.7
(b) Thermally mod. Hf	69.0	96.1	31.0	3.9
(c) Unmodified Hf	100	100	-	-

Fig. 2.18 Electrode after 1 cutting cycle (*CC)*: (*a*) SEM top view; (*b*) detail of swirl trajectories; (*c*) detail of the emitted Hf-based products (white-contoured area in (*a*)); (*d*) insert cross section (OM) and EDS analysis.

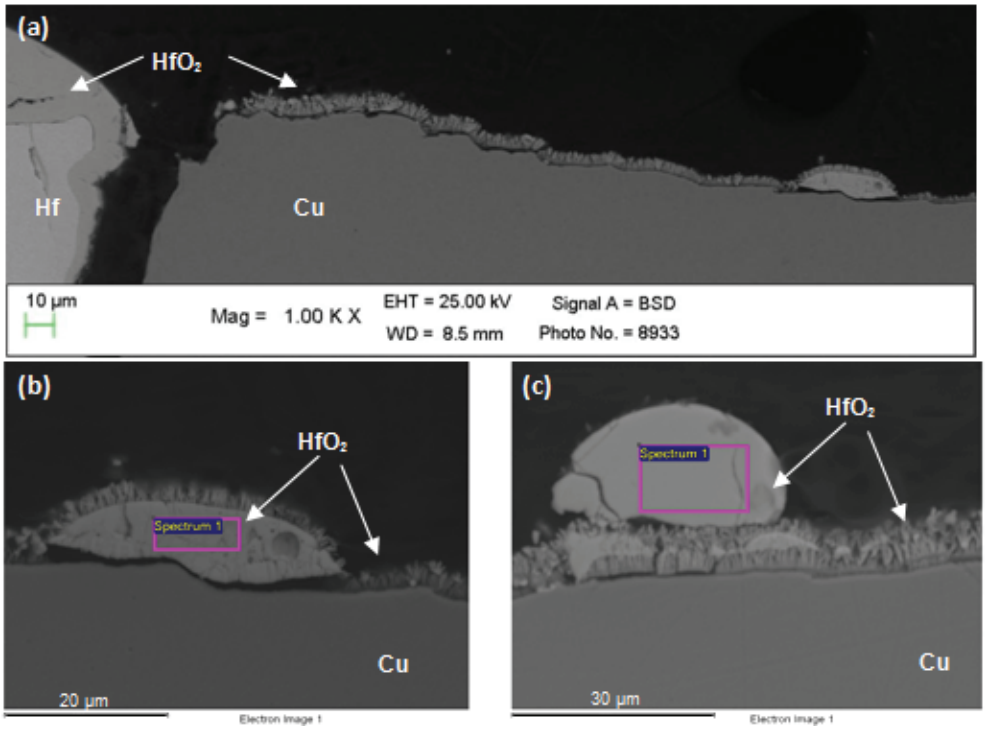

Fig. 2.19 (*a*) Detail of the electrode cross section showing the ejected Hf-based products and detachment at the Cu/Hf interface; (*b*) ejected particle covered by fine HfO_2 dispersion; (*c*) uncovered ejected droplet.

Raman spectra were taken from different zones (Fig. 2.20): on the emitting surface, on the finely dispersed particles and on the ejected droplets, allowing the identification of the examined material as monoclinic HfO_2, with possible traces of the tetragonal allomorph (peak at 270 cm^{-1} in Fig. 2.20). It is indeed known from the Hf-O phase diagram that the hafnium oxide has different allomorphs, ranging from cubic lattice at high temperatures, to tetragonal and then monoclinic at low temperatures [56].

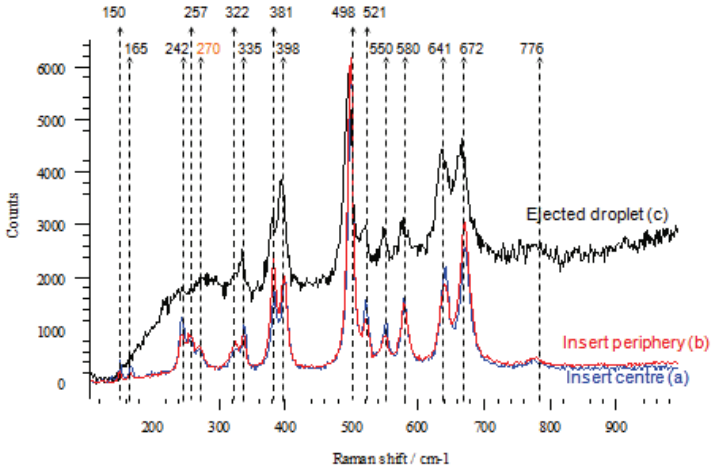

Fig. 2.20 Raman spectra (λ=514.5 nm) measured on: (*a*) insert centre, (*b*) insert periphery and (*c*) Hf-based ejected droplet.

2.2.3.3 ELECTRODE AFTER 5 *CCS*

After 5 *CCs*, the electrode surface still shows the presence of finely dispersed HfO_2 (Fig. 2.21 *a*), but the amount of ejected droplets is higher than in the 1 *CC* electrode surface. Furthermore, Fig. 2.21 *b* shows a relatively large HfO_2 droplet covered by a fine dispersion of smaller particles. This particle could have been ejected in any of the previous cutting phase, except for the last arc-off transient.

The electrode cross section in Fig. 2.21 *c* shows the deepening of the concave erosion cavity. The oxide layer thickness is not anymore homogeneous, as it increased remarkably in the central part of the insert, measuring 320 µm on the axis. This central depth increase can be explained as a consequence of an inward convective motion of the molten HfO_2 pool, caused by the Marangoni effect and the electromagnetic force that could facilitate the heat transfer from the surface to the bulk of the insert, as shown in [57] for a plasma welding molten pool. Moreover, the oxide layer was affected by deep cracking due to thermal cycling.

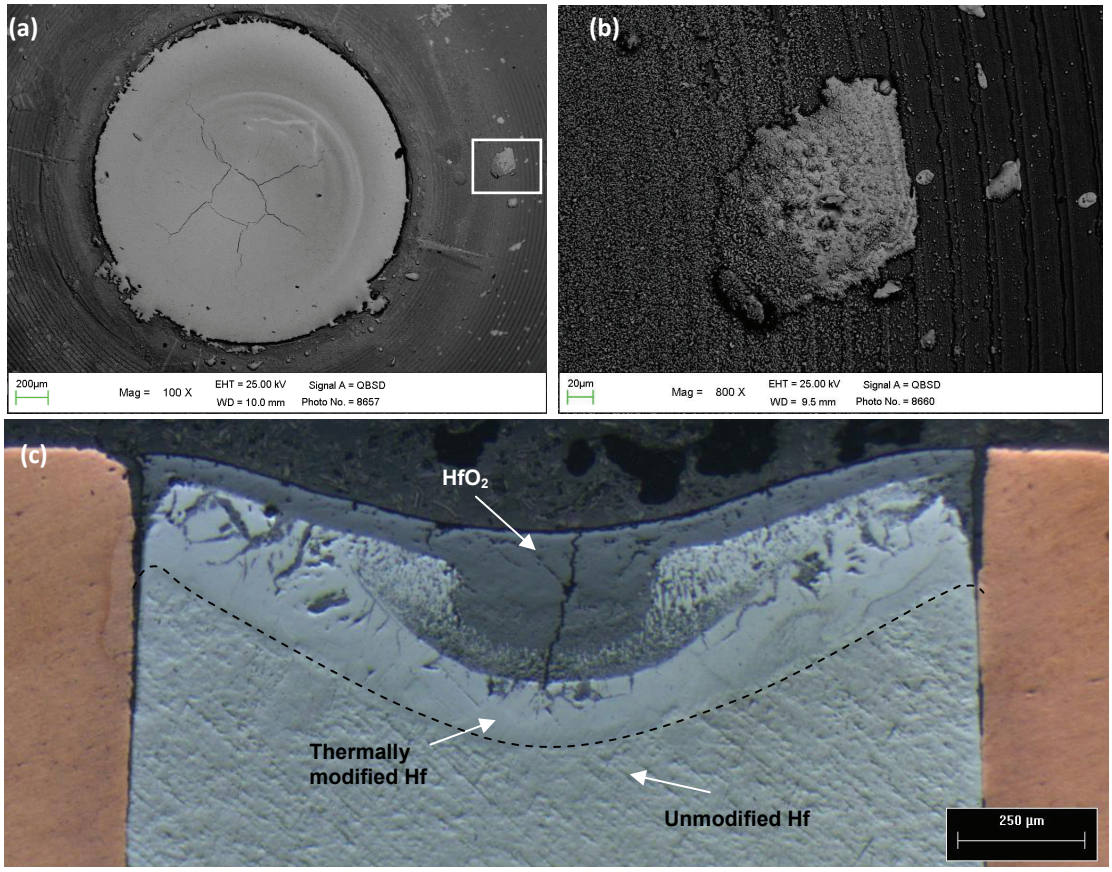

Fig. 2.21 Electrode after 5 *CCs*: (*a*) SEM top view, (*b*) detail of the emitted Hf-based products and (*c*) insert cross section (OM).

2.2.3.4 Electrode Cross Section Detailed Evolution

Fig. 2.22 reports the detailed evolution of electrodes cross section from 1 to 5 *CCs*. The increase of both the depth of the erosion cavity and the thickness of the oxide layer in the central part of the cavity, together with the oxide cracking, starts already at 2 *CCs*. Observing the oxide thickness and erosion cavity depth from 2 to 5 *CCs*, a clear trend cannot be found. When doing this analysis one should in fact consider the observed low repeatability of the process, due both to the complex phenomena involved in the PAC process inside the plasma chamber and to the process of formation of the concave recess [54]. Moreover, it is worth noticing that all the cross sections of Fig. 7 were taken from different electrodes, which underwent their own and unique erosion cycle. Nevertheless, observing the insert morphology from 1 to 13 *CCs*, the erosion cavities and oxide layer thickness tend to increase with the number of cuts.

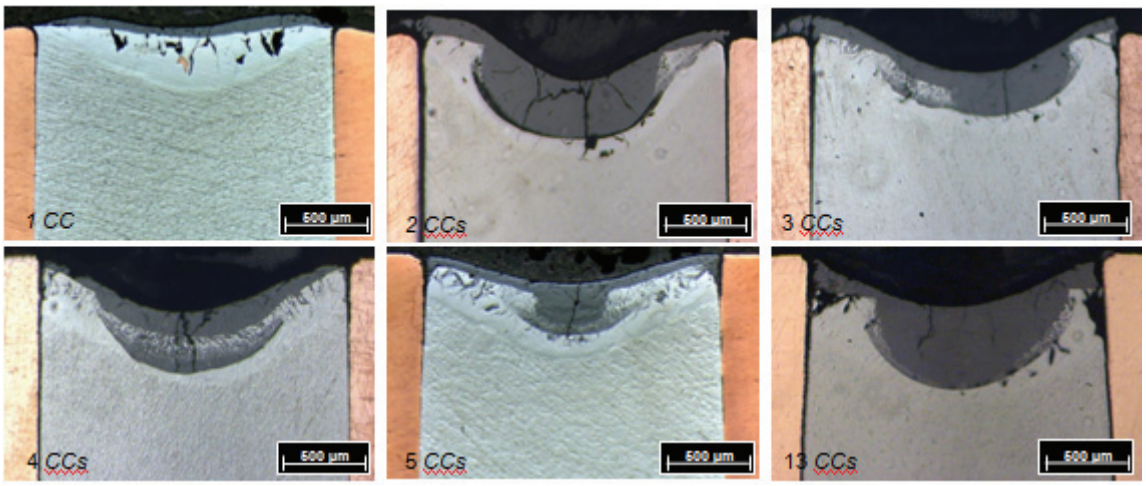

Fig. 2.22 Evolution of the electrodes cross section after 1 *CC*, 2 *CCs*, 3 *CCs*, 4 *CCs*, 5 *CCs* and 13 *CCs*.

At higher magnification, the electrode cross section after 5 *CCs* shows the presence of both macro cracking in the oxide layer and localised cracking in the zone of solid solution of Hf and O_2 (Fig. 2.23 *a*). The latter is the consequence of the oxygen dissolution as interstitial impurity in the Hf matrix, which increases Hf brittleness and causes, in turn, an increase of residual stresses as reported by Voitovich [58]. Moreover, these localized cracks might represent easy diffusion paths for oxygen, thus facilitating the oxide penetration in the Hf matrix, during the transient stages (when the top layers of the emitting material are not completely melted). Due to its brittleness, the thicker the

oxide layer, the more easily macroscopic cracks due to thermal cycling form, thus making the layer non-protective. A thicker oxide layer also implies a longer time needed for the arc to melt it, thus enhancing the ejection of solid oxide particles due to thermal shocks related to the arc attachment [2]. These phenomena could suggest the use of different current ramp depending on the erosion state of the electrode in order to minimize the subsequent erosion and increase the insert service life.

Fig. 2.23 *b* shows a particular of the oxidation paths entering the thermally modified zone, together with macroscopic and microscopic cracks.

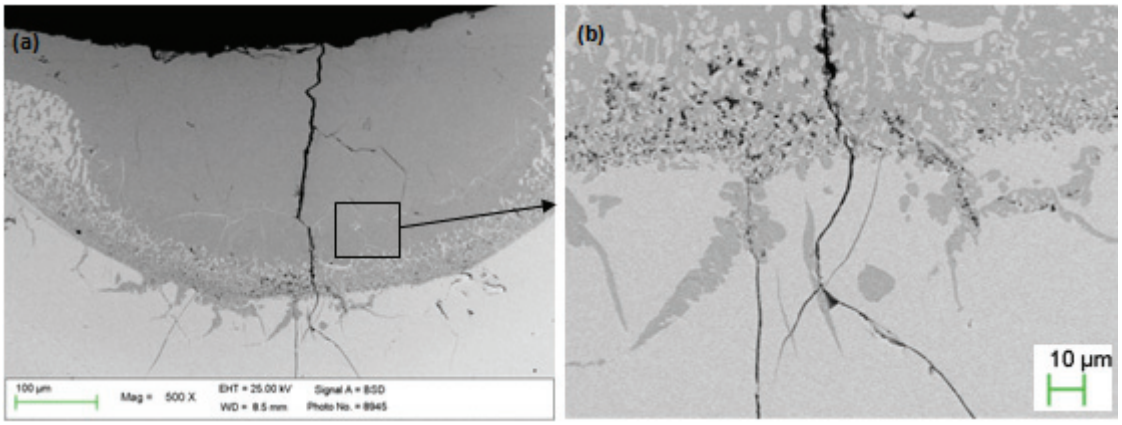

Fig. 2.23 (*a*) Oxide layer cracking after 5 *CCs* and (*b*) detail of the oxidation path penetrating the thermally modified Hf zone.

The chemically etched cross section of an insert after 13 *CCs* (Fig. 2.24) shows how the oxide layer consists of large HfO_2 grains (zone (a) in fig. 2.24 *a*). The thermally modified layer, i.e. metallic Hf with oxygen in solid solution (zone (b) in Fig. 2.24 *a*), is characterized by a thickness of about 200 µm in correspondence of the insert axis and comprises rounded grains whose average dimension is 105 µm. On the contrary, the unmodified Hf zone (zone (c) in fig. 2.24 *a*) is formed by fine equiaxic grains whose mean dimension was found to be around 15 µm, therefore much lower than in zone (b). As regards the thermally modified zone, the higher grain size, the presence of non-negligible amounts of oxygen (Table 1) in solid solution (above the solubility limit [56]) and the densification observed in optical images of the cross sections (Fig. 2.18 *c*, 2.21, 2.22 and 2.24 *a)*, let us hypothesize that this layer underwent melting during the cutting phase, thus suggesting that the temperature achieved in this zone was higher than the melting point of Hf.

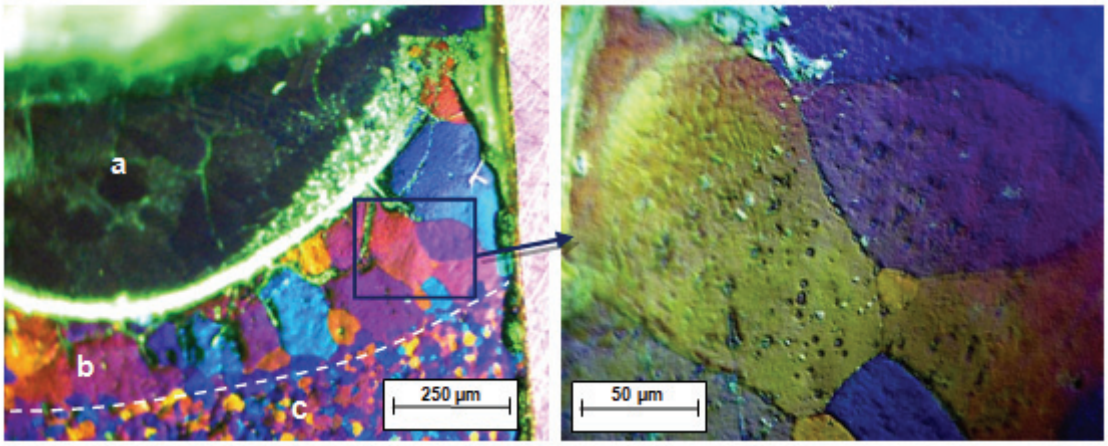

Fig. 2.24 Chemically etched insert cross section (OM) of the Hf insert after 13 *CCs*, observed with OM under polarized light with indication of three different zones: (*a*) HfO_2 layer, (*b*) thermally modified Hf and (*c*) unmodified Hf; on the right-hand side, a higher magnification detail of the microstructure in the thermally modified zone.

Grain size of the Cu holder near the Hf insert was found to be ranging from 40 to 65 µm (Fig. 2.25), without being affected by thermal cycling at low number of *CCs*. It is possible that a small amount of material achieves conditions for recrystallization, but due to the high thermal conductivity of Cu this area is very limited. Grains are slightly elongated in a direction parallel to the insert axis due to the plastic deformation they underwent during the production process.

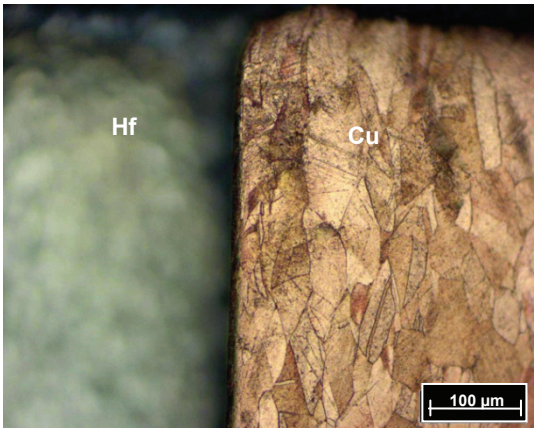

Fig. 2.25 Chemically etched cross section (OM) of the Cu holder near the insert interface.

Fine microstructural analysis of the Hf insert could give another estimation of temperatures achieved during the process in specific areas of the insert cross section. For instance, Fig. 2.26 how the presence of striated precipitates of α-Hf , at the interface

between the HfO_2 and molten Hf layers, resulting from the cooling of cubic HfO_2 from temperatures ranging between 2200° and 2150°C, due the steep solubility change related to transformation of cubic HfO_2 to tetragonal HfO_2 [59]. On the contrary, if cooling starts from temperatures below 2100°C, no cubic-tetragonal inversion occurs and no striations are detected, according to [59].

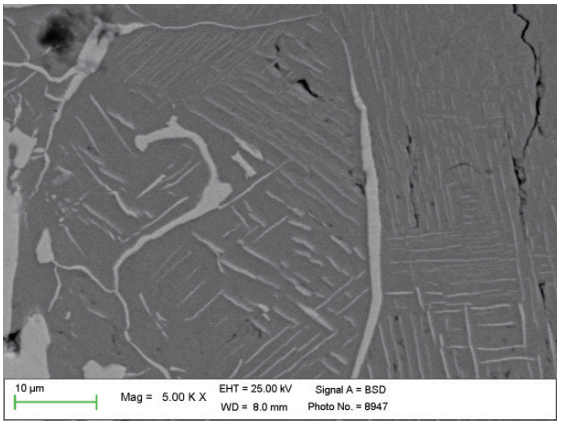

Fig. 2.26 Striated precipitates of α-Hf in a HfO_2 matrix.

At the interface between the Hf insert and the Cu holder two kinds of situation can develop: the detachment of the two components with subsequent oxide penetration (Fig. 2.27 *a*) or the formation of Cu/Hf/O compounds (Fig 2.27 *b*). Both configurations cause a worsening of the heat removal process from the insert, badly affecting the electrode performance.

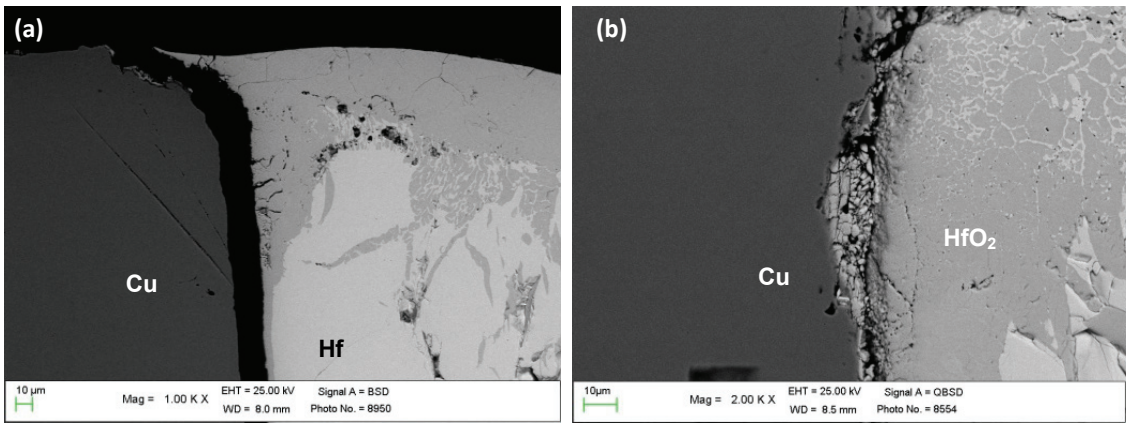

Fig. 2.27 (*a*) Cu holder-Hf insert detachment and (*b*) formation of Cu/Hf/O compounds at the interface between the insert and the electrode body.

As observed in Fig. 2.17 *c*, the contact between Hf and Cu is not continuous even in the as-supplied electrode. As for the erosion cavity and oxide layer depth, the phenomena involved in the detachment are only partially repeatable; moreover, the entity of the separation between the insert and the Cu holder is not axial-symmetric. Nevertheless, the interface detachment depth tends to increase with the number of *CCs*, as it measured about 0.8, 1.0 and 1.3 mm depth respectively after 1, 5 and 13 *CCs*.

2.2.4 CONCLUSIONS

The microstructural modifications occurring in hafnium (Hf) cathodes during first plasma arc cutting cycles, operating at high current level in oxidizing atmosphere, were experimentally investigated. The microstructural phenomena involved in the erosion process were interpreted by means of thermodynamics and kinetics of the Hf high temperature oxidation.

Microstructural analysis, including Raman spectroscopy, optical and electron scanning microscopy on the electrodes surface and cross section, allowed the identification of three typical zones after cutting:

- monoclinic HfO_2 layer;
- remelted transition zone with O_2-Hf solid solution;
- unmodified Hf.

After cutting, the oxide layer undergoes macrocracking, while the remelted Hf shows both a remarkable grain growth and the presence of microcracks which act as preferential oxidation paths during transient stages. The analysis of Hf precipitates in the oxide layer allowed to estimate that temperatures achieved during the process were above 2100 °C in this zone.

The study of the deposited HfO_2 morphologies confirmed that massive emissive material ejections occur both during the arc-on and arc-off transient phases. The erosion cavity deepens with increasing cutting cycles, also as a consequence of convective forces due to the Marangoni effect.

Detachment was detected at the Hf/Cu interfaces, worsening the heat dissipation and accelerating oxidation and erosion phenomena.

Finally, the oxide layer thickness was found to increase with the number of cutting cycles, thus, in order to improve the insert service life, it is suggested the use of different current ramp at subsequent erosion stages, to avoid thermal shocks which would break the brittle oxide layer.

CHAPTER 3

PROTOTYPAL Hf-Ag AND Zr-Cu COMPOSITE INSERT ELECTRODE FOR PAC TORCHES

ABSTRACT

Traditional cylindrical insert design for plasma arc cutting electrodes presents specific limits, especially when operating in oxidizing atmospheres, as discussed in the previous chapters. The work presented in this chapter was aimed at producing, characterizing and testing prototypes of composite inserts, combining powders of a high thermal conductibility (Cu, Ag) and high thermionic emissivity (Hf, Zr) materials, aimed at improving the electrode endurance performances.

First, the microstructural characterization of Hf-Ag and Zr-Cu inserts, realized by means of different production routes, is discussed. In particular, composite pellets were produced both by means of traditional sintering and a rapid sintering technique.

In the last section, explorative wear tests on three manufactured prototypal composite inserts are described, together with microstructural and morphological characterization of the prototypal electrodes at different stages of their service life.

3.1 INTRODUCTION

When operating in oxidizing atmospheres, the size of the emitting surface of traditional cylindrical inserts is generally increased for higher current capacity operations. The high thermionic emissivity insert (Hf, Zr), however, has a poor thermal conductivity with respect to the electrode body. Thus, removal of heat from the centre of the insert to the surrounding electrode body is hindered. This results in the development of higher temperatures at the electrode tip, which in turn increase the insert

oxidation rate and finally cause faster erosion and lower service life.

The use of composite insert, combining a high thermal conductivity material (Cu, Ag) and a high thermionic emissivity material to overcome the limits of the traditional insert design, were described in *US pat. 6,130,399* [40] and *EP 1099360* [41] (see also Paragraph 1.3.2). In particular, in one specific embodiment of these patents, the use of a mixture of powders to produce such kind of inserts is described.

The effectiveness of a high conduction/high emission composite insert have not yet been proved by means of scientific publication, and no experiments have been found in literature concerning the composition and possible manufacturing methods for these emissive elements. Moreover, although the high potential of such designed inserts, no commercial electrodes adopting this kind of solution are nowadays available.

The work presented in this chapters was aimed at producing, characterizing and testing prototypes of composite inserts, combining powders of a high thermal conductibility (Cu, Ag) and high thermionic emissivity (Hf, Zr) materials, with the general objective of supplying preliminary assessment of the potential of such inserts to improve electrode service life for PAC torches.

3.2 INSERT PRODUCTION AND CHARACTERIZATION

3.2.1 EXPERIMENTAL PROCEDURE

Composite pellets were produces by means of sintering techniques starting from two powder systems: Cu-Zr and Ag-Hf. Powders were first blended by means of 6 hours ball milling. A conventional sintering method was used in first instance, involving two production steps. First, the powders were cold pressed in carbide tooling, obtaining a so called *moulded* pellet. Then, sintering was performed in a vacuum atmosphere, at 885°C for 2 hours in the case of Cu-Zr system, and at 900° C for 30 minutes for the Ag-Hf system. For the Cu-Zr system, three different composition (wt.%) were used: Cu70-Zr30, Cu50-Zr50 e Cu29-Zr69-$La_2O_3$2 (also referred to as Cu29-Zr69 in the text); for the Ag-Hf system, only the 50-50 wt. % powder mixture was used. Pellets were supplied with a diameter of 2,80 mm and length of 5,30 mm (Fig.s 3.1, 3.2).

A *rapid sintering* method was also used to produce small disks starting from Cu50-Zr50 and Ag50-Hf50 powder mixtures. The sintered disks were characterized by a diameter of 20 mm and a thickness of 2 mm (Fig. 3.3).

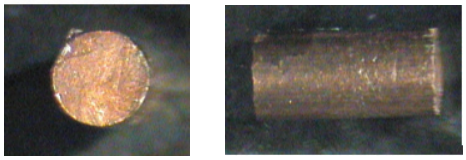

Fig. 3.1 Top and lateral view of a sintered Cu50-Zr50 insert.

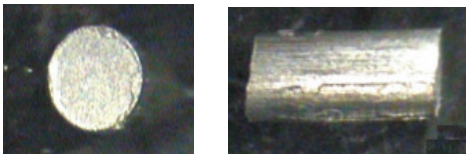

Fig. 3.2 Top and lateral view of a sintered Ag50-Hf50 insert.

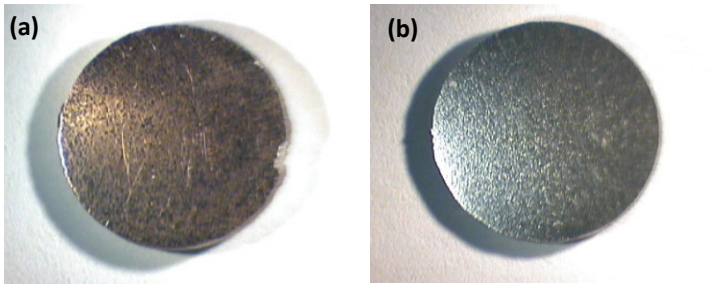

Fig. 3.3 Rapid sintered disks: (*a*) Hf50-Ag50 (*b*) Cu50-Zr50.

Powder mixture samples were first subjected to microstructural analyses by means of Scanning Electron Microscopy (SEM) and Optical Microscopy (OM). The elemental analysis was performed by energy dispersive spectroscopy (EDS), whilst phase composition was analysed by X-Rays Diffraction by comparison with the ICDD-PDF database [60].

The external surface of those pellets which were produced by means of conventional sintering, both in the moulded and sintered state, underwent the same characterization route as powders did. In order to characterize the pellets cross sections, they were mounted in epoxy resin and polished through grit paper sheets (up to 2000P), while mirror polishing was obtained by means of 3 μm and 1 μm diamond suspensions. The insert cross section were also subjected to OM and SEM investigation and XRD analyses. EDS was used either at large scale, to investigate composition homogeneity, and at smaller scale, to investigate the presence of interaction phased at the interface

between the two material constituting the inserts. Similar investigation route was followed to analyse the disks produced by means of *rapid sintering*.

3.2.2 EXPERIMENTAL RESULTS

3.2.2.1 POWDER CHARACTERIZATION

Cu-Zr system

Powders were supplied with a nominal granulometry of 270 mesh for Cu and Zr, and of 325 mesh for La_2O_3. SEM micrographs of Fig. 3.4 show sharply particles with dimensions ranging from a few microns to about 100 µm, with the presence of angular elements. The detected composition was slightly different from the nominal one, possibly due to inhomogeneous blending, and in the Cu50-Zr50 and Cu29-Zr69-$La_2O_3$2 systems presence of oxides was found. The XRD spectrum confirmed that oxides are present in these two systems, but the oxidation involves only the copper phase (Cu_2O) in the former, while it also involves the Zr phase (ZrO_2) in the latest, further than the LaO_2 oxides introduced as lubricant (Fig. 3.5).

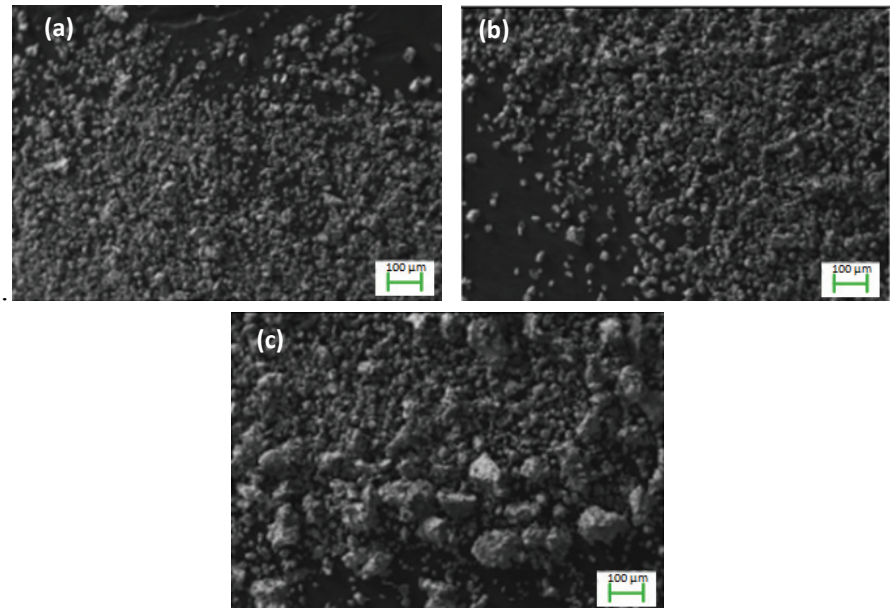

Fig. 3.4 SEM micrographs of Cu-Zr powders: (*a*) Cu70-Zr30, (*b*) Cu-50Zr-50, (*c*) Cu69-Zr29

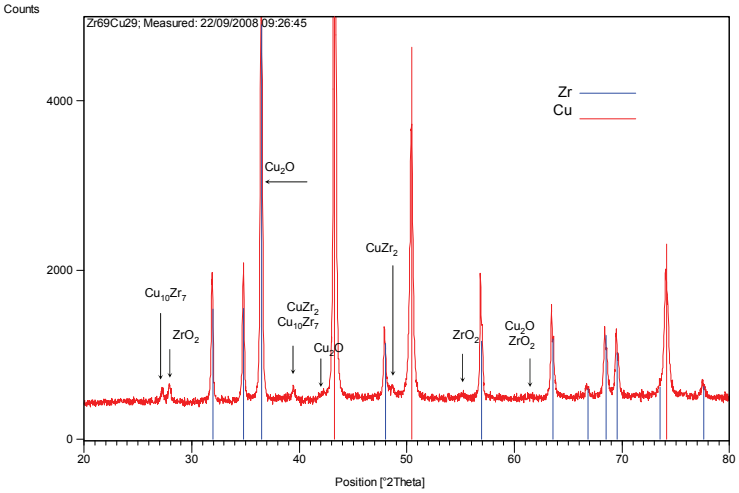

Fig. 3.5 XRD spectrum of the Cu29-Zr69-La_2O_32 powder system.

Ag-Hf system

Starting powders were supplied with a nominal granulometry of 325 mesh for Hf and Ag. SEM micrographs of Fig. 3.6 show angular particles, whose size ranges from a few microns to more than 100 µm.

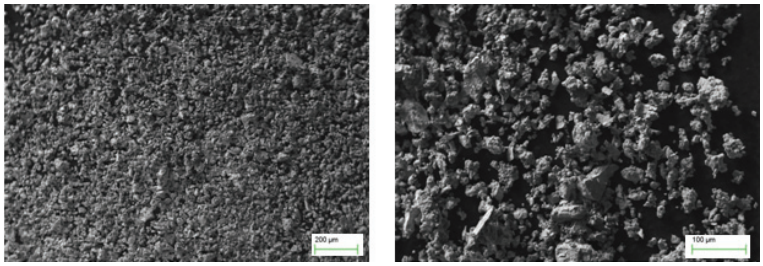

Fig. 3.6 SEM micrographs of Ag-Hf powders.

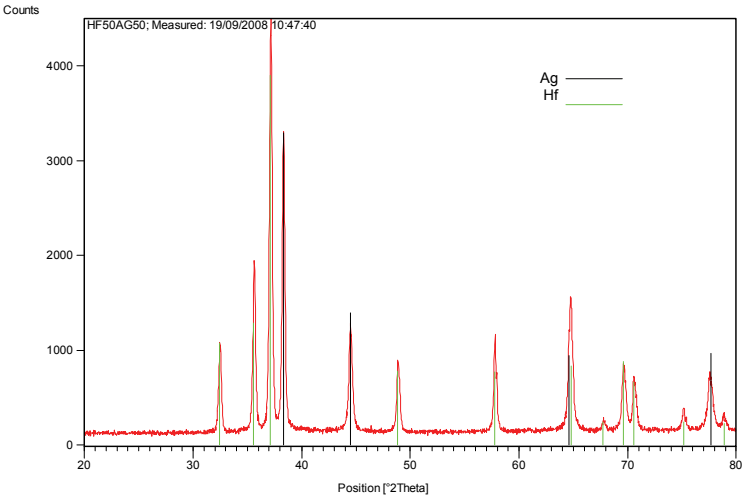

Fig. 3.7 XRD spectrum of the Ag50-Hf50 powder system.

In this case, the XRD analyses detected only the Hf and the Ag phases, thus excluding powder oxidation, and EDS showed that the mixture composition was close to the nominal one.

3.2.2.2 Insert Characterization after Moulding Stage

Cu-Zr system

EDS spectra of Table 3.1 indicates a partial oxidation of the insert surface, which was not detected with XRD (Fig. 3.8), where only metallic Cu and Zr phase were identified. Metallographic analyses of the pellet cross section (Fig. 3.9) shown the presence of porosity and low cohesion between the two phases, particularly in the case of the Cu50-Zr50 system. Particle distribution was found to be inhomogeneous, but without a preferential orientation.

The lack of homogeneity in composition was confirmed by EDS analyses, which, in Table 3.2, highlights the differences with nominal composition. Further SEM and EDS analyses, performed locally at the interface between Cu and Zr, did not reveal any relevant presence of interaction phases.

%wt	Cu70-Zr30	Cu50-Zr50	Cu29-Zr69-La2O32
Cu	83	66	35
Zr	4	25	51
O	13	9	13
La	-	-	1

Table 3.1 EDS based composition of the Cu-Zr moulded inserts surface.

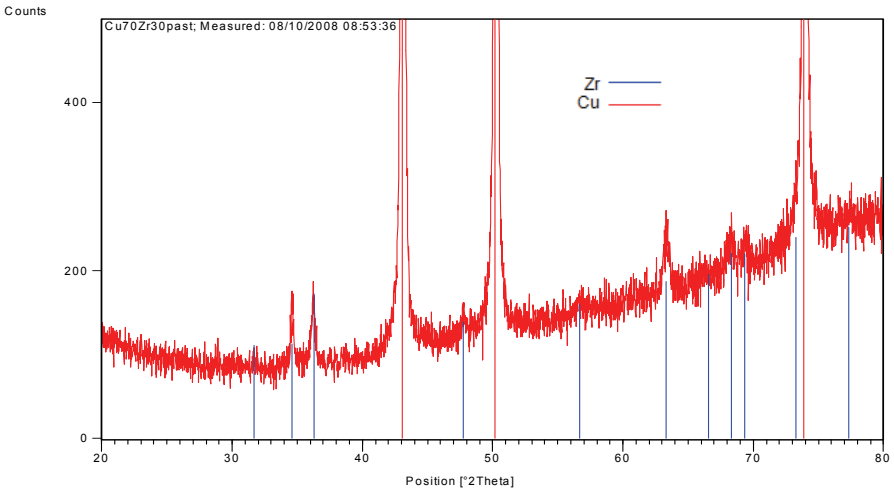

Fig. 3.8 XRD spectrum of Cu29-Zr69-$La_2O_3$2 moulded insert surface.

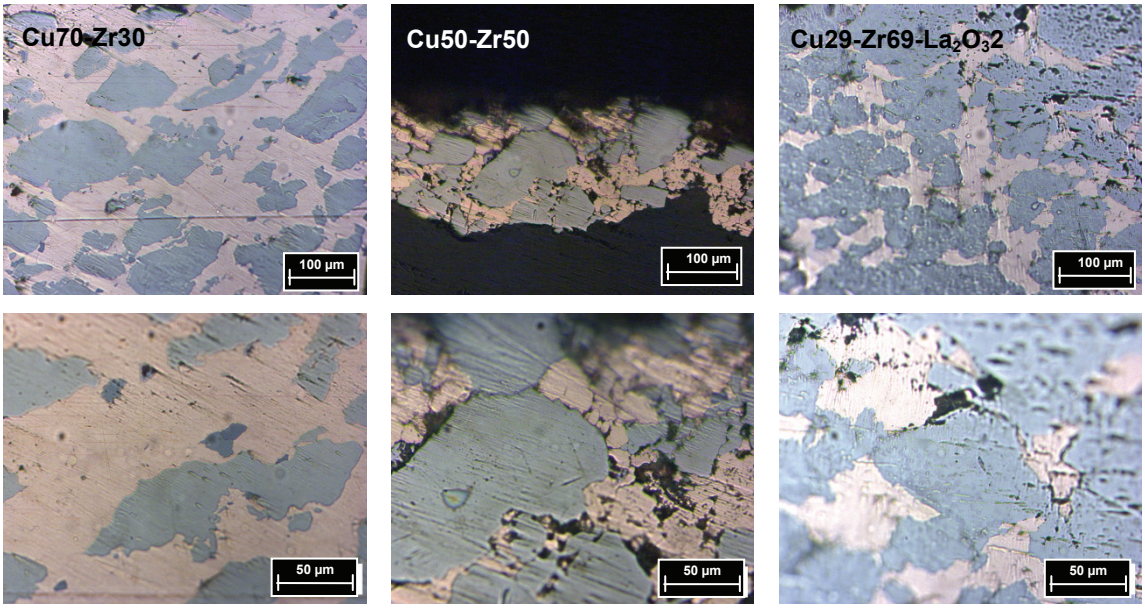

Fig. 3.9 Cross sections of Cu-Zr moulded inserts.

%wt	Cu70-Zr30	Cu50-Zr50	Cu29-Zr69-La2O32
Cu	51	37	19
Zr	46	51	72
O	3	12	8
La	-	-	1

Table 3.2 EDS based composition of the Cu-Zr moulded inserts.

Ag-Hf System

EDS analyses on the insert surface (Table 3.3) identified the presence of oxygen further than Ag and Hf, whereas no oxides were identified in by means XRD (Fig. 3.10), since the material layer involved in the measure is thicker than with EDS.

High degree of porosity and low cohesion was found by observing the pellet cross section (Fig. 3.11). the insert microstructure appeared to be formed by a silver matrix with a disperse Hf second phase. Once again, particle distribution was found to be inhomogeneous, although without a preferential orientation, as also suggested by the differences between the nominal and EDS-detected composition.

%wt	Surface	Cross sec.
Ag	53	58
Hf	34	42
O	13	-

Table 3.3 EDS based composition of the Ag-Hf moulded insert.

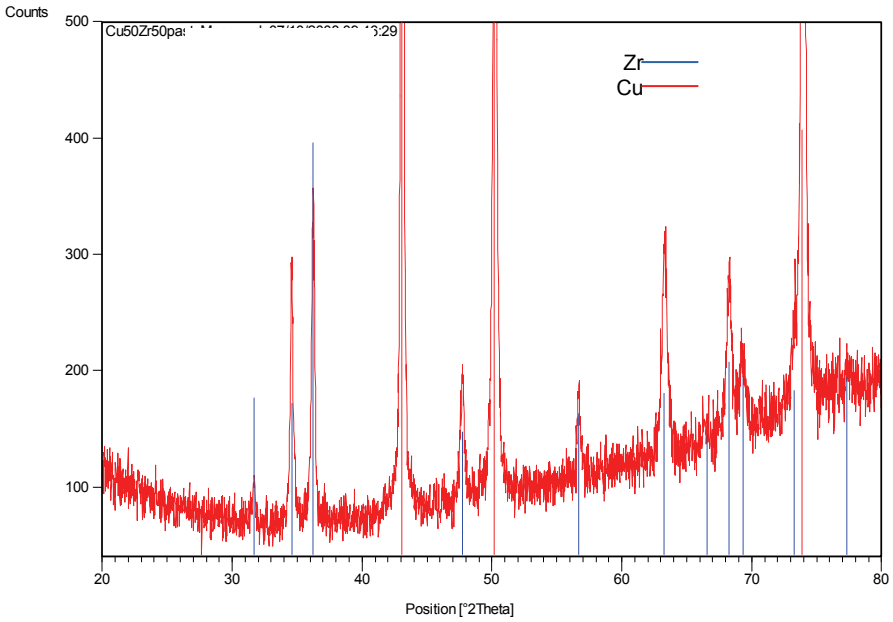

Fig. 3.10 XRD spectrum of the Ag-Hf moulded insert surface.

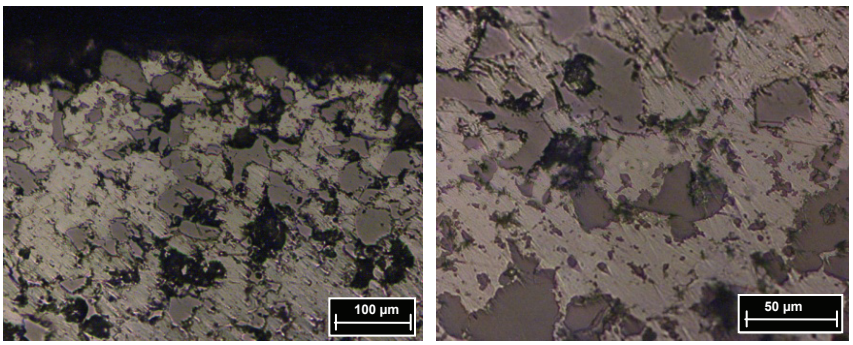

Fig. 3.11 Cross section of the Ag-Hf moulded insert.

3.2.2.3 INSERT CHARACTERIZATION AFTER SINTERING

Cu-Zr System

Sintered inserts showed an irregular surface morphology and were found to be generally more oxidized than the moulded ones, as shown in the EDS analysis of Table 3.4 and XRD spectrum of Fig. 3.13. It emerged that, during sintering, a ZrO_2 surface layer, not detectable with XRD after moulding, was created. Metallographic analyses revealed porosity and no preferential distribution of phases; differently from moulded insert, crown of Cu-Zr interaction were identified at the matrix/dispersoids interface.

SEM micrographs and EDS analyses, taken in cross section at large scale (Fig. 3.15 and Table 3.6), shown once again a inhomogeneous microstructure and, consequently, divergences between measured and nominal composition.

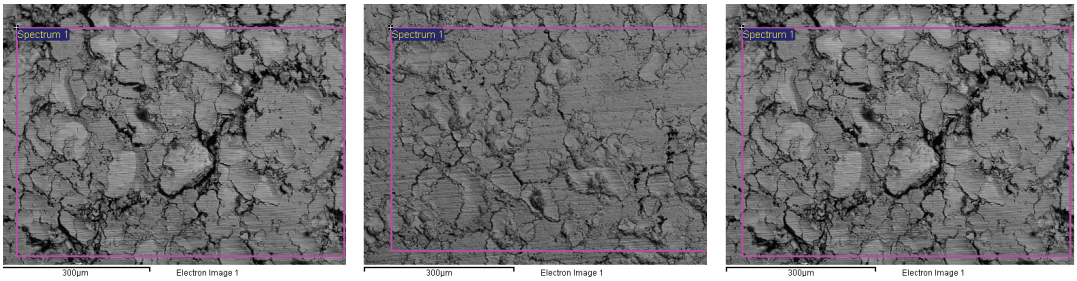

Fig. 3.12 Cu29-Zr69-La_2O_3 sintered insert surface and EDS field.

%wt	Cu70-Zr30	Cu50-Zr50	Cu29-Zr69-$La_2O_3$2
Cu	60	40	29
Zr	30	46	51
O	10	14	17
La	-	-	3

Table 3.4 EDS based composition of the Cu-Zr sintered inserts surface.

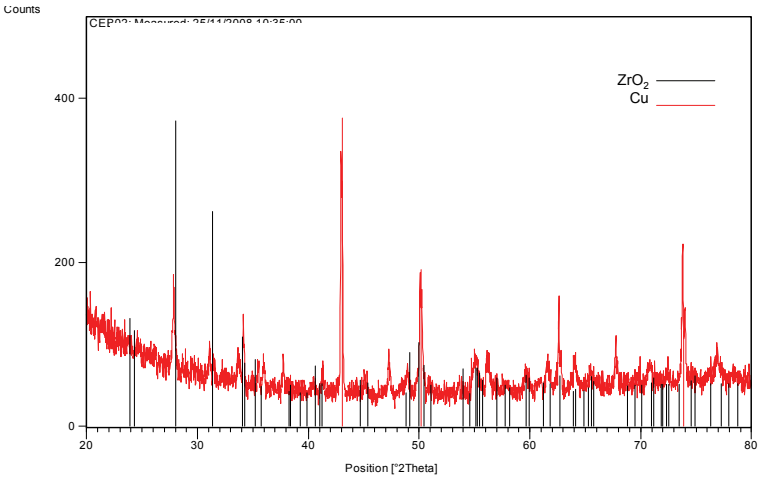

Fig. 3.13 Cu29-Zr69-La_2O_3 sintered insert XRD spectrum.

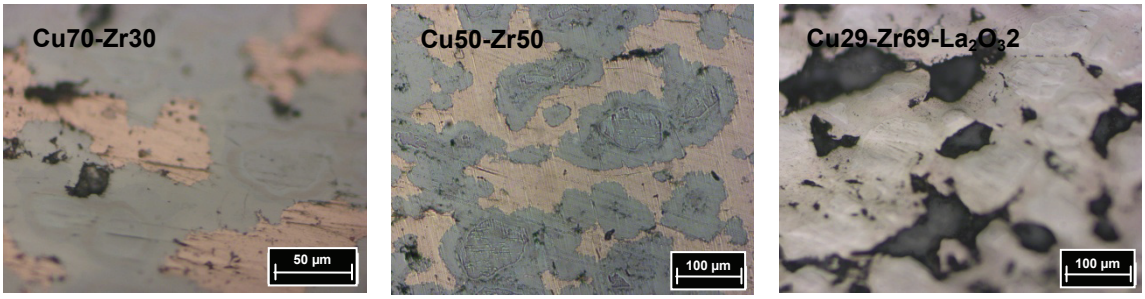

Fig. 3.14 Cu-Zr sintered inserts cross section.

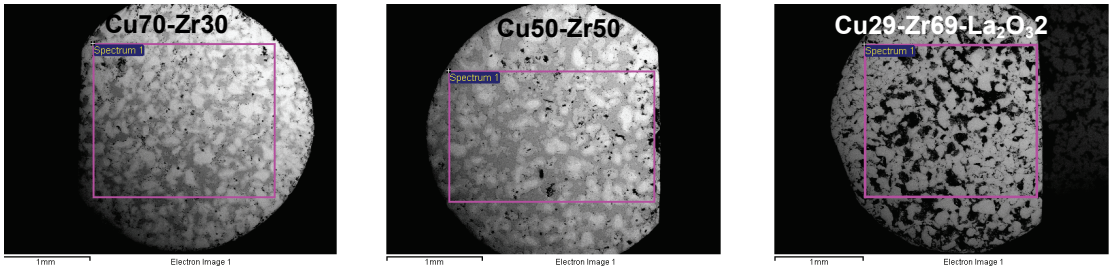

Fig. 3.15 Cu-Zr sintered inserts cross section and respective EDS fields.

%wt	Cu70-Zr30	Cu50-Zr50	Cu29-Zr69-$La_2O_3$2
Cu	41	64	20
Zr	53	33	64
O	6	3	15
La	-	-	1

Table 3.5 EDS based composition of the Cu-Zr sintered inserts..

Ag-Hf System

The Ag50-Hf50 sintered insert showed a surface morphology which is irregular and porous (Fig. 3.16); based on EDS analyses, it resulted more oxidised that the moulded specimen. XRD analyses confirmed the presence of HfO_2 (Fig. 3.17).

Insert cross section were characterized by porosity and lack of directionality in phase orientation (Fig. 3.18). EDS analyses showed once again low correspondence with nominal composition (Table 3.6). The specimen is now characterized by relevant oxidation not only in surface, but also in the bulk material.

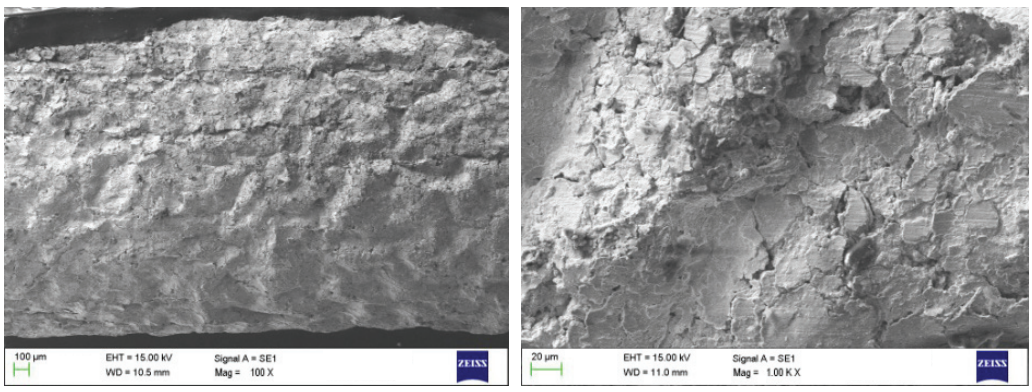

Fig. 3.16 Ag-Hf sintered insert surface.

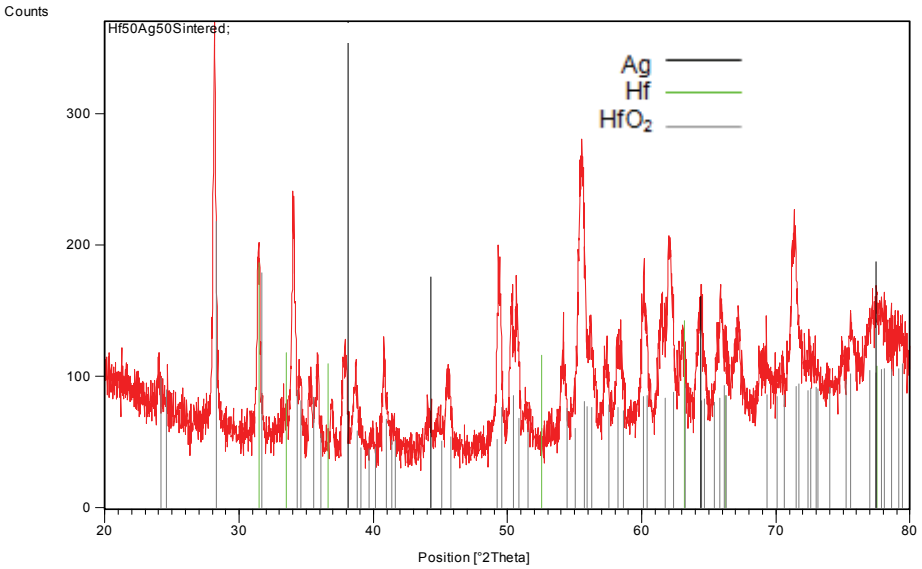

Fig. 3.17 XRD spectrum of the Ag-Hf sintered insert surface.

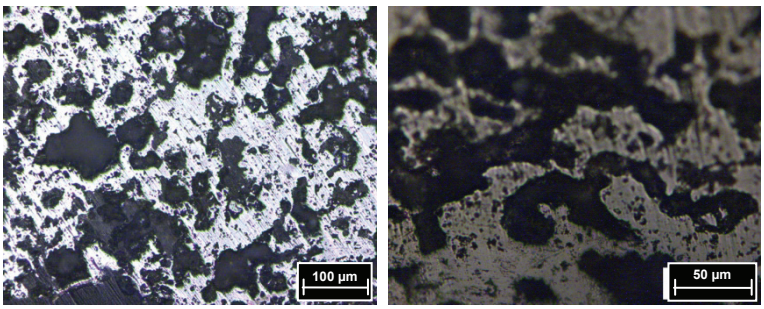

Fig. 3.18 Cross section of the Ag-Hf sintered insert.

%wt	Surface	Cross sec.
Ag	11	31
Hf	71	50
O	18	19

Table 3.6 EDS based composition of the Ag-Hf sintered insert.

3.2.2.4 Rapid Sintered Inserts

Cu70-Zr30

The XRD spectrum of Fig. 3.19 highlighted that the main phases present in the insert are Cu and Zr in their metallic state. Although in limited amount, other Cu-Zr interaction phases are present, attributable to the $Cu_{51}Zr_{14}$ intermetallic.

Metallographic investigation showed a good cohesion between Cu matrix and Zr-rich zones, and almost no porosity was detected (Fig. 3.21, 3.22). Moreover, interdiffusion zones were found to be significantly thinner than the ones observed in the sintered pellet of same nominal composition. Once again, general composition is not coherent with the nominal one, and 5% of oxygen was found (Fig. 3.22). However, the microstructure appears much more uniform with respect to the conventional sintering. Local EDS analyses highlighted the non-negligible presence of oxygen in the interdiffusion zones.

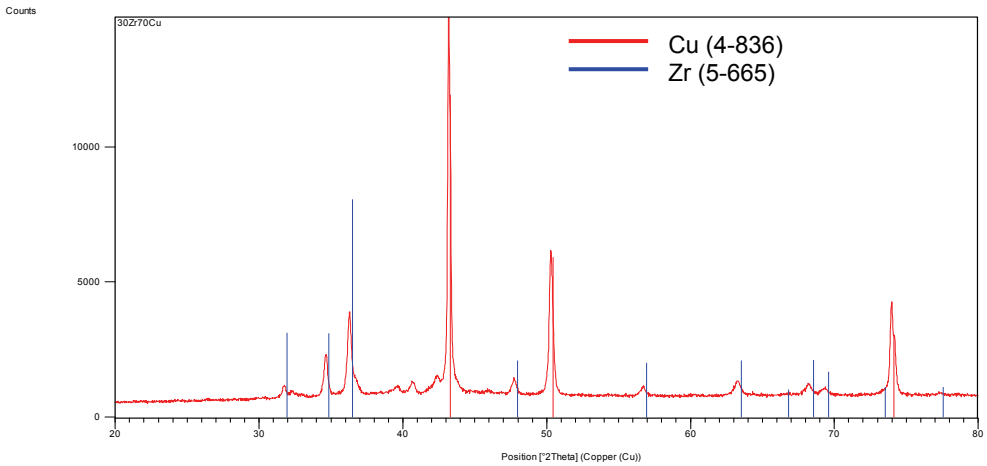

Fig. 3.19 XRD spectrum: rapid sintered Cu70-Zr30.

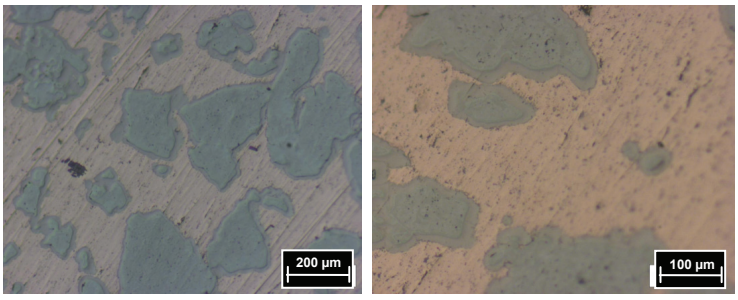

Fig. 3.21. Metallographic cross sections of rapid sintered Cu70-Zr30.

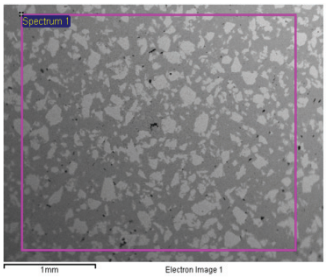

%wt	Cu70-Zr30
Cu	55
Zr	40
O	5

Fig. 3.22 EDS field and elemental analysis of rapid sintered Cu70-Zr30.

Cu50-Zr50

The XRD spectrum of Fig. 3.23 shows that main phases are Cu and Zr in the metallic state, with presence of the intermetallic $Cu_{51}Zr_{14}$, although in limited amount.

As observed for the previous specimen (Cu70-Zr30), good cohesion and absence of porosity was found by means of metallographic analyses (Fig. 3.24). Interdiffusion zones, surrounding Zr-based particles, are again thinner than in the case of sintered component of same nominal composition. Large-scale EDS analysis showed a composition which is now comparable with the nominal one, although a 6% difference remains (Fig. 3.25). Local scale EDS revealed the presence of oxygen in the interdiffusion zones (Fig. 3.26), even though it was not revealed in the large scale measurements.

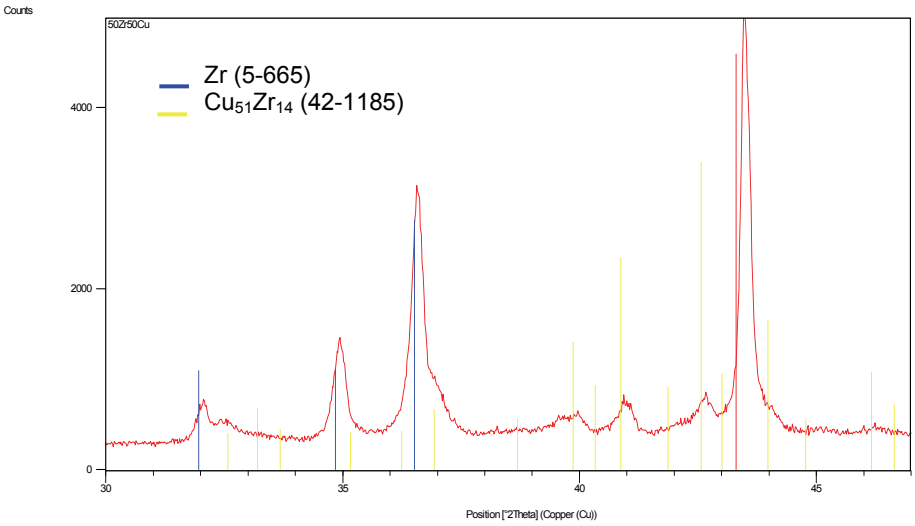

Fig. 3.23 XRD spectrum 30°-47° detail of rapid sintered Cu50-Zr50.

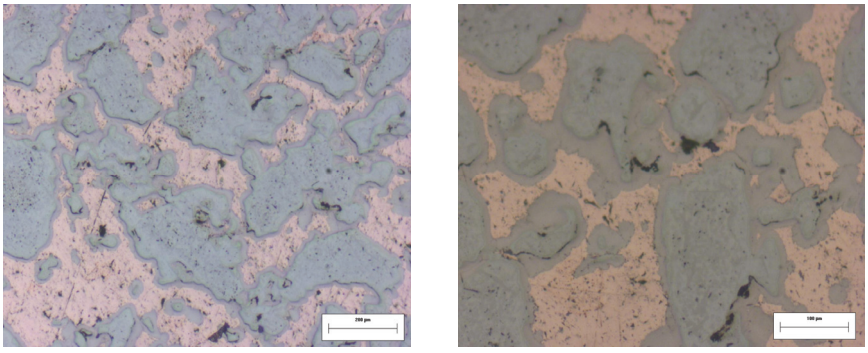

Fig. 3.24 Metallographic cross sections of rapid sintered Cu50-Zr50.

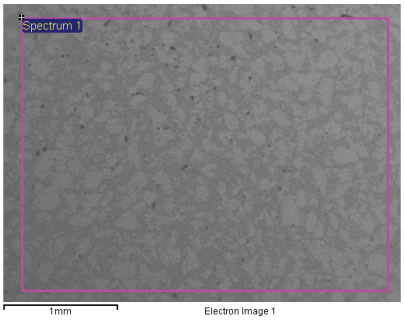

%wt	Cu50-Zr50
Cu	46
Zr	54

Fig. 3.25 Large scale EDS field and elemental analysis of rapid sintered Cu50-Zr50.

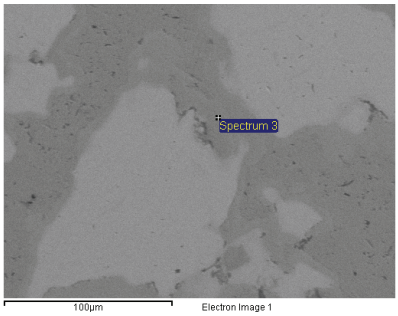

%wt	Average
Cu	65
Zr	27
O	8

Fig. 3.26 Local EDS of Zr-Cu inter-diffusion zones.

Cu29-Zr69-$La_2O_3$2

Main phases in the XRD spectrum were found to be metallic Cu and Zr, although traces of the intermetallic $Cu_{51}Zr_{14}$ were detected (Fig. 3.27). A compact microstructure was observed by means of metallographic analyses, formed by a Zr matrix in which Cu-based particles are dispersed, although small porosities were found. Zr-Cu interaction zones are evident but thinner with respect to the corresponding conventionally sintered pellet (Fig. 3.30).

Large scale EDS showed a limited difference with the nominal composition; in particular, the amount of copper is 7% lower than nominal, whilst 7 % of oxygen was detected (*Fig. 3.29*). Localized EDS revealed in particular that oxygen is present in small amount (about 2 %) in the Zr-based and Cu-based zones, while it exceeds 7% in the interaction zones, were the above mentioned intermetallic compound is present (Fig. 3.30).

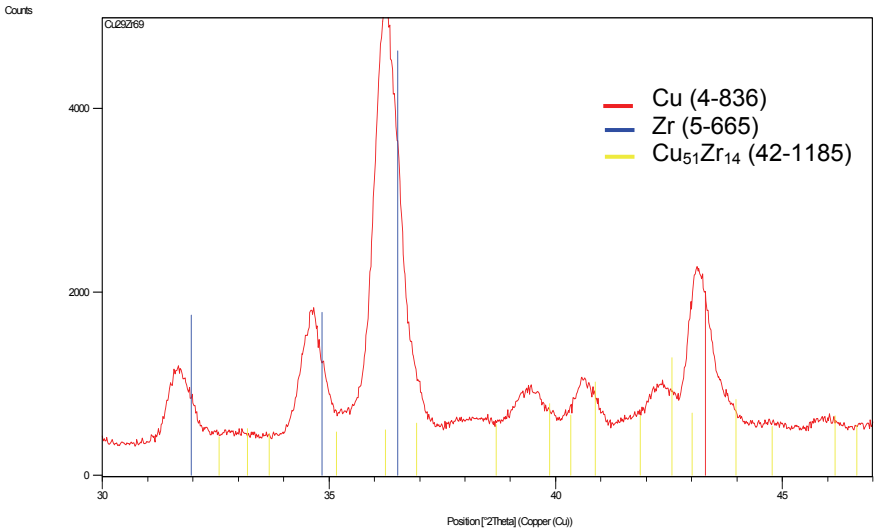

Fig. 3.27 Detail 30°-47° of XRD spectrum of rapid sintered 29-Zr69-$La_2O_3$2.

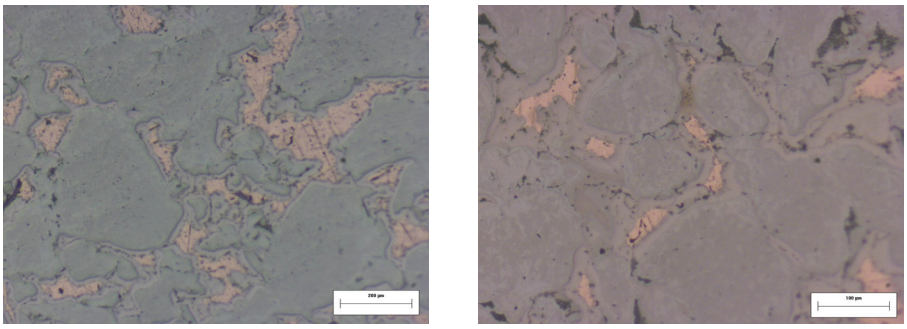

Fig. 3.28. Metallographic cross sections of rapid sintered 29-Zr69-$La_2O_3$2.

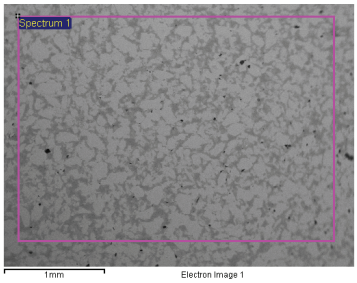

%wt	Cu29-Zr69-La_2O_3
Cu	22
Zr	70
O	7
La	1

Fig. 3.29 Large scale EDS field and elemental analysis of rapid sintered 29-Zr69-$La_2O_3$2

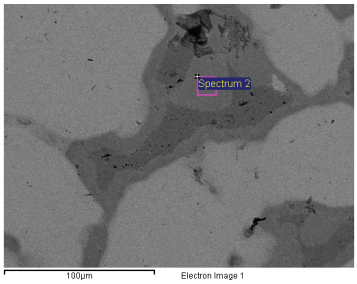

%wt	Average
Cu	62
Zr	31
O	7
La	0

Fig. 3.30 Local EDS analysis of Zr-Cu inter-diffusion zones.

Ag50-Hf50

In the Ag-Hf rapid sintered disk, principal phases were found to be the two constituent in the metallic form. The XRD spectrum highlighted the presence of other compounds which are not Ag or Hf oxides. Since no spectrum peak reference are available in the ICDD-PDF database for possible Hf-Ag o Hf-Ag-O, these compounds could not be identified.

Good cohesion was found between the two phases, in a uniform microstructure without preferential orientation (Fig. 3.32) and characterized by the presence of interdiffusion zones of limited extension. Good correspondence was found between nominal composition and EDS large scale analyses (Fig. 3.33), although with a significant amount of oxygen (4 %). At a smaller scale, EDS revealed that oxygen was present mainly in the Hf rich areas and in the interaction zones (Fig. 3.34).

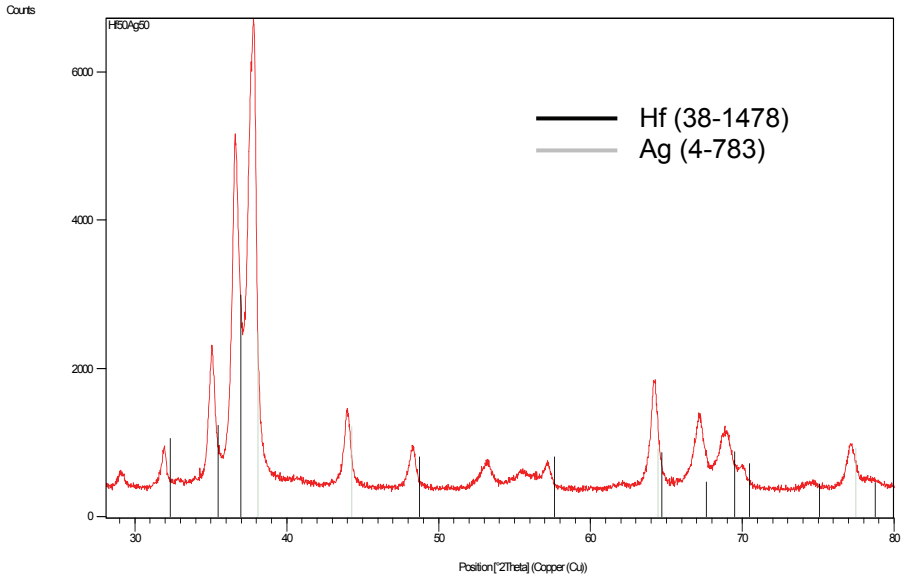

Fig. 3.31 XRD spectrum of rapid sintered Ag50-Hf50.

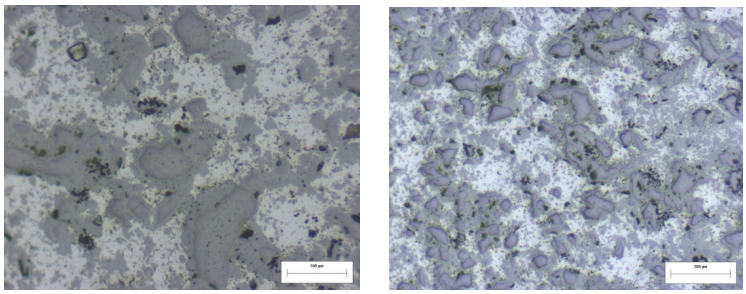

Fig. 3.32 . Cross sections of rapid sintered Ag50-Hf50.

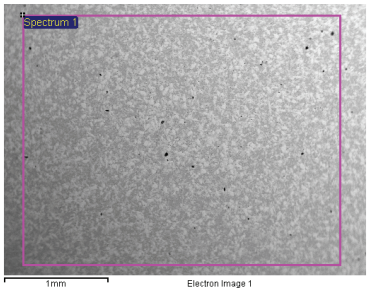

%wt	Ag50-Hf50
Ag	48
Hf	48
O	4

Fig. 3.33 Large scale EDS field and elemental analysis of rapid sintered Ag50-Hf50

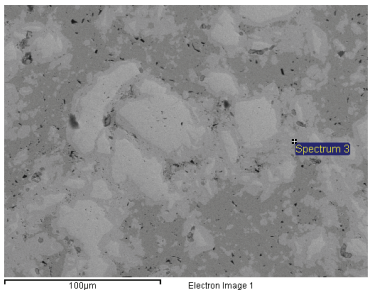

%wt	Average
Ag	43.77
Hf	53.56
O	2.67

Fig. 3.34 Local EDS analysis of Hf-Ag inter-diffusion zones.

3.2.3 DISCUSSION

The analyses accomplished on the inserts obtained by means of traditional sintering showed that, both for the semi finished (mechanically compacted) products, named *moulded,* and finished products, named *sintered*, there was a low correspondence between the actual and nominal chemical composition, possibly related to factors such as: limited effectiveness of the starting powders blending, low cohesion between phases, high degree of porosity and relevant presence of oxidation phenomena. The microstructure was found to be constituted by areas rich in Zr (or Hf) dispersed in a Cu (or Ag) phase. The cross section of sintered pellets was characterized by the presence of interaction zones of interdiffused material around Zr-(Hf-) rich areas, in which a relevant amount of oxygen is detected. Traces of the intermetallic $Cu_{51}Zr_{14}$ were detected in the interaction zones for the Cu-Zr specimens, while it was not possible to identify the intermetallic present in the Ag-Hf disks. Moreover, oxidation products were found on the external pellet surface, possibly due to the interaction with the sintering atmosphere. This oxidation could be due to a non sufficient vacuum degree, and/or to the oxygen which was trapped between particles during the moulding phase, not performed under vacuum nor inert atmosphere.

Since sintered products are more oxidized than moulded ones, it is expected that their density is lower with respect to the nominal one, as actually found after density measurements (Table 3.14, 3.15).

		Measured density [g/cm^3]	Nominal density* [g/cm^3]	%
Cu70-Zr30	Moulded	7,22	8,20	88,0
	Sintered	6,30[a]		76,8[a]
	Rapid sint.	7,85		95,8
Cu50-Zr50	Moulded	6,59	7,72	85,4
	Sintered	5,92		76,7
	Rapid sint.	7,20		93,3
Cu29-Zr69	Moulded	6,31	7,20	87,6
	Sintered	5,10		70,9
	Rapid sint.	6,98		97,0
Ag50-Hf50	Moulded	10,97	11,79	90,73
	Sintered	7,75		65,81
	Rapid sint.	11,27		95,6

Table 3.7 Measured and nominal density for moulded, sintered and rapid sintered inserts.

Specimens obtained by means of rapid sintering were all characterized by a compact and uniform microstructure with a low degree of porosity. The EDS elemental analysis was in general quite in agreement with respect to the nominal values, although with the Cu70-Zr30 system differences were significant. At a local scale, microstructure was found to be formed by zones rich in Cu (or Ag) and Zr (or Hf), uniformly distributed through the cross section. The microstructure of the Hf-Ag insert was characterized by finer particles, probably due to the finer size of the constituting powders. The Hf-based and Zr-based zones were found to be surrounded by interdiffusion strips, respectively formed by Hf-Ag-O and Cu-Zr-O. The elemental composition of this areas was found to be similar in the three different batch of Cu-Zr specimens. The thickness of these interaction strips was in general lower than the sintered inserts. XRD analysis, obtained this time in transversal cross section on a plane surface, allowed us to indentify the $Cu_{51}Zr_{14}$ intermetallic in the Cu-Zr rapid sintered specimens.

The density ratio, with respect to the nominal one, achieved values ranging from 93 to 97%, as reported in Table 3.14, significantly higher than the values obtained after conventional sintering.

It is worth making a comment on density measurements. The interaction phases between Cu/Ag and Zr/Hf possibly change the theoretical value of the nominal density, since the intermetallic which forms are characterized by a different specific volume (due to different lattice spacing) with respect to the constituting phases. A rigorous analysis would request a reliable assessment of the amount of this interaction phases (e.g. by means of cross section digital image analyses), which is not trivial especially when composition it not completely uniform, and the knowledge of its density, which was not known for the Ag-Hf intermetallic. Nevertheless, at this stage, nominal density was simply calculated by the rule of mixture based on the powder mixture nominal composition. Although approximated, density measurements have been considered as one of the tools to compare the feasibility of using traditional or rapid sintering methods to produces composite inserts for PAC electrodes. It emerges in particular from these measurement that with the rapid sintering the pellets produced have a density which is much more close to the nominal one.

Drawing partial conclusions, specimens realized through rapid sintering are characterized by a compact and quite homogeneous microstructure, with limited amount of interaction phases, thus leading to a higher density (over 93%) with respect to the traditional sintered inserts (lower than 77%), which are on the contrary characterized by a strong oxidation.

With the final aim of producing electrode inserts for PAC torches, it is of particular importance to achieve the maximum possible density, so to reduce porosity, and to limit as much as possibly the presence of interaction phases which would negatively affect the electrical and thermal conductivity. Moreover, porosity would have a detrimental effect of the component mechanical properties, which are fundamental to withstand the stresses the insert will have to face both during electrode assembly process (e.g. through press fitting) and during cutting. Finally, the gas occluded in porosities could evolve during the cutting process, with unpredictable but most likely negative consequences on the electrode service life.

In view of these analyses, the disk produced by means of rapid sintering were selected to produce composite prototypal inserts for PAC.

3.3. EXPLORATIVE EROSION TESTS

3.3.1 EXPERIMENTAL PROCEDURE

The composite disks obtained by means of rapid sintering, as described in the previous section, were machined to obtain cylindrical inserts characterized by a diameter of 1.5 mm and a length of 4 mm, i.e. the typical dimension for standard Hf insert operating at arc current of 120 A. The inserts where then mounted in standard copper body electrodes by means of press fitting.

Due to specimens availability and difficulty in machining, only three inserts were obtained: one with the Cu50-Zr50 wt.% composition and two with the Ag50-Hf50 wt.% composition. Concerning the latest, only one specimen (which will be referred to as *Ag-Hf (A)*) could be machined with the nominal design length of 4 mm ,while for the second (*Ag-Hf (B)*) a total length of 2 mm was obtained.

Above mentioned electrodes were then mounted on a Cebora Plasma multi-gas plasma torch. Erosion tests on the electrodes have been performed through a Cebora plasma cutting system, comprising the power supply Plasma Prof 164 HQC, equipped with the remote high frequency unit HV18 and the Gas Console PGC1-2 for manual gas settings. The system can operate in the current range 20-120 A. Experiments have been accomplished under operative conditions typically used with standard Hf cathodes in cutting of MS plates 20 mm thick, with O_2 as plasma gas and air as shield gas at 120 A. However, a graphite rotating anode was used to simulate steel cutting process, allowing for material saving.

High speed imaging (HSI) was used to assess the behaviour of the composite inserts during shut down, by comparing it with traditional Hf insert. The process was observed by means of a NAC Memrecam K3R HS camera, capable of acquiring up to 200 frame per second. The camera was mounted coaxially with respect to the PAC torch, so to observe the phenomena occurring on the insert surface during the transitory.

A pilot arc was used, so to have a free axial line-of-sight from the insert surface to the camera.

The electrodes characterized by standard length were first subjected to two subsequent steps of 100 *CCs* (cutting cycles), at the end of which the surface of each electrode was analysed by means of scanning electron microscopy (SEM), performing the elemental analysis through energy dispersive spectroscopy (EDS), whilst phase composition was analysed by micro-Raman spectroscopy (λ=514.5 nm). Topographies of the emitting surfaces where reconstructed from stylus profilometer measurements, when maximum recess depth was lower than the profilometer maximum range. All three electrodes were then brought to the end of service life, i.e. to the point at which a catastrophic failure prevented the accomplishment of any other cutting cycles. The surface of failed composite electrodes were again analyzed according to the above mentioned methods.

The total number of *CCs* achieved by the three electrodes were measured. As a mean of comparison, three standard Hf insert electrodes were also tested at the same operative conditions and brought to the end of their service life.

In order to characterize the electrode cross sections, the portions of the cathodes comprising the composite inserts were first cut, then mounted in epoxy resin and mirror polished with the procedure described in Chapter 2.2 for standard Hf insert electrodes. The cross sections of the electrodes at the end of service life were observed by means of Scanning Electron Microscopy (SEM) and Optical Microscopy (OM).

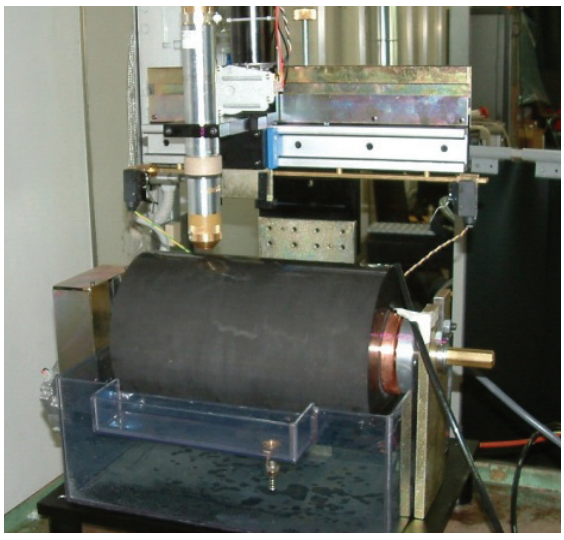

Fig. 3.35 PAC torch mounted on a rotating anode.

3.3.2 RESULTS AND DISCUSSION

3.3.2.1 HIGH SPEED IMAGING OF THE SHUT-DOWN TRANSITORY

High speed imaging demonstrated that, during shut down, the arc off process its significantly faster in the composite inert electrodes with respect to the ones adopting traditional Hf inserts. In particular, solidification occurs more rapidly when the improved inserts comprising a high conductivity phase are used. Fig. 3.36 shows different stages of the arc off transitory in the three different kind of electrodes. In the case of a traditional Hf insert, massive ejection of emissive materials particles was observed (Fig. 3.36 *b*, Hf). On the contrary, no such massive ejection were observed. As discussed in chapter 1 and 2, an imbalance of forces acting on the molten pool occurs during the shut-down transitory, thus causing particles to be . It then clear that if fast solidification is achieved, as for the composite inserts, this massive ejection can be limited.

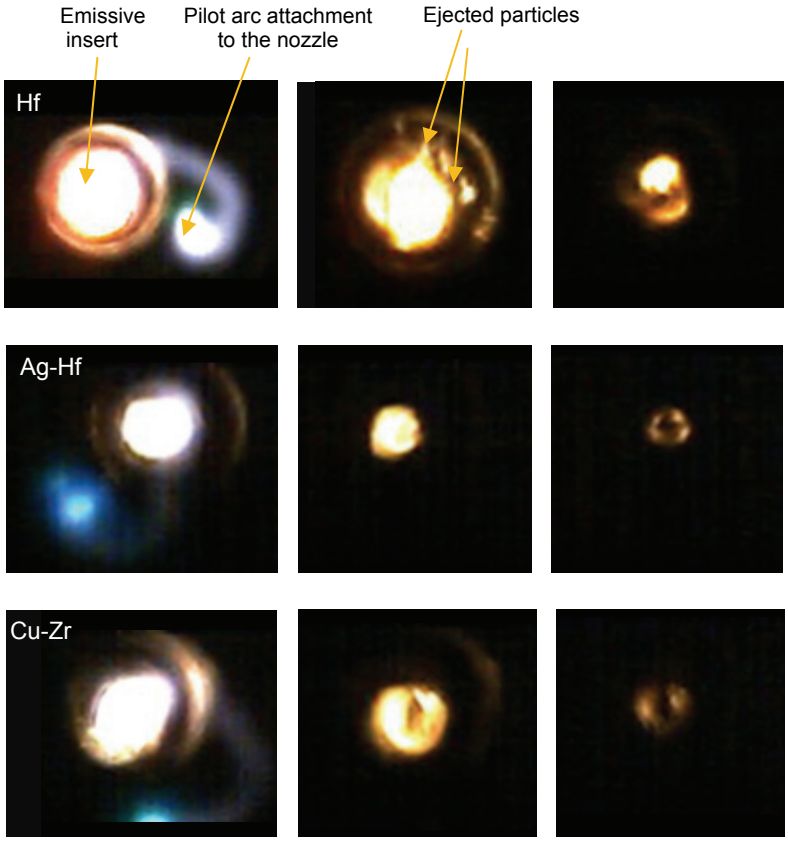

Fig. 3.36 High speed imaging of the shut down process for the Hf, Ag-Hf and Cu-Zr insert electrodes.

3.3.2.2 EROSION TESTS

The results of erosion tests are reported in Fig. 3.37, in terms of maximum achieved number of *CCs* before catastrophic failure of the electrodes. The Hf-Ag (A) electrode achieved a total of 980 *CCs*, while the Hf-Ag (B) electrode, characterized by a length of only 2 mm, achieved 560 *CCs*; this result is still higher than the one achieved by the Cu-Zr insert electrode, whose catastrophic failure occurred at 450 *CCs*. The three standard electrode achieved on average a total service life of 1149 *CCs* with a standard deviation of 213 *CCs*. However, the exiguous number of available composite electrodes does not allow for the drawing of any conclusive assessment on the performance of this electrodes in terms of service life.

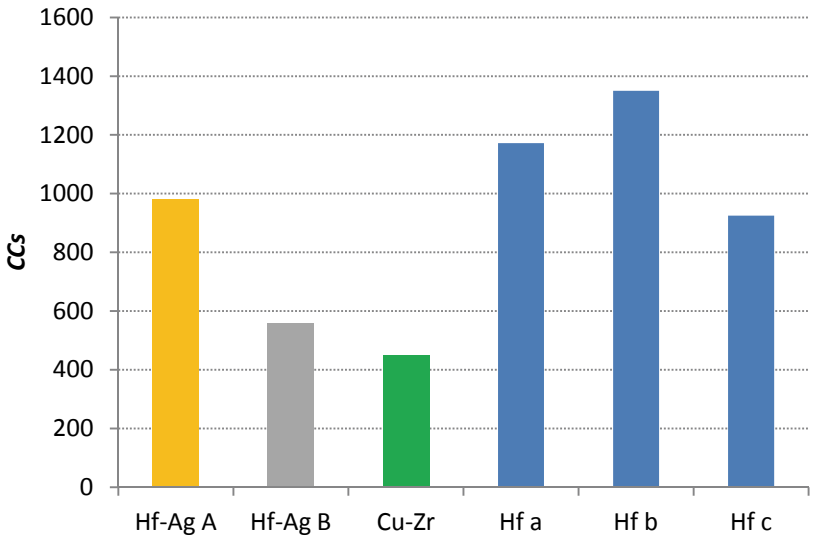

Fig. 3.37 Erosion test results.

3.3.2.3 EMITTING SURFACE ANALYSES

Hf-Ag inserts

Analyses at 100 *CCs* and 200 *CCs* showed that the morphology assumed by the emitting surface of the Ag-Hf (A) electrode is similar to that already observed in Chapter 2 for standard Hf insert, with a central recess cavity and a deposit of emitting material on the periphery of the insert and on the electrode body holder. This morphology is observable in the topography of Fig. 3.38, which shows that the cavity

depth after 100 *CCs* is about 600 µm. Part of the emissive material is ejected and deposits on the nozzle inner surface (Fig. 3. 39). At 200 *CCs*, the erosion cavity depth increases (exceeding the profilometer measurement range) and the deposited volume enlarges, although the morphology appears relatively uniform and generally axisymmetric (Fig. 3.40).

EDS and Raman spectra demonstrated that after 100 *CCs* the external insert surface is covered by a HfO_2 layer with Ag trace. In correspondence of the insert periphery, a slightly higher presence of silver was detected (Fig. 3.41).

At the end of the service life, the insert in not anymore clearly distinguishable on the electrode surface (Fig. 3.43). As confirmed by EDS analyses (Fig. 3.44), the surface is actually covered by a copper oxide layer, with presence of Hf and Ag. This configuration could be the result of an arc attachment to the copper body, which induced its melting and subsequent covering of the composite insert by liquid copper.

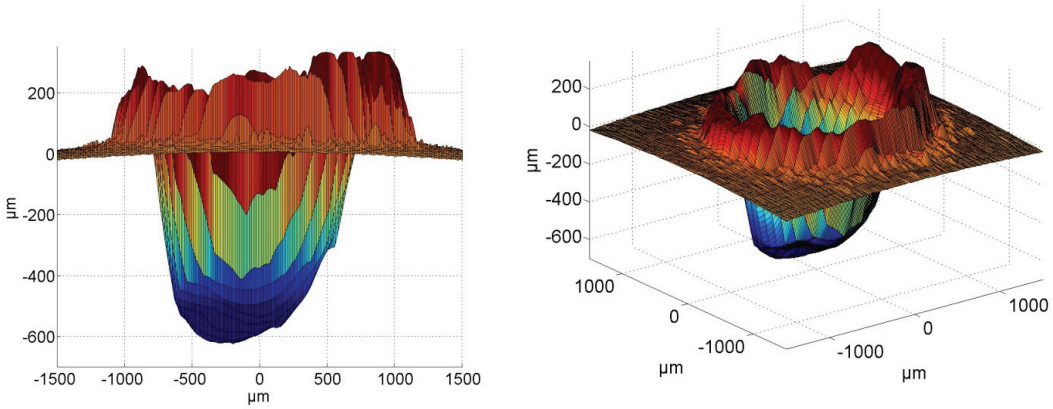

Fig. 3.38 3-D topographies of Hf50-Ag50 at 100 *CCs*.

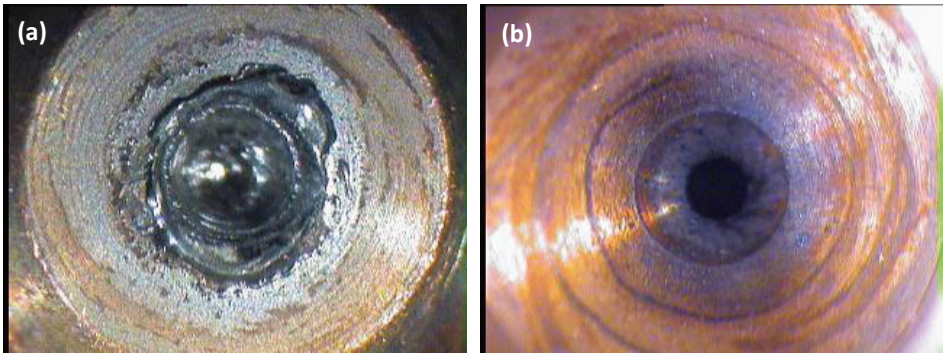

Fig. 3.39 (*a*) Electrode with insert Hf-Ag (A) 100 *CCs*; (*b*) Nozzle internal surface

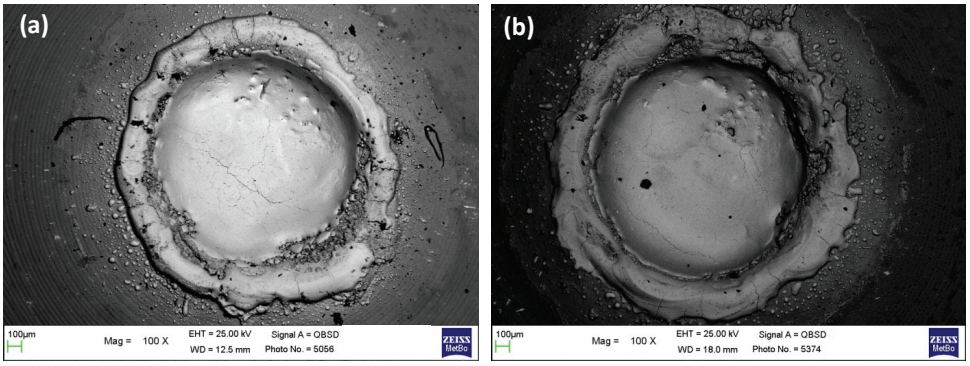

Fig. 3. 40 Ag-Hf (A) at (*a*) 100 *CCs* and (*b*) 200 *CCs*.

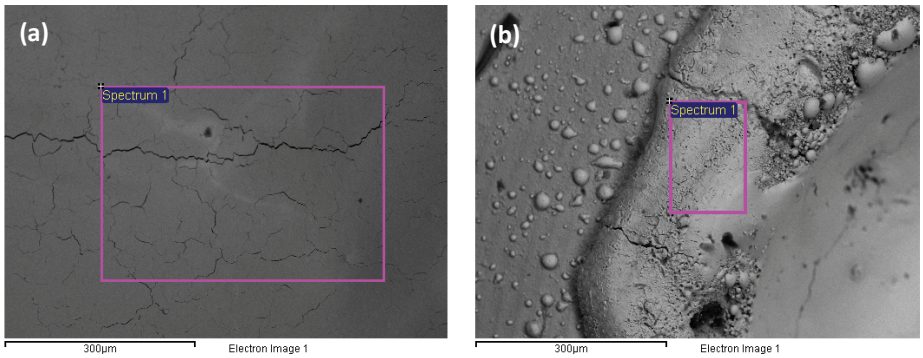

Element	Weight%	Atomic%
O	16	64
Cu	2	2
Ag	16	10
Hf	67	24

Element	Weight%	Atomic%
O	23	76
Ag	2	1
Hf	76	23

Fig. 3.41 EDS Particular of the Ag-Hf emissive insert centre (*a*) and insert periphery (*b*).

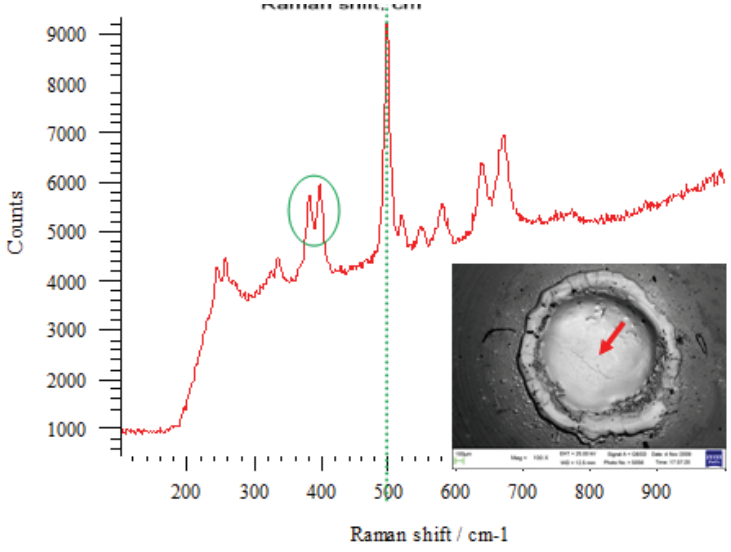

Fig. 3.42 Raman spectrum of the rapid sintered after Hf-Ag insert 100*CCs*.

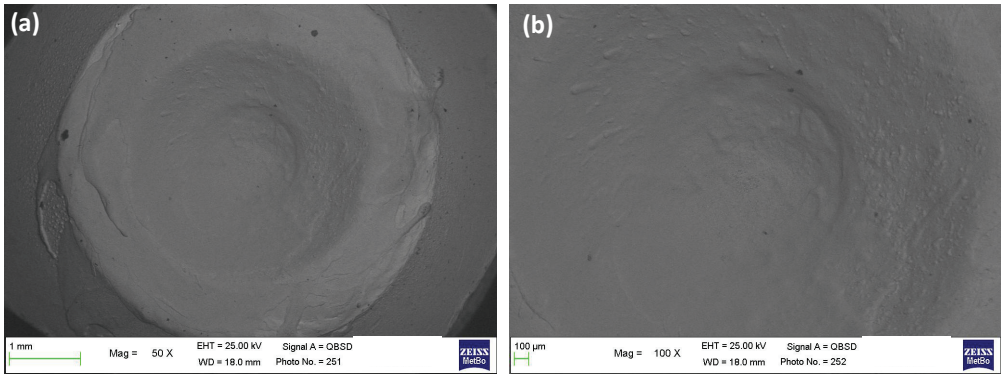

Fig.3.43 SEM: Hf-Ag (A) at 980 *CCs*.

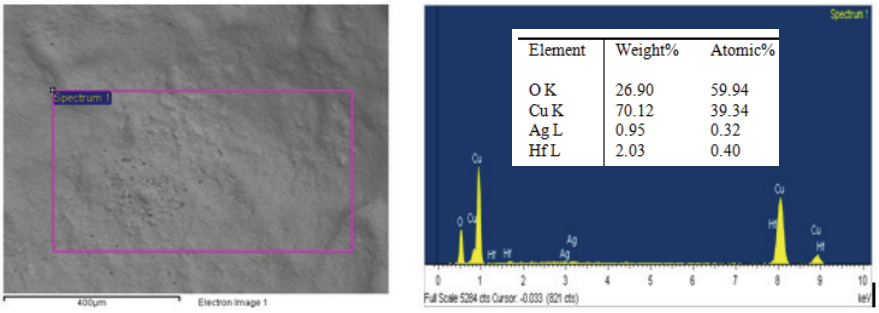

Fig. 3.44 EDS analysis of the Hf-Ag (A) insert centre at 980 *CCs*.

The Ag-Hf (B) electrode showed at the end of its service life (560 *CCs*) an emitting surface characterized by a deep erosion cavity with a significant portion of emissive material which deposited on the copper body (Fig. 3.45 *a*), while further Ag-Hf based material was ejected and deposited on the nozzle inner surface (Fig. 3.45 *b*). EDS analyses revealed that the Ag phase tends to segregate at the insert periphery, leaving a higher portion of Hf in correspondence of the insert central area.

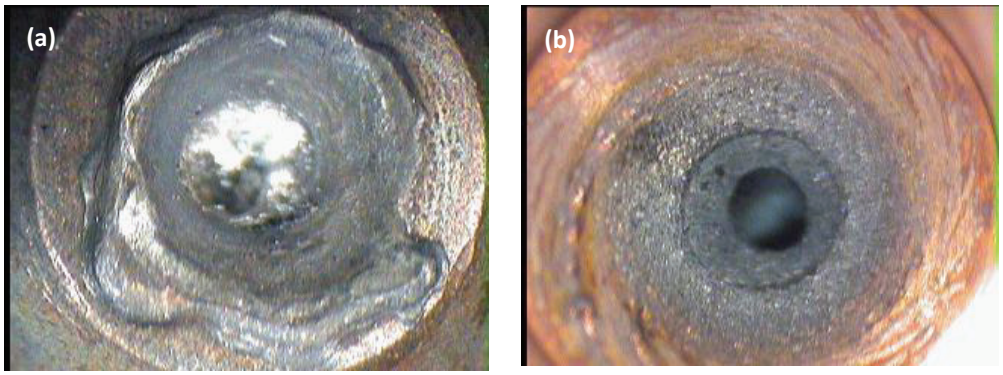

Fig. 3.45 (*a*) Hf Ag (B) 560 *CCs*; (*b*) Corresponding nozzle internal surface.

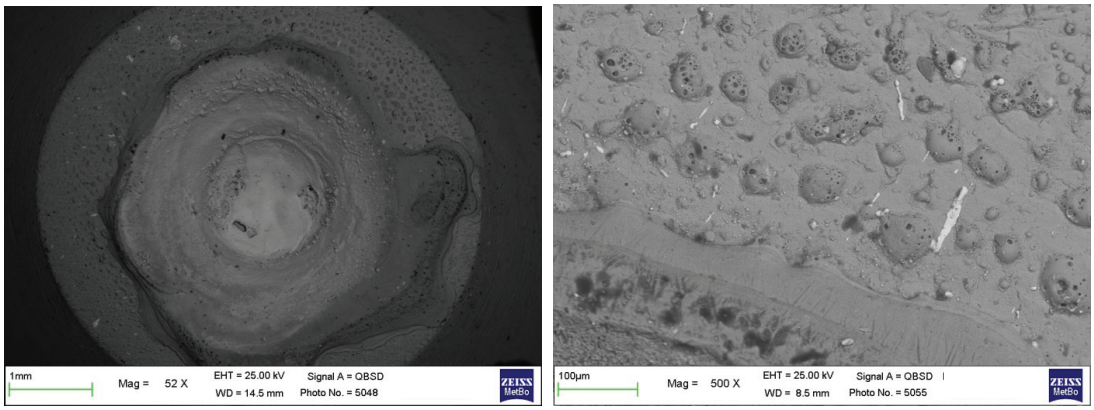

Fig. 3.46 SEM micrographs of the Hf-Ag (B) insert at 560 *CCs*.

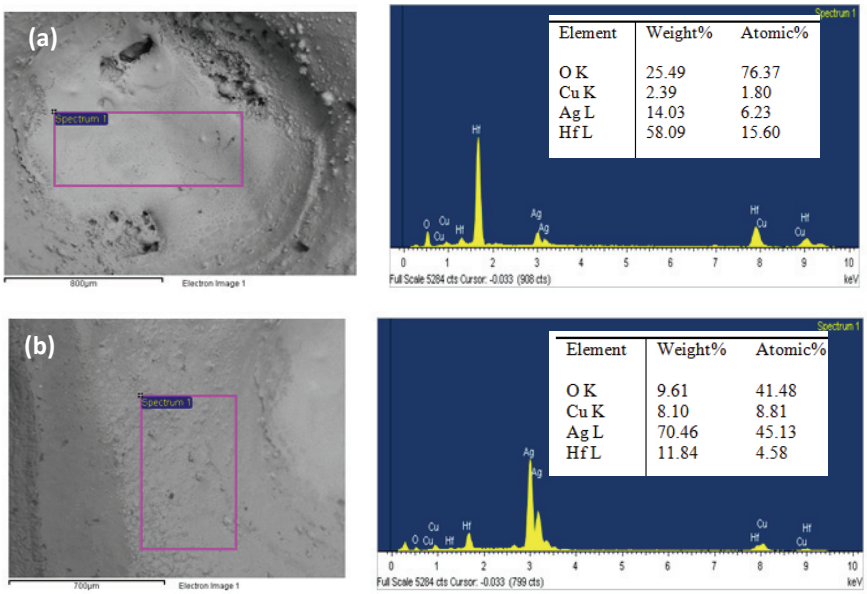

Fig. 3.47 EDS analyses Hf-Ag (B) insert centre (*a*) and insert periphery (*b*) at 560 *CCs*.

Cu-Zr insert

The Cu-Zr insert was characterized by a higher erosion rate with respect to its Ag-Hf competitor, as already at 100 *CCs* its cavity depth was higher than the maximum detectable by the profilometer (about 800 µm). The cavity deepens with increasing *CCs*, and a considerable part of the emissive material solidifies on the copper body or is ejected and partly deposited on the nozzle inner surface. Elemental EDS analysis showed that the external layer at the insert centre is mainly constituted by Zr oxide, with presence of Cu traces. The presence of ZrO_2 both in the insert centre surface layer and on the deposited emissive material is confirmed by Raman spectra. The copper body is

characterized by the presence of large Cu particles (over 100 µm), possibly ejected by the emissive surface, partly covered by Zr oxide.

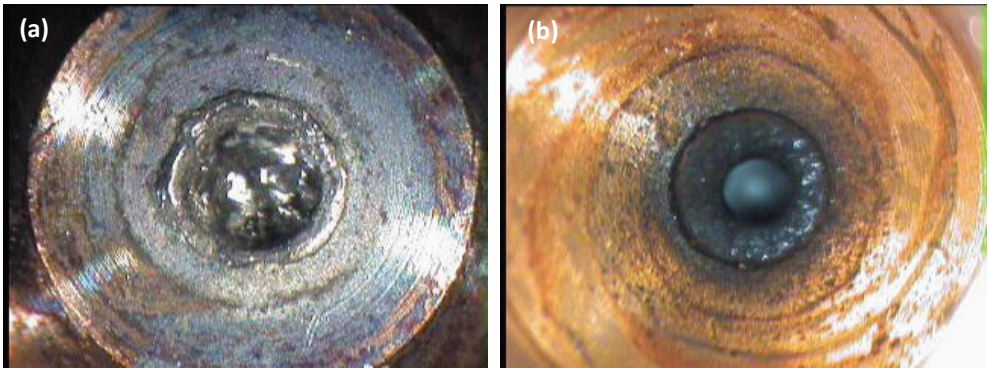

Fig. 3.48 Zr-Cu insert electrode at 100 *CCs* (*a*); (*b*) corresponding nozzle internal surface.

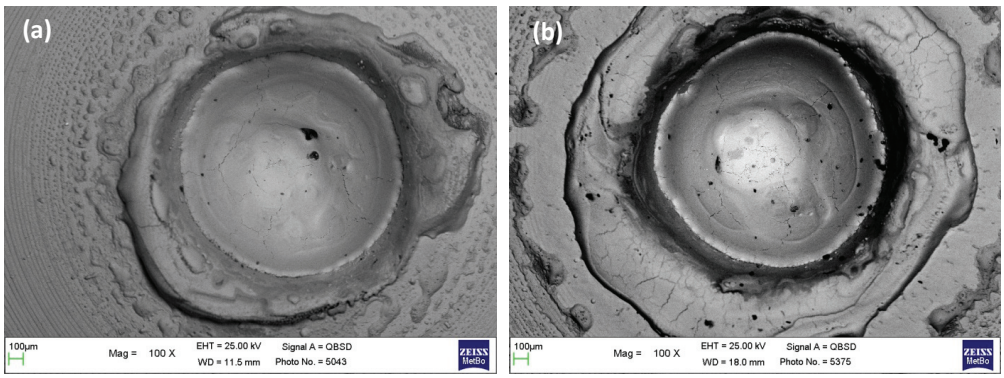

Fig. 3.49 Zr-Cu insert electrode (*a*) at 100 *CCs* and (*b*) at 200 *CCs*.

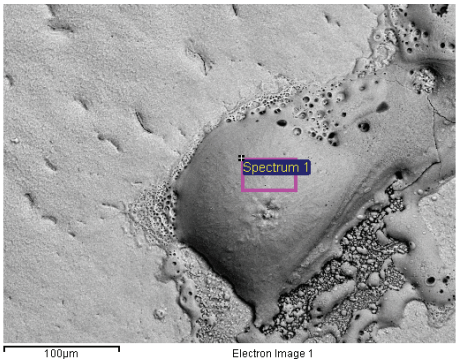

Element	Weight%	Atomic%
O K	18.42	47.65
Cu K	77.62	50.56
Zr L	3.96	1.80

Fig. 3.50 EDS analysis of a Cu particle deposited on the electrode body.

When observed at the end of the service life, the electrode is characterized by a deep erosion cavity with vast portion of emissive material solidified on the copper body. Even in this case, emissive element (Zr) in oxidized form covers the insert centre, while

the peripheral portions owns a higher percentage of Cu. Large copper particles are still observable in Fig. 3. 53.

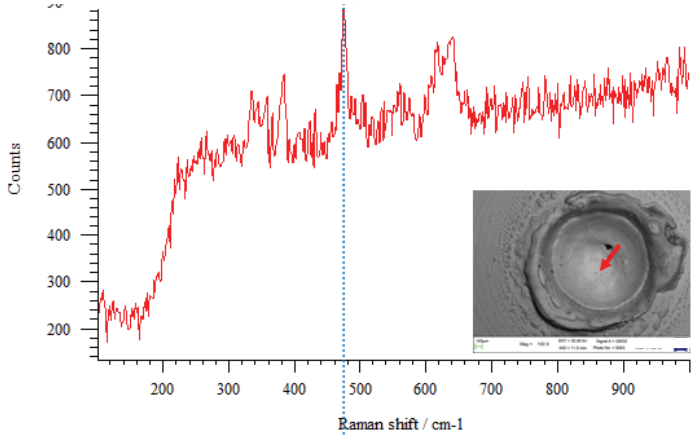

Fig. 3.51 Zr-Cu at 100 *CCs*: insert centre Raman spectrum. The dotted light blue line indicates the ZrO_2 peaks.

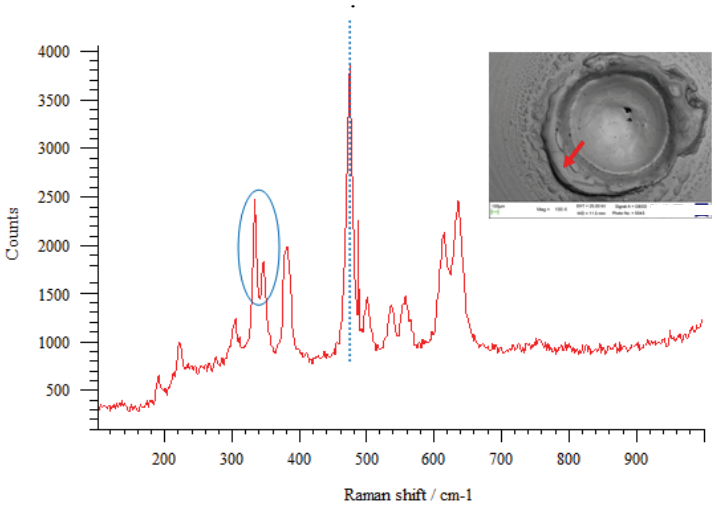

Fig. 3.52 Zr-Cu at 100 *CCs*: insert periphery Raman spectrum. The dotted light blue line and circle indicate the ZrO_2 peaks.

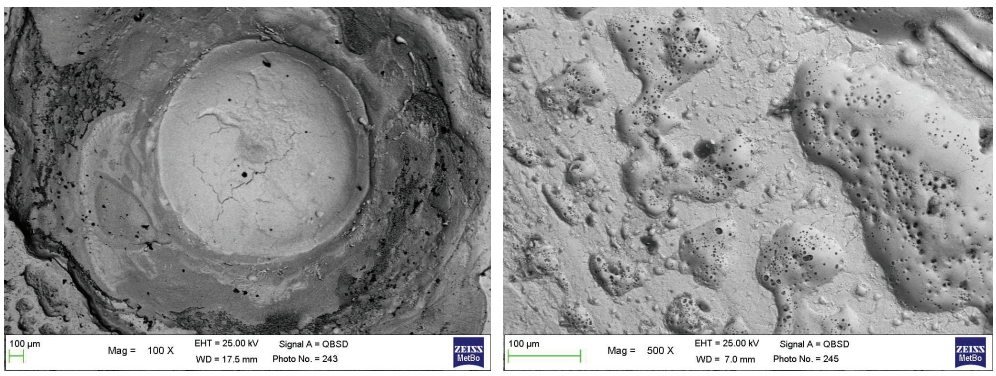

Fig. 3.53 Zr-Cu insert at 450 *CCs*.

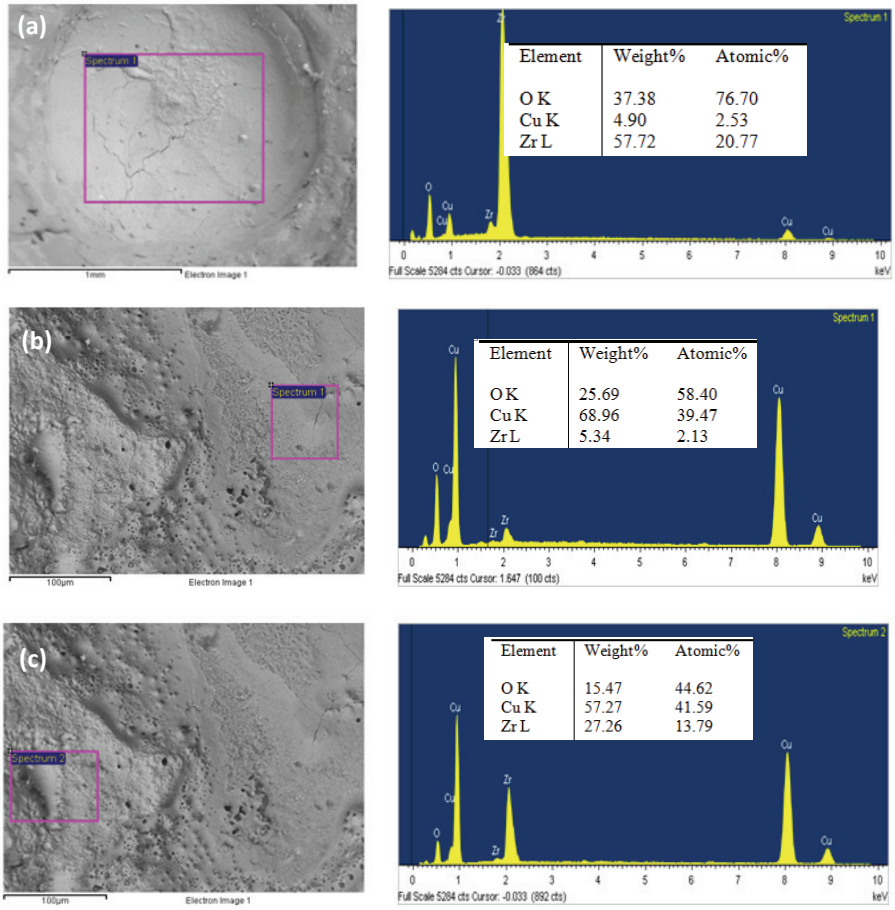

Fig. 3.54 Zr-Cu insert at 450 *CCs:* EDS analyses of the insert centre (*a*) and periphery (*b*).

3.3..2.4 INSERT CROSS SECTION ANALYSES

Hf-Ag (A)

The insert, shown in its complete cross section at the end of service life (980 *CCs*) in Fig. 3.55, is characterized by a erosion cavity depth of 1.2 mm. Although not uniform, a description of the microstructure constituting the insert after the cutting process can be drawn. From EDS elemental analysis of Fig. 3. 44 one can infer that the superficial central part of the insert is mainly constituted by a copper oxide layer, with HfO_2 traces, whose thickness is approximately 80 µm. As anticipated, the presence of Cu in the superior part of the insert is probably related to a destructive attachment of the arc to the copper body. Underneath this layer, an irregular layer of HfO_2 can be observed, with a maximum thickness of 50 µm. A third layer comprises Ag and Cu oxides, with traces of inter-diffused Hf. In some portion of the cross section, between

the second and third layer, a metallic Cu and a metallic Ag layers are present, although very thin (about 20 μm). Since in the described portion of the insert cross section it not possible to distinguish any separate Hf or Ag particles, it is believed that this part underwent melting during cutting process and subsequently solidified to the observed microstructure. Below the third layer, the transition to the original microstructure of the insert begins, as it is possible to observe the Hf particles, surrounded by the interdiffusion strips, dispersed in the metallic Ag matrix. Afore mentioned oxidized layers are interested by relevant porosity.

Finally, a thin oxide layer separates the insert from the copper body. The contact between the two elements appears quite regular, but the presence of this oxide presumably affects the thermal conductivity.

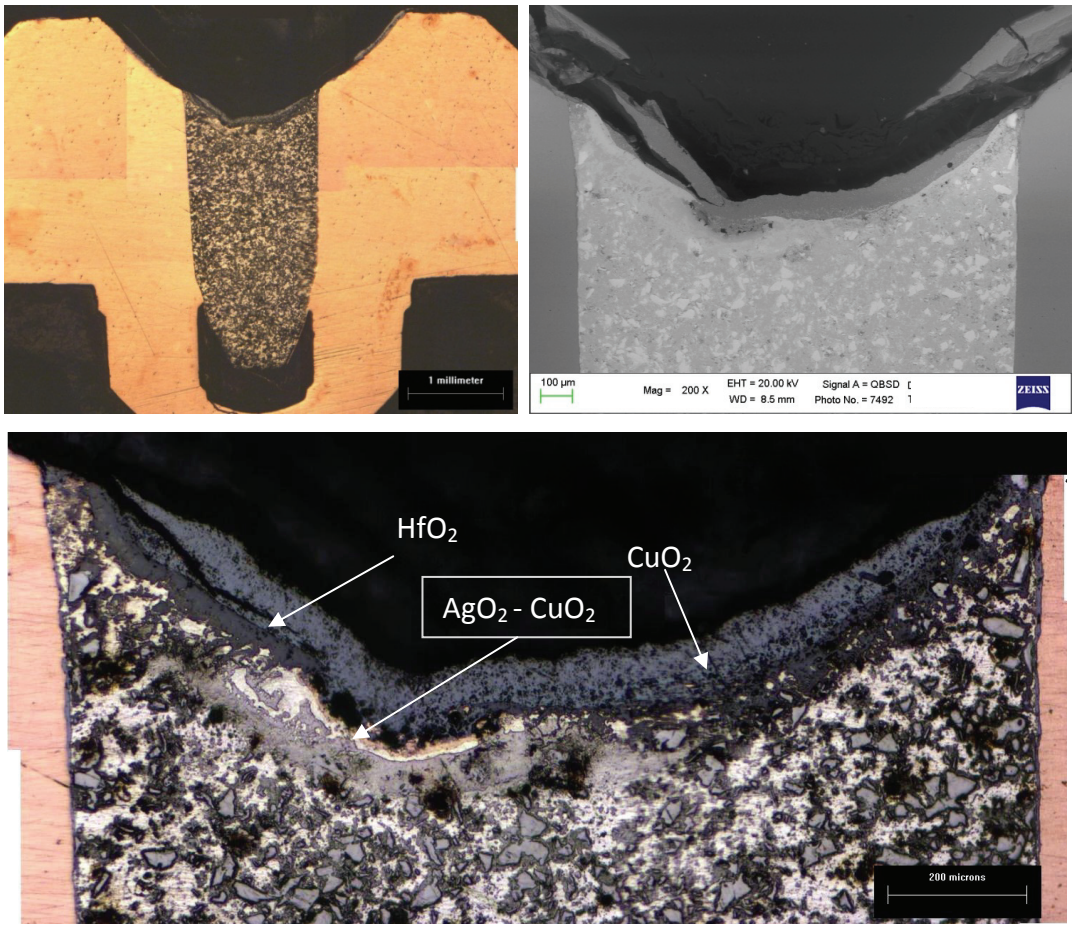

Fig. 3.55 Hf-Ag (A) insert cross section.

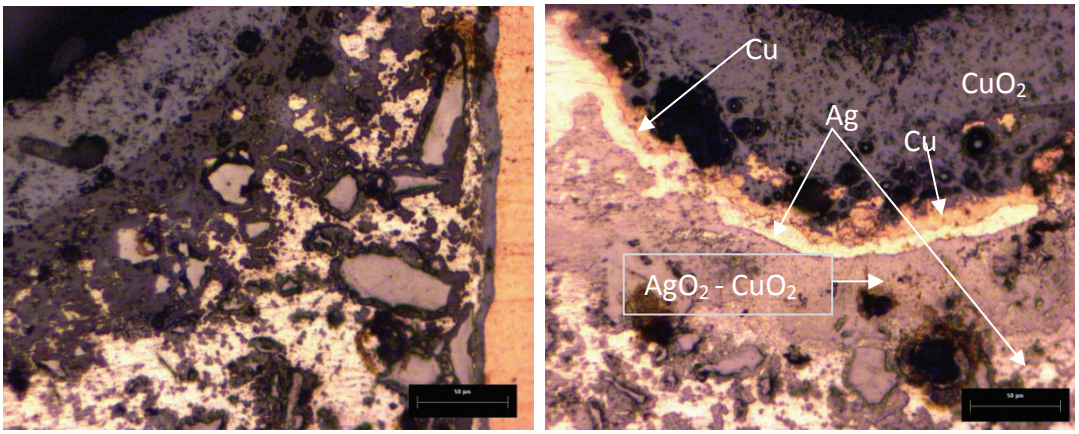

Fig. 3.56 Hf-Ag (A) insert cross section details.

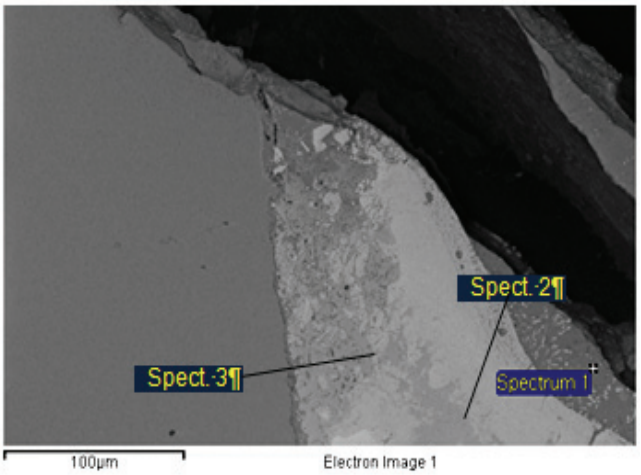

Element	Weight%	Atomic%
Cu K	67.64	45.44
Ag L	3.49	1.38
Hf L	9.82	2.35
O	19.05	50.83

Element	Weight%	Atomic%
Cu K	15.25	14.76
Ag L	4.75	2.71
Hf L	64.28	22.14
O	15.72	60.39

Element	Weight%	Atomic%
Cu K	41.51	33.69
Ag L	37.05	17.71
Hf L	6.99	2.02
O	14.45	46.58

Fig. 3.57 Hf-Ag (A) insert cross section: punctual EDS analysis 1/2.

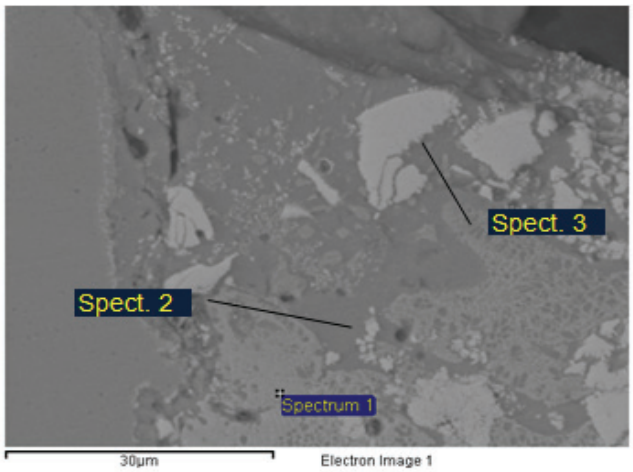

Element	Weight%	Atomic%
Cu K	3.89	4.41
Ag L	62.73	41.83
Hf L	23.53	9.48
O	9.85	44.28

Element	Weight%	Atomic%
Cu K	4.15	4.71
Ag L	68.89	46.11
Hf L	17.64	7.14
O	9.32	42.04

Element	Weight%	Atomic%
Cu K	3.96	4.27
Ag L	14.14	8.98
Hf L	67.72	26.00
O	14.18	60.75

Fig. 3.58 Hf-Ag (A) insert cross section: punctual EDS analysis 2/2.

The Hf-Ag (B) insert showed an erosion cavity depth of 1,3 mm, comparable to that of the Hf-Ag (A) insert. Nevertheless, the shorter insert length could have affected the heat removal process, as the room which is formed between the insert bottom end and the copper body is filled with air, thus badly conducting heat from the plasma process.

In this case, no superficial Cu layer is present. A HfO_2 layer and a zone rich of metallic Ag and a AgO_2 oxide layer with inter-diffused Hf can still be observed. Big pores (up to 100 μm) can be observed in the melted and re-solidified zone.

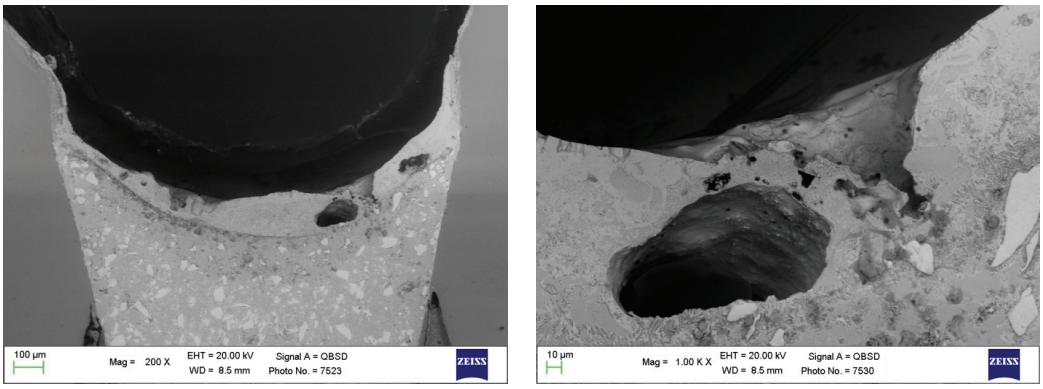

Fig. 3.59 Insert Hf-Ag (B) cross section.

Insert Zr-Cu

The Cu-Zr insert is characterized, at the end of its service life (450 *CCs*), by an erosion cavity depth of about 1.0 mm. Cross sectional micrograph (Fig. 3.60) and EDS analysis confirmed that the inert surface is covered with a layer of ZrO_2, with a minimum thickness of about 50 μm. This relatively compact oxide layer partly penetrates, through oxidation paths, the underlying layer, which is presumably composed of interdiffused Zr, Cu and oxygen. The total thickness of this thermally affected (possibly remelted) zone is about 260 μm

Porosities and some cracks interest the superficial Zr oxide layer, while large porosities are present at the interface between the remelted zone and the portion of insert which did not undergo any melting during the process.

The contact between the insert lateral surface and the copper holder appears regular, although a thin oxide layer was observed.

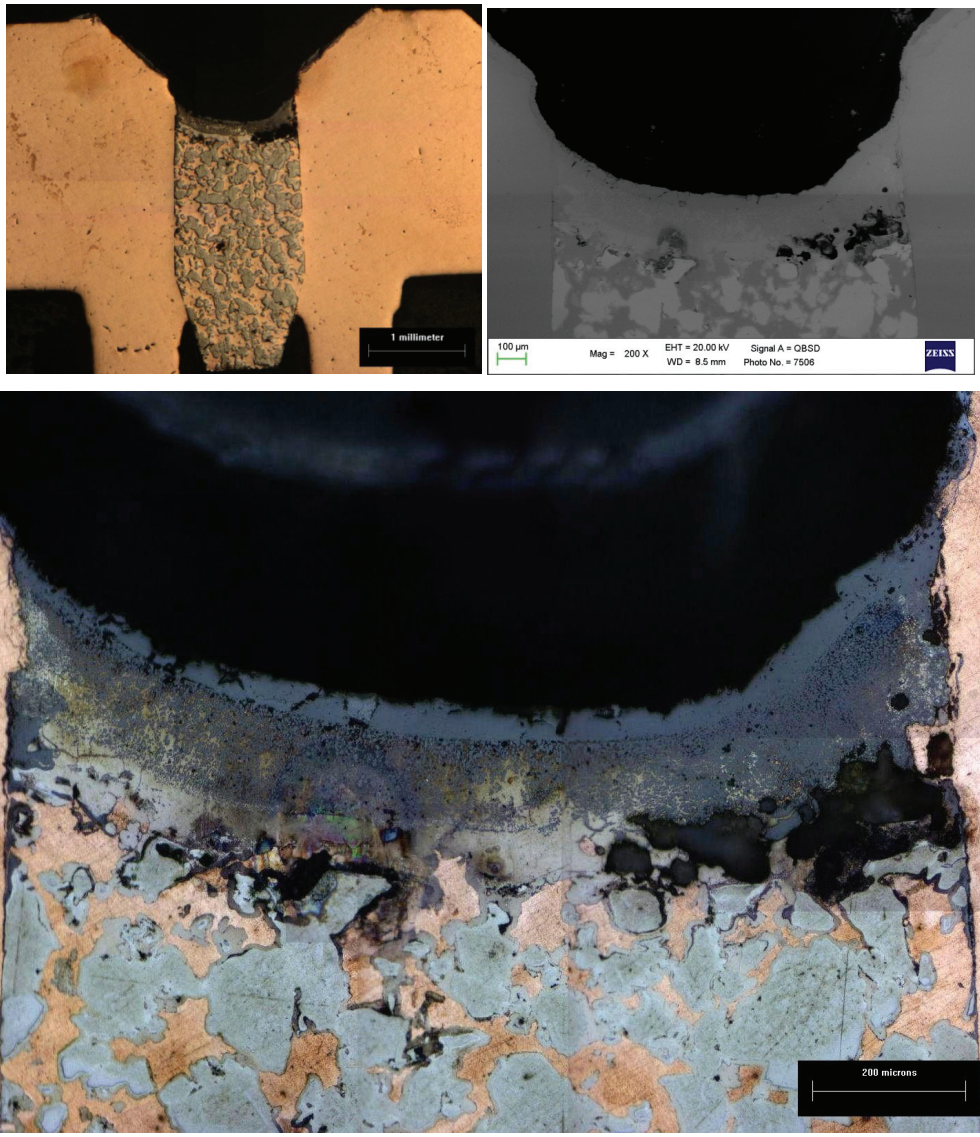

Fig. 3.60 Zr-Cu insert cross section.

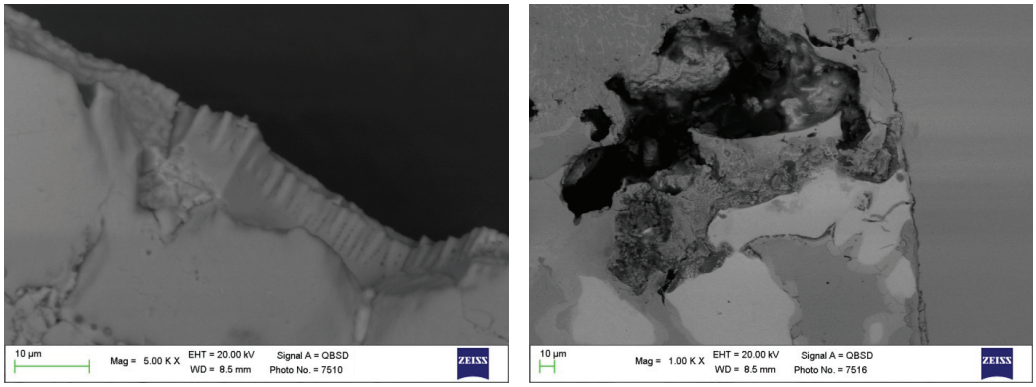

Fig. 3.61 Zr-Cu insert cross section details.

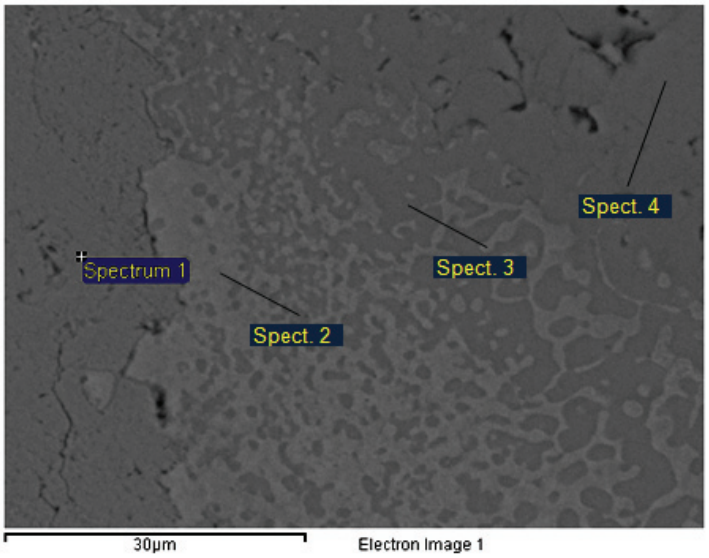

Element	Weight%	Atomic%
Cu K	71.57	44.94
Zr L	7.71	3.37
O	20.72	51.69

Element	Weight%	Atomic%
Cu K	59.44	37.51
Zr L	18.95	8.33
O	21.61	54.16

Element	Weight%	Atomic%
Cu K	18.47	11.85
Zr L	56.91	25.43
O	24.61	62.72

Element	Weight%	Atomic%
Cu K	14.17	9.11
Zr L	60.90	27.26
O	24.93	63.63

Fig. 3.62 Zr-Cu insert cross section: punctual EDS analysis EDS 1/2.

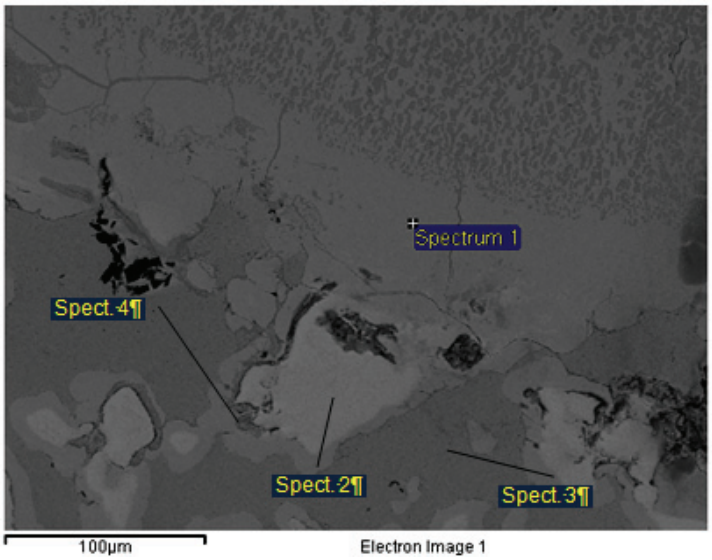

Element	Weight%	Atomic%
Cu K	51.58	32.65
Zr L	26.24	11.57
O	22.19	55.78

Element	Weight%	Atomic%
Cu K	14.14	9.09
Zr L	60.93	27.27
O	24.93	63.64

Element	Weight%	Atomic%
Cu K	66.99	42.15
Zr L	11.95	5.24
O	21.06	52.62

Element	Weight%	Atomic%
Cu K	49.46	31.33
Zr L	28.20	12.44
O	22.34	56.22

Fig. 3.63 Zr-Cu insert cross section: punctual EDS analysis.

3.4 CONCLUSIONS

The results presented demonstrated the feasibility of using composite inserts comprising high conductivity material such as Cu or Ag and a high emissivity material, such as Zr or Hf, for PAC electrodes. The small number of prototypes available to be tested does not allow to draw a conclusive assessment concerning the effective performance of such electrodes with respect to traditional pure Hf inserts. Nevertheless,

the erosion tests, together with microstructural and HSI analysis, suggest that the potential of such electrodes has to be considered for industrial application, although further experimental tests would be required.

The analysis of HS imaging showed in particular as these electrodes are significantly faster than traditional Hf insert in cooling down during the arc off phase. As discussed in the first and second chapters, and observed in the abovementioned images, during this transient the imbalance of fluidynamic force leads to the ejection of massive amount of emissive material. A faster cooling down of the molten emissive pool allows for a significant reduction of this ejection, as the molten pool solidifies in a shorter time.

Microstructural analyses showed that the oxide layer which forms on top of the insert cross section is relatively uniform and thin, without the presence of thick oxide formation in the insert centre, which were on the contrary observed in traditional Hf inserts after a few cutting cycle. The higher cooling rate of such composite inserts, limiting the amount of material which melts during the cutting process, could contribute in decreasing the total amount of dissolved plasma gas in the molten pool. Since this gas is believed to escape from the molten pool during arc off, dragging with it part of the emissive material, this could be a further beneficial effect in containing cathode erosion during shut down. Moreover, cracking and breaking of the oxide layer during arc-on phase is known to be one of the main cause of cyclic erosion, which can possibly be reduced by means of such composite inserts.

In order to assess the potential of such electrodes, a number of issues which could positively impact their properties have to be addressed and should be considered for future works. First, the composition and dimension of powders have to be optimized, although, in order to assure effective heat condition, the high conductive material should be kept at least at a wt.% which would allow for a continuous path across the insert. Then, the insert production process should be further optimized to minimize the presence of interaction phases and to approach full density.

Operating conditions, and in particular current and pressure ramps during transient, should be tailored on the specific insert configurations. Finally, the diameter of the insert should probably be adapted to the new insert properties in terms of heat conduction and thermionic emissivity. Is was in fact demonstrated how this diameter

should be large enough to sustains the arc, but as small as possible to effectively conduct heat, depending on the insert physical and chemical properties, i.e. on their composition.

CHAPTER 4

NET EMISSION COEFFICIENT OF ARGON PLASMAS

ABSTRACT

Radiative emission represents a significant component of energy transport in thermal plasmas and cannot be neglected in plasma torch modelling. A detailed line-by-line method was implemented to compute the net emission coefficient of Ar plasmas at temperatures ranging from 3000 K to 25000 K and pressure ranging from 50 kPa to 200 kPa for optically thin and partially auto-absorbed plasmas. Species and emission mechanisms fractional contributions to the volumetric emission coefficient were determined. Both continuum emission and line emission including broadening effects were considered for calculations. The implemented model is suitable for performing calculation of the net emission coefficient at different plasma thickness, by considering the absorption over a large wavelength spectrum. Results obtained from the present model were compared to published theoretical and experimental data.

4.1 INTRODUCTION

Argon plasmas are widely used in many industrial and research applications, such as plasma arc cutting and welding, spray-coating, nano-particles synthesis and waste treatment. Radiative processes often represent an important component in energy transport, and the calculation of the divergence of the thermal plasmas radiative flux is necessary in plasma arc and plasma torch modelling.

The use of the net emission coefficient (NEC), as defined by Lowke [61], in the

transport energy equation, allows for the calculation of the temperatures of the hottest zones of plasmas with sufficient accuracy, as demonstrated in [62]. On the other side, net emission coefficient is useful in computing the amount of radiant energy lost from a plasma when temperatures are known. The NEC represents the difference between the power radiated by a volume unit and the radiation proceeding from other regions of the plasma and absorbed in this volume unit. Although it is a crude representation of the radiative source term, the computation of NEC is often convenient with respect to alternatives such as doing a detailed radiative transport analysis [63], using the method of partial characteristics [64, 65] or mean absorption coefficients [66]. In particular, to accomplish a detailed radiative transport analysis, such a great deal of computational power and fundamental property data are needed that the computation may even become impossible for complex plasma models. Despite considerably simpler, the methods of partial characteristics is still highly demanding in terms of computing time. On the other hands, with respect to NEC, the use of means absorption coefficients considerably simplify the spectral dependence of radiation by supposing that the plasma behaves as grey body (a medium in which the absorption coefficient is independent on the wavelength), with constant abortion coefficients in different bands or frequency intervals, although it allows for the calculation of radiation in the peripheral (colder) zone of plasmas.

Due to their popularity, Argon plasmas are among most studied plasmas. Different authors computed the emissive radiation of Ar argon plasmas by means of its NEC, either in its pure state or comprising metallic vapours. Significant differences exist among the results presented by different authors, especially for optically thick plasmas [67, 68, 69, 70, 71]. Moreover, presented results often consider different conditions such as spectrum range and pressures. It is worth mentioning that the computed radiative properties are not purely a function of the theoretical model being used and assumptions made, but are also dependent on the accuracy and amount of fundamental atomic data (e.g. energy levels, lines, transition probabilities) used in the analysis. Moreover, also due to difficulties in measuring the vacuum ultraviolet portion of the spectrum, there are no measurements of total optically thin emission coefficients (net emission coefficients with a zero path length) over the entire spectrum, in any type of plasma. Measurements of optically thin emission coefficients have been made over a

portion of the spectrum, as performed by Evans and Tankin for argon in the 0.2–3.5 μm range [69].

Having detailed Ar plasma properties describing the radiative emission is valuable to those interested in obtaining temperature profiles or computing heat fluxes. The knowledge of the dominating radiation mechanisms, species and spectral emission coefficient over a large spectrum span at different pressures and temperatures is needed for these purposes. Published results could not supply the complete set of data necessary to pursue this tasks. For the above mention reasons, a model was developed to compute the net emission coefficient of Ar thermal plasmas over a wide spectrum in the 3000 K – 25000 K temperature range, selected as the one of main interest for industrial Ar plasmas thermal applications, both for optically thin and opaque plasmas at different plasma pressures. The results obtained have been compared both with experimental measures and computed literature data.

4.2 RADIATIVE PROCESSES IN THERMAL PLASMAS

The radiative energy that escapes from the section *dS* in the solid angle *dΩ, in direction* θ with respect to the normal *n* of the surface *dS*, in the time interval *dt* and frequency interval between *v* and *v*+*dv*, can be written as [1]:

$$dE_v(\theta,\varphi) = I_v(\theta,\varphi)dvdS\cos(\theta)d\Omega dt \qquad (4.1)$$

where $I_v(\theta,\varphi)$ its the monochromatic intensity of the radiation, expressed in J/(ster m^2) and referred to the unit of time, frequency and surface.

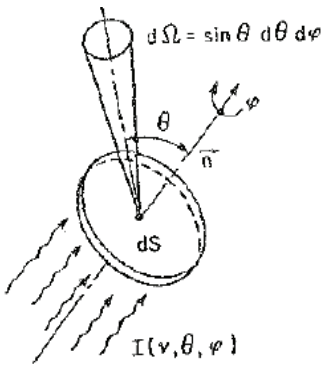

Fig. 4.1. Radiative energy crossing the section *dS* in the solid angle *dΩ [1]*.

Assuming local thermodynamic equilibrium (LTE) and neglecting light diffusion, the radiative transfer equation can be expressed as [61]:

$$n \cdot \nabla I_\nu(r,n) = \kappa'_\nu (B_\nu - I_\nu) \tag{4.2}$$

where B_ν is the black body radiation, I_ν is the radiation monochromatic intensity (expressed in W/(sr m^2), K'_ν is the absorbtion coefficient for length unit and $n(\theta,\varphi)$ is the unity vector defining the radiation direction.

The absorption coefficient K'_ν is related to the spectral emission coefficient ε_ν through Kirchhoff's law:

$$\kappa'_\nu = \varepsilon_\nu / B_\nu \tag{4.3}$$

Black body radiation is defined by Plank's law, with $I_\nu d\nu = I_\lambda d\lambda$:

$$B_\nu d\nu = \frac{2h\nu^3}{c^2} \frac{d\nu}{\exp[h\nu/(kT)]-1} \tag{4.4}$$

$$B_\nu d\lambda = \frac{2hc^2}{\lambda^5} \frac{d\lambda}{\exp[hc/(kT\lambda)]-1} \tag{4.5}$$

If the propagation medium is considered as isotropic, the radiative transport equation can be written as:

$$\nabla \cdot F_{R\nu} = 4\pi(\varepsilon_\nu - J_\nu \kappa'_\nu) = 4\pi\varepsilon_{N\nu} \tag{4.6}$$

where $F_{R\nu}$ and J_ν represent respectively the radiative flux and the mean radiation intensity, defined as:

$$J_\nu = \frac{1}{4\pi} \int_0^{4\pi} I_\nu d\Omega \tag{4.7}$$

$$F_{R\nu} = \int_0^{4\pi} I_\nu n d\Omega \tag{4.8}$$

The term $4\pi\varepsilon_{N\nu} = 4\pi B_\nu \kappa'_\nu$ represents the volumetric net emission coefficient (W/m^3), i.e. the difference between the volumetric emission coefficient $4\pi\varepsilon_\nu$ and the

volumetric absorption $4\pi J_\nu \kappa'_\nu$. Eq. 4.6 equation basically states that the divergence of the radiation flux per unit frequency is equal to the net radiation emitted [72].

In most cases, the temperature distribution along the arc plasma radius (DC plasma jets or RF plasma jets downstream of the induction coil) can be represented by a function such as [1]:

$$\frac{T}{T_{\max}} = (1 - r/R)^n \qquad (4.9)$$

where T_{max} represents the temperature on the central axes and R the plasma jet radius. However, the use of this profile in Eq. 4.6 would make the computation of the radiative emission extremely tedious and complex. Rahmani [73] demonstrated that, for this purpose, it is often possible to substitute this kind of profile with a rectangular profile, where $T=T_{max}$ for $r < R$ and $T=0$ for $r \geq R$ (Fig. 4.2).

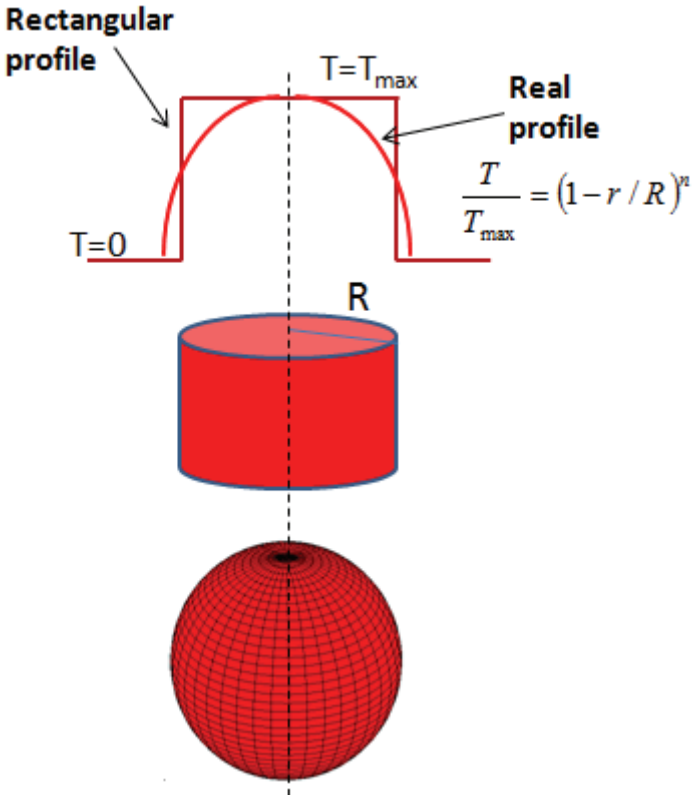

Fig. 4.2 Approximation of the temperature profile: isothermal cylinder and isothermal sphere

Now the problem becomes that of computing the radiative transport in a isothermal cylinder of temperature $T=T_{max}$ and radius R. Lowke [1] demonstrated that

under these hypothesis it is possible to use an effective emission coefficient ε_N , corresponding to the effective radiation emitted from the cylinder axes. In particular, this emission represents the fraction of the total power that is radiated per unit volume and unit solid angle and escapes into a volume element surrounding the axis of the cylinder, after crossing a thickness *R* (or *L*) of the isothermal plasma. In other terms, the net emission coefficient ε_N then represents the difference between the emitted and absorbed power for unit volume and solid angle in a fixed point for a homogeneous and isothermal plasma. It can be expressed as [1]:

$$\varepsilon_N(T) = \int_0^\infty B_\nu \kappa'_\nu \, G_1(\kappa'_\nu \, R) d\nu \tag{4.10}$$

where G_1 is a function accounting for the cylindrical geometry.

In turn, the isothermal cylinder can be approximated as an isothermal sphere with same radius *R*, maintaining an accuracy in the emission calculation higher than 90%, as shown by Libermann and Lowke [72]. In this case, the radiative transfer equation can be written as a function of frequency or wavelength, respectively as:

$$\varepsilon_N(T) = \int_0^\infty B_\nu \kappa'_\nu \exp(-\kappa'_\nu \, R) d\nu = \int_0^\infty \varepsilon_\nu \exp(-\kappa'_\nu \, R) d\nu \tag{4.11}$$

$$\varepsilon_N(T) = \int_0^\infty B_\lambda \kappa'_\lambda \exp(-\kappa'_\lambda \, R) d\lambda = \int_0^\infty \varepsilon_\lambda \exp(-\kappa'_\lambda \, R) d\lambda \tag{4.12}$$

4.2.1 SPECTRAL EMISSION COEFFICIENT

The spectral emission coefficient ε_λ (or ε_ν) represents the radiation emitted (radiative power) at wavelength λ (frequency *v*), for unit volume and unit solid angle. It comprises three contributions, according to the different emission mechanism (Fig. 4.3):

$$\varepsilon_\lambda = \varepsilon_{\lambda,L} + \varepsilon_{\lambda,fb} + \varepsilon_{\lambda,ff} \tag{4.13}$$

where

$\varepsilon_{\lambda,L}$ = line emission coefficient (*bound-bound* transitions)

$\varepsilon_{\lambda,fb}$ = continuum emission coefficient: radiative recombination (*free-bound* transitions)

$\varepsilon_{\lambda,ff}$ = continuum emission coefficient: *bremsstrahlung* (*free-free* transitions)

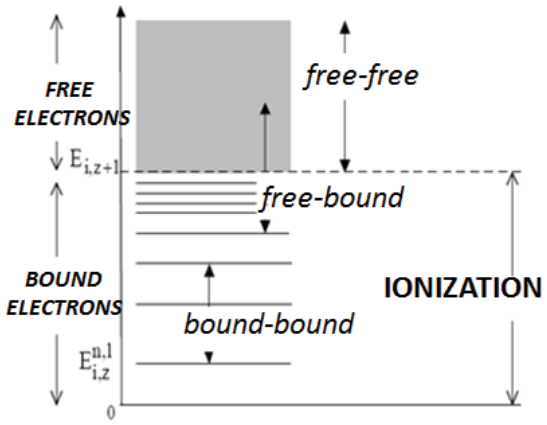

Fig. 4.3 Excited states of an atom or an ion and the corresponding bound-bound, free-bound, and free--free transitions (after [74]).

Differently from ε_N, ε_λ does not consider any type of absorption.

4.2.2 Continuum Spectral Emission

Radiative recombination (free-bound transitions)

The recombination processes of free electrons with a ion of charge Z (A^{Z+}), or an atom, results in a continuum emission in the spectrum, due to the non-quantized energy that free electrons can assume:

$$A^{Z+} + e^- \Leftrightarrow A_i^{(Z-1)} + h\nu \tag{4.14}$$

The expression for the spectral emission due to these kind of processes was introduced by Cabannes and Chapelle [74], and proposed by Wilbers *et al*. [75] as follows:

$$\varepsilon_{fb}(\lambda) = \sum_z \frac{C_1}{\lambda^2}\frac{n_e n_z}{\sqrt{T_e}} Z^2 \left[1 - \exp\left(-\frac{hc}{\lambda k T_e}\right)\right]\frac{g_{z,1}}{Q_z}\xi_{fb}$$

$$C_1 = \frac{16\pi\left(\frac{e^2}{4\pi\varepsilon_0}\right)}{3c^2\sqrt{6k\pi m_e^3}} \tag{4.15}$$

where

$g_{z,1}$ = statistical weight of the first energy level of the *Z*-th ion

Q_z= internal partition function (or sum over all states *s*) of the Z-th ion:

$$Q_z = \sum_s g_s \exp\left(-\frac{E_s}{kT}\right) \tag{4.16}$$

$\xi_{fb}(T_e, \lambda, Z)$ = Biberman factor, which represents a weighted sum of the photo-absorption sections taking into account the difference of the Ar energy level structure with respect to that of hydrogen [76, 77].

Bremsstrahlung (free-free transitions)

In *bremsstrahlung,* or braking radiation, free electrons lose a portion of its energy when braked by the electric field of positive ions.

This non- quantized amount of lost energy is converted into radiation according to:

$$A^{z+} + [e^-]_{Vi} \Leftrightarrow A_i^{z+} + [e^-]_{Vf} + h\nu \tag{4.17}$$

$$h\nu = \frac{1}{2} m_e (V_f^2 - V_i^2) \tag{4.18}$$

where V_i and V_f represent respectively the initial and final electron velocities. The formula describing this type of spectral emission is proposed again by [74, 75] for electron-ions interactions as

$$\varepsilon_{ff}^{ei}(\lambda) = \sum_z \frac{C_1}{\lambda^2} \frac{n_e n_z}{\sqrt{T_e}} Z^2 \exp\left(-\frac{hc}{\lambda k T_e}\right) \frac{g_{z,1}}{Q_z} \xi_{ff} \tag{4.19}$$

and for electron-neutrals interactions as

$$\varepsilon_{ff}^{ea}(\lambda) = \frac{C_2}{\lambda^2} n_e n_a \sqrt{T^3} q(T_e) \left[\left(1 + \frac{hc}{\lambda k T_e}\right)^2 + 1\right] \exp\left(-\frac{hc}{\lambda k T_e}\right) \tag{4.20}$$

where $\xi_{ff}(T_e, \lambda, Z)$ represents the Biberman factor for electron-ion braking radiation [76, 77].

4.2.3 LINE SPECTRAL EMISSION

The spontaneous transition of an exited electron from a higher energy level E_u (*upper*) to a lower energy level E_l (*lower*) in ions and neutrals causes a spectral line emission whose centre is given by:

$$\lambda_{ul} = \frac{hc}{E_u - E_l} \tag{4.21}$$

Assuming a Boltzman distribution of the energy levels for each specie *S*,

$$\frac{n_{S,u}}{n_S} = \frac{g_{S,u}}{Q_S} \exp(-\frac{E_{u,S}}{kT}) \tag{4.22}$$

it is possible to calculate the spectral line emission coefficient for a single line, resulting from the *u*-*l* levels transition, as:

$$\varepsilon_{L_{ul}}(\lambda) = \frac{hc}{4\pi\lambda_{ul}} A_{ul} n_u P_{ul,\lambda} \tag{4.23}$$

where

A_{ul} = transition probabilities (s^{-1}), i.e. the probability per second that an atom in the state *u* will spontaneously decay to state *l* by emitting a photon

n_u = number density of upper level *u*

$P_{ul,\lambda}$ = normalized profile of line emission.

4.2.3.1 LINE BROADENING

The interactions due to the presence of other ions, atoms and free electrons cause the emitted radiation to be not monochromatic. The line is indeed characterized by a broadening, with a *half width at half maximum* (HWHM or δ), and can be shifted of $\Delta\lambda$ with respect to the expected line centre λ_{ul}.(Fig. 4.4).

There are basically two types of broadening described in the literature: Doppler broadening and collision broadening (pressure broadening including Stark effects) [79]. Collision broadening comprises resonance, Van der Waals and Stark broadening. Natural broadening is considered negligible.

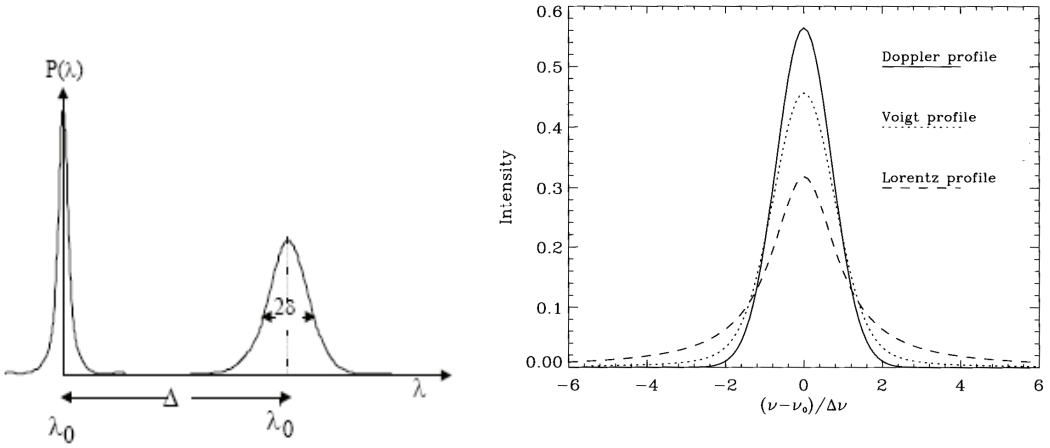

Fig. 4.4 Spectral line broadening and shifting; b) Lorentz, Doppler and Voigt profiles with the same half width [78]

Doppler Broadening. Doppler broadening is due to the thermal random motion of the emitting atoms or particles and depends on the temperature and the mass of the particle. The Doppler broadening has a Gaussian line shape with a full width at half maximum (FWHM or 2δ) [80]:

$$2\delta_D = 7.162 \cdot 10^{-7} \lambda_0 \sqrt{\frac{T}{M}} \tag{4.23}$$

where M is the atomic mass of the emitter in atomic mass units and λ_0 the wavelength in nm. The line profile can be then expressed as [80]:

$$P_{ul}^{G}(\lambda) = \exp\left(-\ln(2)\left(\frac{\lambda - \lambda_0}{2\delta_D} \right)^2 \right) \tag{4.24}$$

Resonance broadening. Resonance broadening occurs when either the upper or the lower level of the transition is a resonance level broadened by collisions with alike atoms. The formula for the FWHM is, in cm [80]:

$$2\delta_R = 8.61 \cdot 10^{-14} \sqrt{\frac{g_1}{g_R}} \lambda_o^2 \lambda_R f_R N \tag{4.25}$$

with $N = p/(k_B T)$ in cm^{-3}, wavelengths in cm as well, the suffix R referring to the resonant level and f representing the oscillator strength.

Van der Waals broadening. Van der Waals broadening is a broadening effect due to neutral perturbers, most common in low electron density zones. The FWHM in cm can be computed according to [81]:

$$2\delta_{vdW} = 8.18 \cdot 10^{-26} \lambda_o^2 \lambda_R \left(\overline{R}^2\right)^{\frac{2}{5}} T^{\frac{3}{10}} N \cdot \sum_i \left(\frac{\alpha^{\frac{2}{5}} \chi}{\mu_i^{3/10}} \right) \tag{4.26}$$

with the wavelength λ_0 in nm, the neutral particle density N, in cm^{-3}, the reduced mass μ in atomic mass units, i representing the neutral species present in the plasma, χ the fraction of the pertuber, α the polarizability of the pertuber (1.64×10^{-24} cm^3 for Ar), $\overline{R}^2$ is the difference of the square radius of the emitting atom in the upper and lower levels, which can be calculated by applying the Coulomb approximation [82].

Stark broadening. Stark broadening is due to the interaction with micro-electric field of other charged particles such as electrons and ions. The broadening by electrons is relevant from the impact theory, whereas the effect of ions, owing to their slow motion, is relevant from a quasi-static theory. When the perturbation involves electrons, the Lindholm-Foley collision approximation leads to the following equations, respectively for neutrals (e-N) and ions (e-I) [83, 84]:

$$2\delta_{S,e-N} = 11.37 C_4^{2/3} V_e^{1/3} n_e \frac{\lambda_0^2}{2\pi c} \tag{4.27}$$

$$2\delta_{S,e-I} = 200.284 C_4^{2/5} \frac{Z^{4/5} n_e}{T^{1/2}} \frac{\lambda_0}{2\pi c} \tag{4.28}$$

where $V_e = \sqrt{8kT/\pi m_e}$ is the mean electrons velocity. In the case of non-hydrogenic emitters, the Stark effect constant C_4 is given by [84, 85]:

$$C_4 = C_{4,i} - C_{4,f} \tag{4.29}$$

where i and f represent the initial and final level. C_{4i} is calculated as:

$$C_{4,i} = \frac{e^2}{3\hbar g_i} \sum_j \frac{S_{ij}}{E_i - E_j} \tag{4.30}$$

where S_{ij} represents the line strength and ħ the reduced Plank constant, with the summation accomplished over all the levels E_j in the neighbourhood of level E_i for which optical transition exists. C_{4f} is computed with an analogous formula. Finally, the influence of ions can be taken into account with the quasi static method of Griem [79].

For each line, all collision broadening effects can be summed,

$$\delta_C = \delta_R + \delta_{vdW} + \delta_S \tag{4.31}$$

giving rise to a Lorentzian line profile, which can be expressed in the normalized, form as:

$$P_{ul}^{L}(\lambda) = \frac{\delta_C}{\pi\left((\lambda - \lambda_0)^2 + {\delta_C}^2\right)} \tag{4.32}$$

The profile resultant from a contribution of Doppler and pressure related effect can be obtained by a Voigt convolution [Voigt] of the Lorenztzian and Gaussian profiles, which can be expressed, in the analytical form, as [83]:

$$P_V(\lambda) = \frac{1}{2\delta_D \pi^{3/2}} \int_{-\infty}^{\infty} a \frac{\exp(-y^2)}{(b-y)^2} dy \tag{4.33}$$

with

$$a = \frac{\delta_L}{\delta_D}\sqrt{\log(2)}$$
$$b = \frac{\lambda - \lambda_0}{\delta_D}\log(2) \tag{4.34}$$

4.3 COMPUTATION METHOD

A detailed line-by-line method was adopted to determine the radiant energy transport, performing a detailed calculation of the emission coefficient on a wavelength basis before integrating over the selected spectrum range.

The primary assumptions of the NEC calculation are that the plasma is homogeneous, isothermal and in local thermodynamic equilibrium. The first step for the

calculation of the spectral emission coefficient is the computation of plasma species composition at pressures and temperatures of interest. Composition was in particular determined by solving the Saha-Eggert mass law equation and taking into account Dalton's law for ideal gas, macroscopic charge neutrality and conservation of heavy species mass [86]. The temperature range was fixed between 3000 K and 25000 K, with pressure varying from 50 kPa to 200 kPa.

Fundamental data for energy levels e_i, statistical weight g_i, transition probabilities A_{ul} and lines, atomic configurations and oscillator strengths, were taken integrating the NIST [87] and Kurucz [88] databases. A total of 7065 emission lines was considered for the Ar neutral (Ar I), first and second Ar ions (A II and Ar III respectively) as shown in Tab 4.1.

Ar (Ar I)	**Ar^+ (Ar II)**	**Ar^{2+} (Ar III)**	**Total**
2412	4573	80	7065

Tab. 4.1 Lines considered for each specie in the computation of Ar NEC.

Spectral line emission coefficient was then calculated considering line and continuum emission.

Concerning the computation of continuum emission, electron-ion interactions were considered in terms of radiative recombination and braking radiation. For each ion, the Biberman factors for free-bound and *bremsstrahlung* continuum were taken from Schlueter [89] and Hoafsess [76, 77]. Crude linear interpolation was used to determine Bibmernam factors for missing temperatures and wavelengths, while the influence of pressure was considered as negligible.

Doppler, resonance and Stark broadening effects were considered for each auto-absorbed line to compute its perturbed profile. The determination of Stark parameters is rather complex, difficulties lying not only in the precision of the various models used to compute the FWHE, but also in the lack of spectroscopic data, in particular concerning the collisional broadening. Therefore, when the oscillator strengths for Stark effect were missing, empirical relationship between the broadening parameters and the spectroscopic level configurations for Ar as described by Trassy [90] was used,

although with a correction factor taking into account the dependence on electron density, as suggested in [81].

Lorentzian and Gaussian profile were finally convoluted to a Voigt profile by means of the approximate approach introduced by Whiting [91], in the form proposed by Menart et al in [70].

Integrating the spectral emission coefficient over the selected wavelength spectrum (0.03 – 25 μm), for every temperature and every pressure of interest, volumetric emission coefficient (i.e. NEC for a optically thin plasma) was estimated at different pressures and temperatures. Once the emission spectrum of the optically thin Ar plasma, comprising broadened lines, was computed, the spectral absorption coefficient K_λ was determined. NEC at different plasma thickness R (or line-of-sight L) was finally calculated. Species and emission mechanisms fractional contribution to the net emission coefficient of Ar plasmas were determined. The effects of pressure were shown. Results were compared with published data, both for the optically thin and partially absorbed Ar plasma at 10 cm and 100 cm plasma thickness.

4.4 Results and discussion

Fig. 4.5 shows plasma composition at 50 kPa, 100 kPa and 200 kPa. As obvious, species concentration generally increases with increasing pressures and ionization degree increases with temperature.

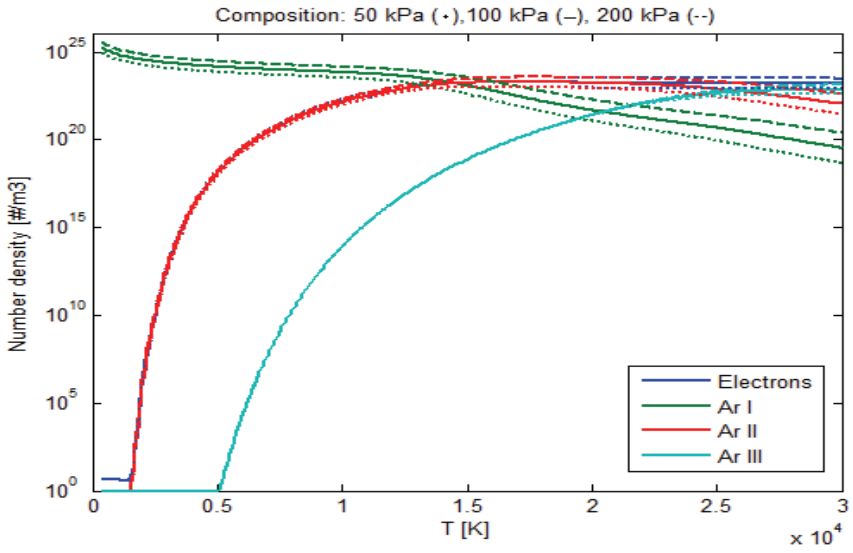

Fig. 4.5 Ar plasma composition at different pressures.

Internal partition functions are reported in Fig. 4.6 in the case of atmospheric pressure. In order to validate calculations with respect to the ones reported by NASA in [92], partition function were computed for neutral Ar and its first three ions.

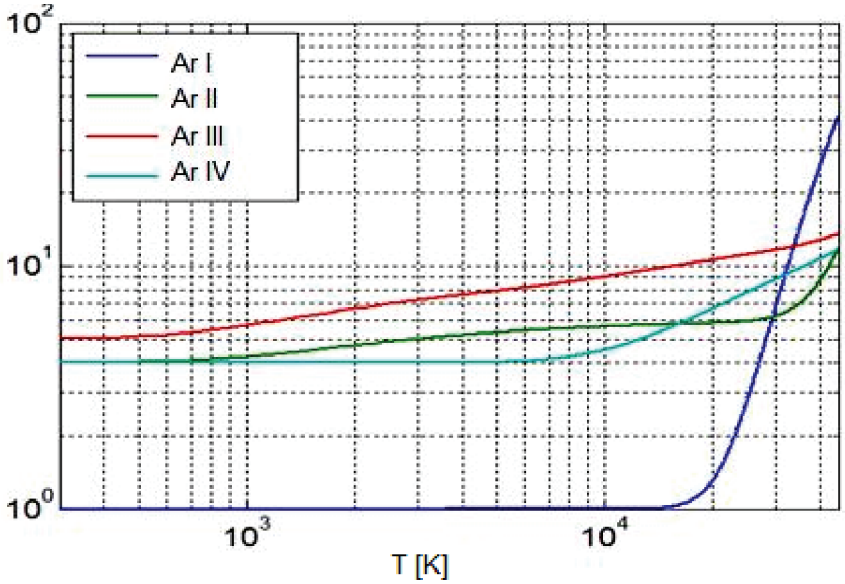

Fig. 4.6 Internal partition function for Ar I – Ar IV at 100 kPa.

Fig. 4.7 shows the normalized emission coefficient ($\varepsilon_{L_{ul}}(\lambda)/\varepsilon_{L_{ul}}^{\max}$) up to 30000 K as computed for two lines, selected among the 7065 considered in the present model. Good agreement was found with the ones measured in [93].

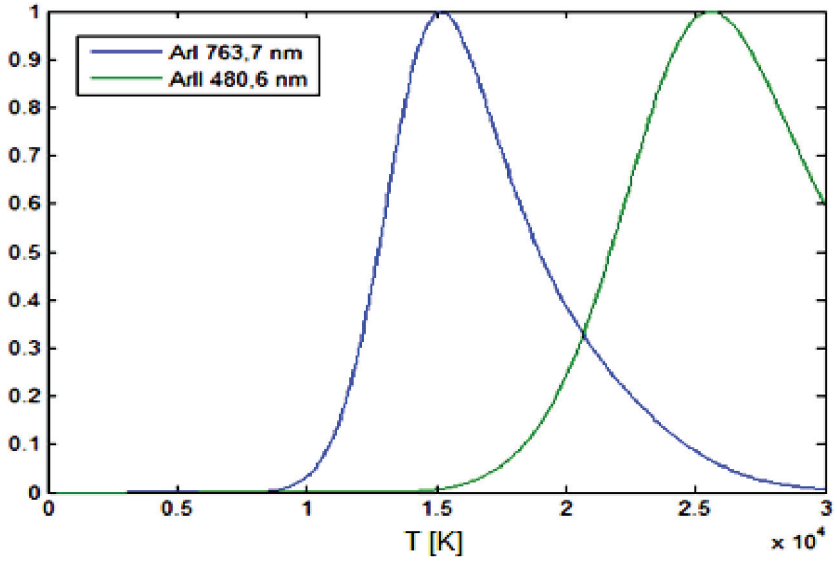

Fig. 4.7 Relative emission coefficient of selected Ar I and Ar II lines at 100 kPa. The reported wavelengths represent the respective line centres.

The contribution of different species to line emission at atmospheric pressure is reported in Fig. 4.7. By also observing the fractional contribution of Fig. 4.9, one can notice that line emission of the first ion (Ar II) starts to be preponderant from about 17000 K, whereas the contribution second ion (Ar III) starts to be significant only over 25000 K. Line emission for optically thin plasma at different pressures is reported in Fig. 4.10.

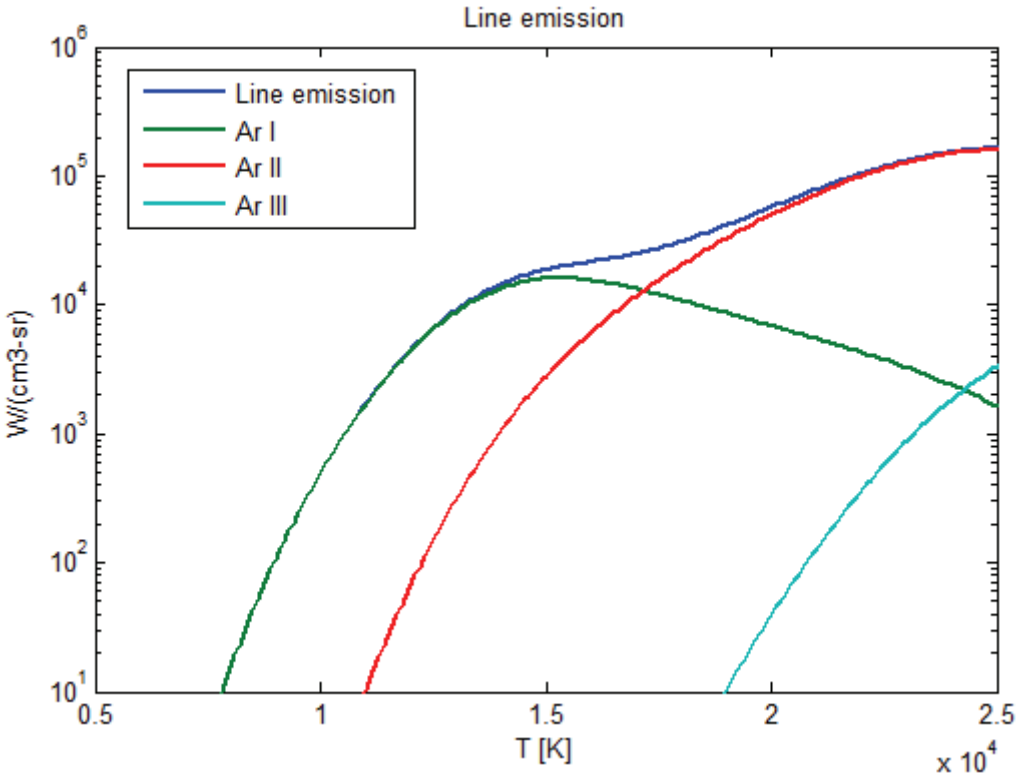

Fig. 4.8. Line emission at atmospheric pressure (100 kPa) with contribution of different species.

As already mentioned, only electrons interactions with ions were considered for continuum emission, while *free-bound* radiative attachment and braking radiation due to interaction with neutrals were neglected. Fig. 4.9 shows the fractional contribution of Ar II and Ar III for the two emission mechanisms, highlighting in both cases that the second ion has a greater effects starting from about 24000 K. The radiative recombination gives the main contribution to the total continuum emission, being more than one order of magnitude higher than braking radiation, with a maximum at 15000 K, with respect to the temperature range considered (Fig. 4.10). *Bremsstrahlung* increases its fractional contribution at increasing temperature (Fig. 4.11). At 25000 K,

by doubling the plasma pressure, continuum emission increases of a factor of about 2.7 from 50 kPa to 100 kPa and of about 2.6 from atmospheric pressure to 200 kPa.

Summing the line and continuum contribution, the spectral emission coefficient ε_λ at every temperature and pressure of interest was determined.

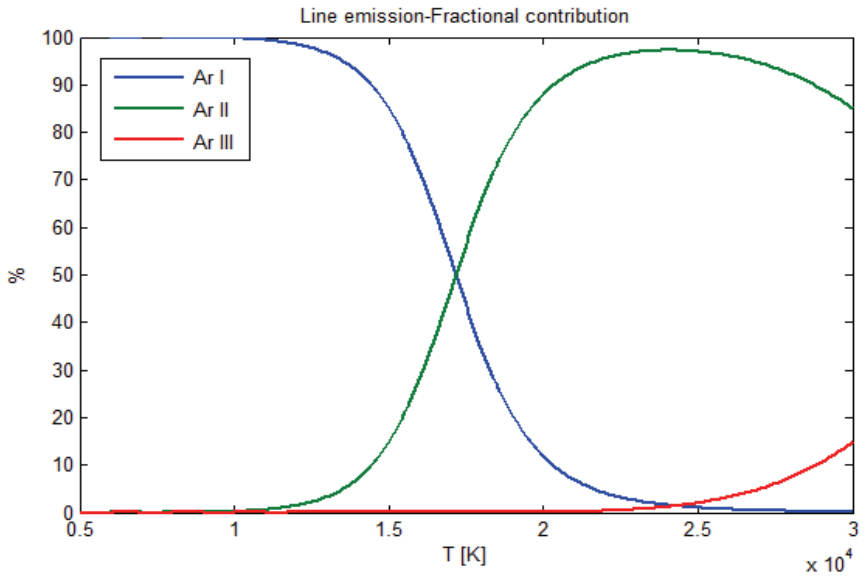

Fig. 4.9. Line emission: species fractional contribution at 100 kPa.

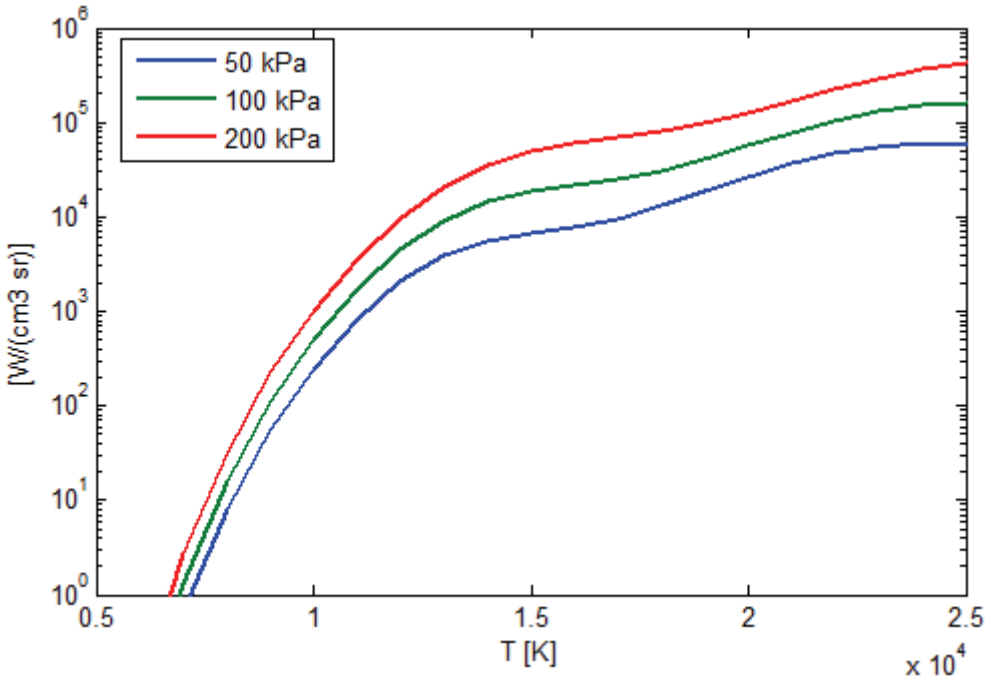

Fig. 4.10 Volumetric line emission emission at different plasma pressures.

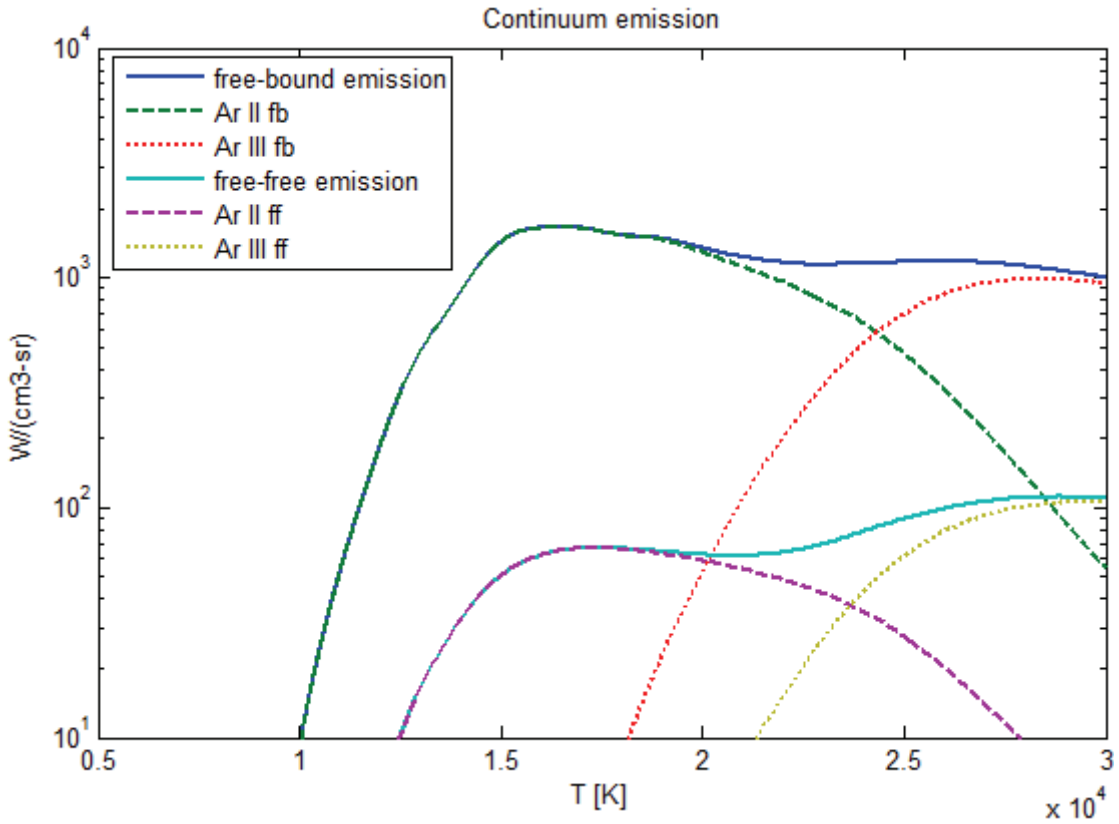

Fig. 4.11 Continuum emission due to *free-bound* and *free-free* transitions (p = 100 kPa).

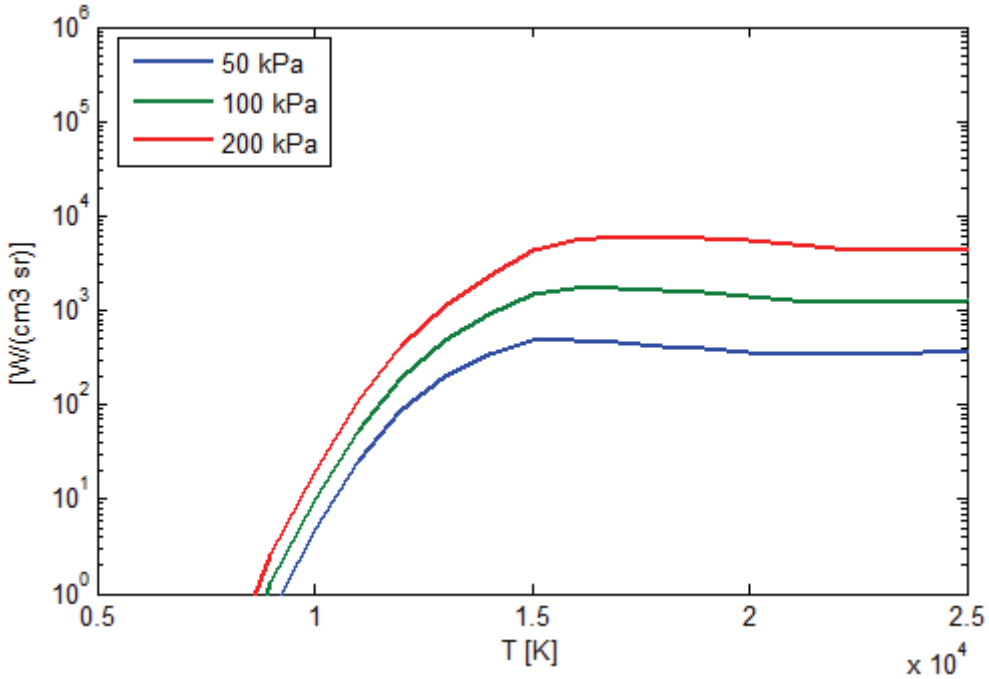

Fig. 4.12 Total continuum emission at different pressures.

By way an example, a spectrum computed with the present model for an Ar plasma at 14000 K and atmospheric pressure in given in Fig. 4.13. The reader be advised that the resolution of the image is not sufficient to resolve the 7065 lines considered. There is a negligible amount of radiant power below 30 nm and above 25 μm. The background of continuum emission can be identified underneath the line emission peaks.

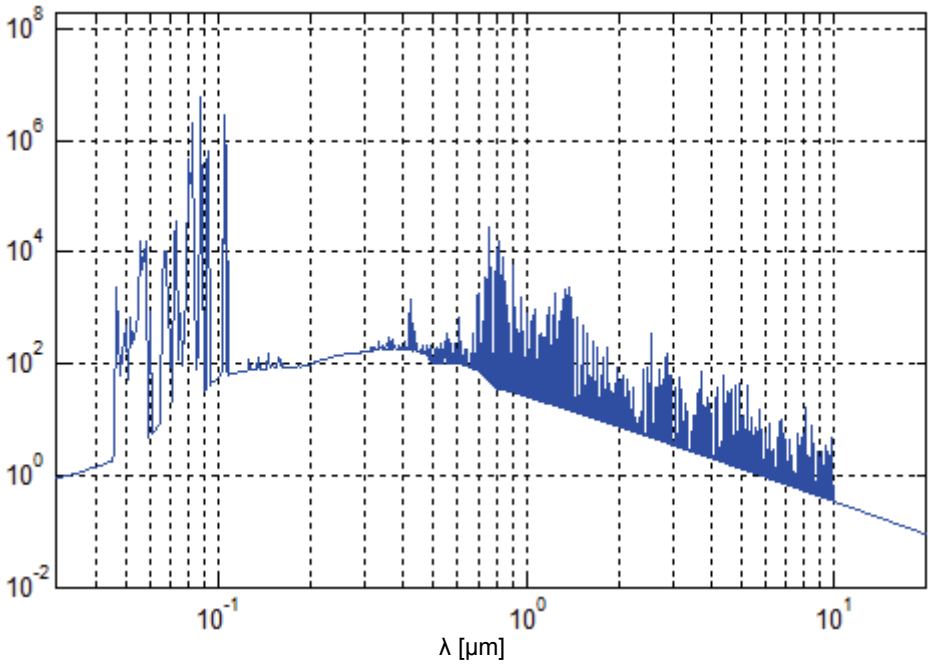

Fig. 4.13 Ar plasma spectral emission coefficient at 14000 K, 100 kPa.

By integrating ε_λ, the volumetric emission coefficient (W/cm^{3}sr) for Ar plasma was calculated according to Eq. 4.12, by imposing the plasma thickness L (or plasma radius R) equal to 0 for optically thin plasmas, as it is the case for Fig. 4.14. The main contribution to total emission is given by far by line emission, as highlighted in the analysis of Fig. 4.15. At temperatures ranging from 5000 K to 25000 K continuum emission (due to free-bound transitions) does not contribute more than 7% to the total volumetric emission, in perfect agreement with data reported in [71]. The contribution of *bremsstrahlung* to the total emission is negligible.

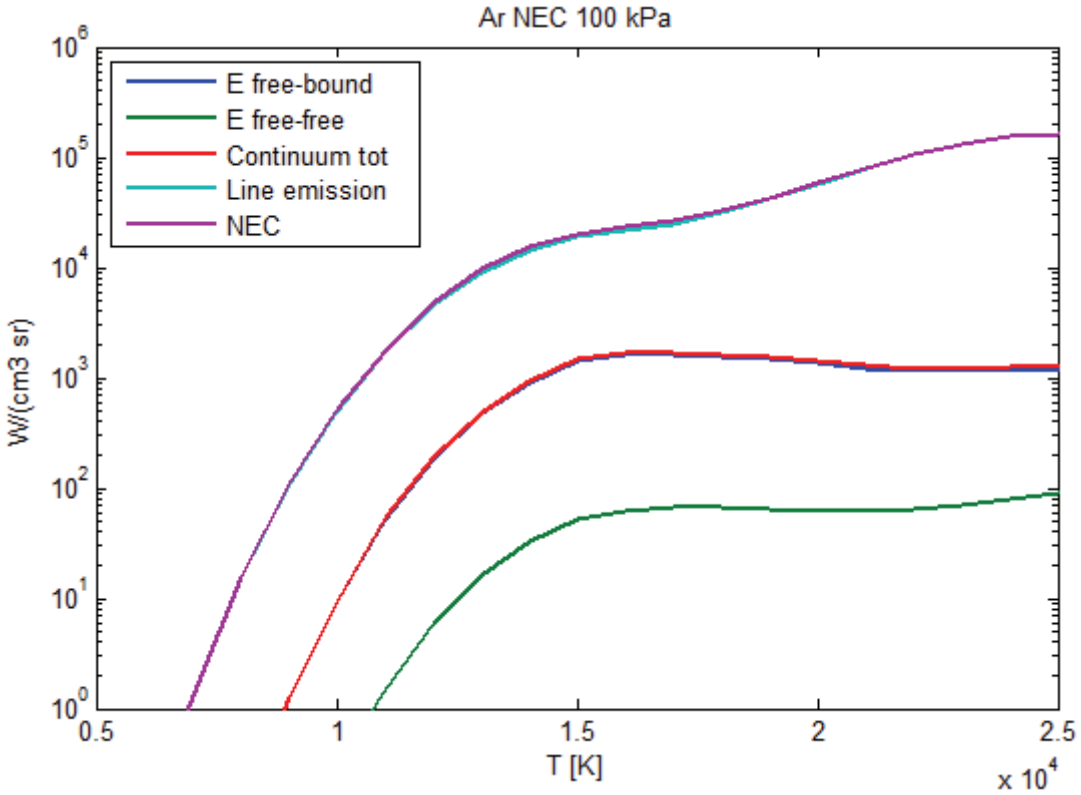

Fig. 4.14 Total volumetric emission coefficient with different mechanisms' and species contribution.

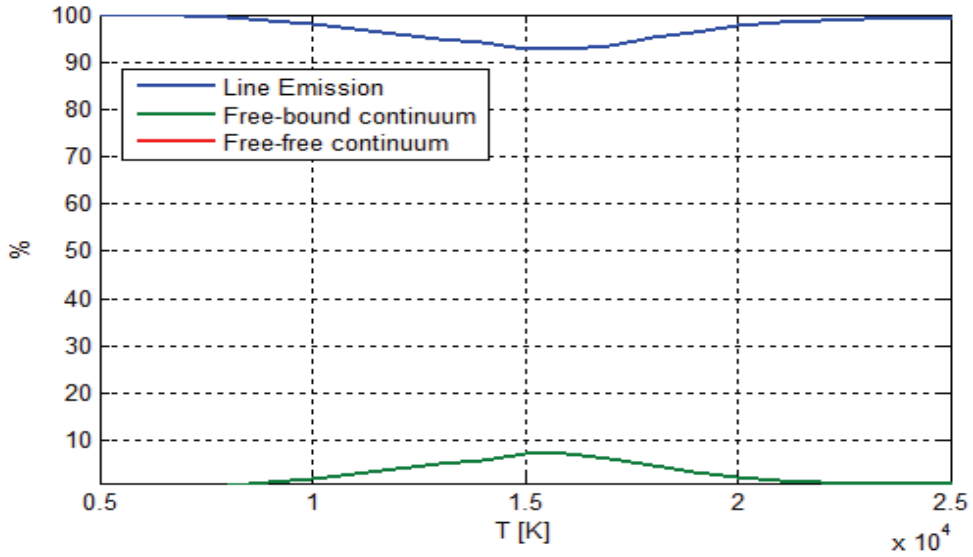

Fig. 4.15 Fractional contribution of the different emission mechanisms to the volumetric emission coefficient for an Ar plasma at 100 kPa.

The effect of pressure on total emission is shown in Fig.s 4.16-4.18. The higher particle densities implies, as expected, an increase in the emission coefficient both in the optically thin and partially absorbed Ar plasma.

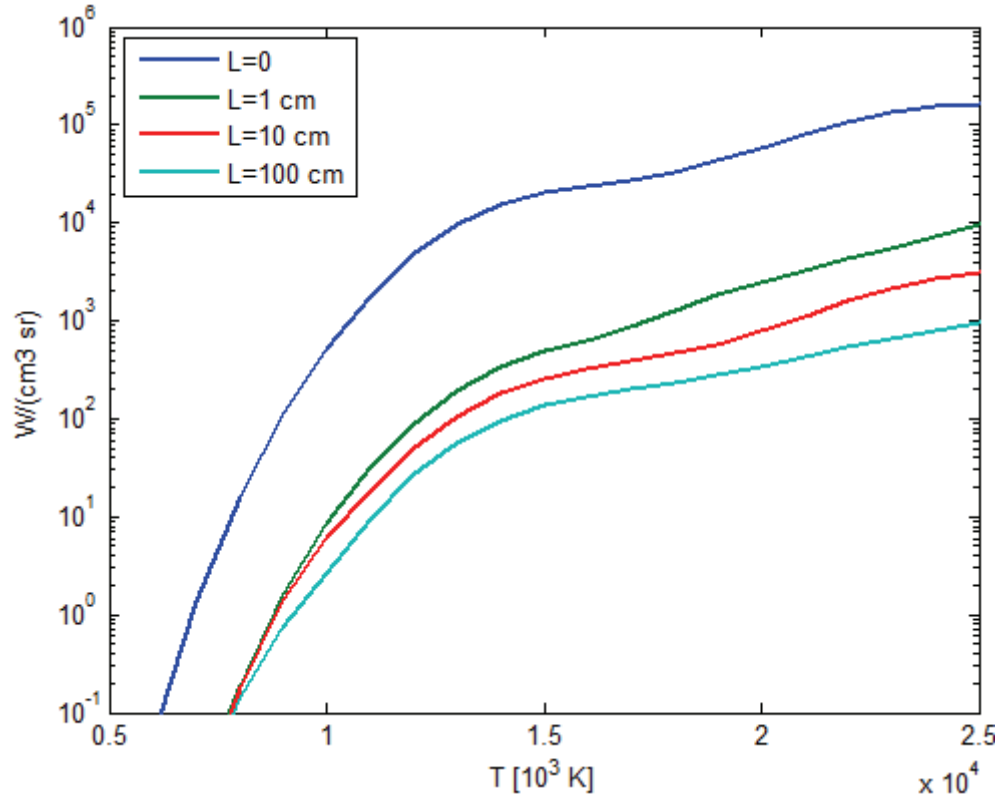

Fig. 4. 16 NEC of Ar plasmas for at different plasma thicknesses, 100 kPa.

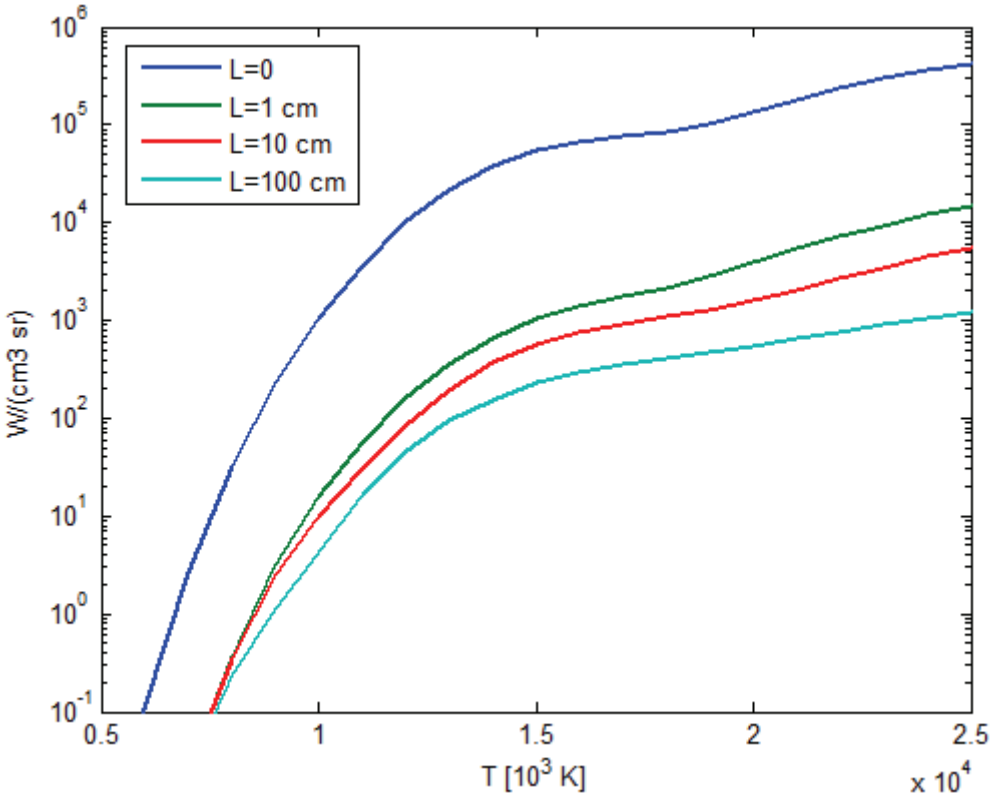

Fig. 4. 17 NEC of Ar plasmas for at different plasma thicknesses, 200 kPa.

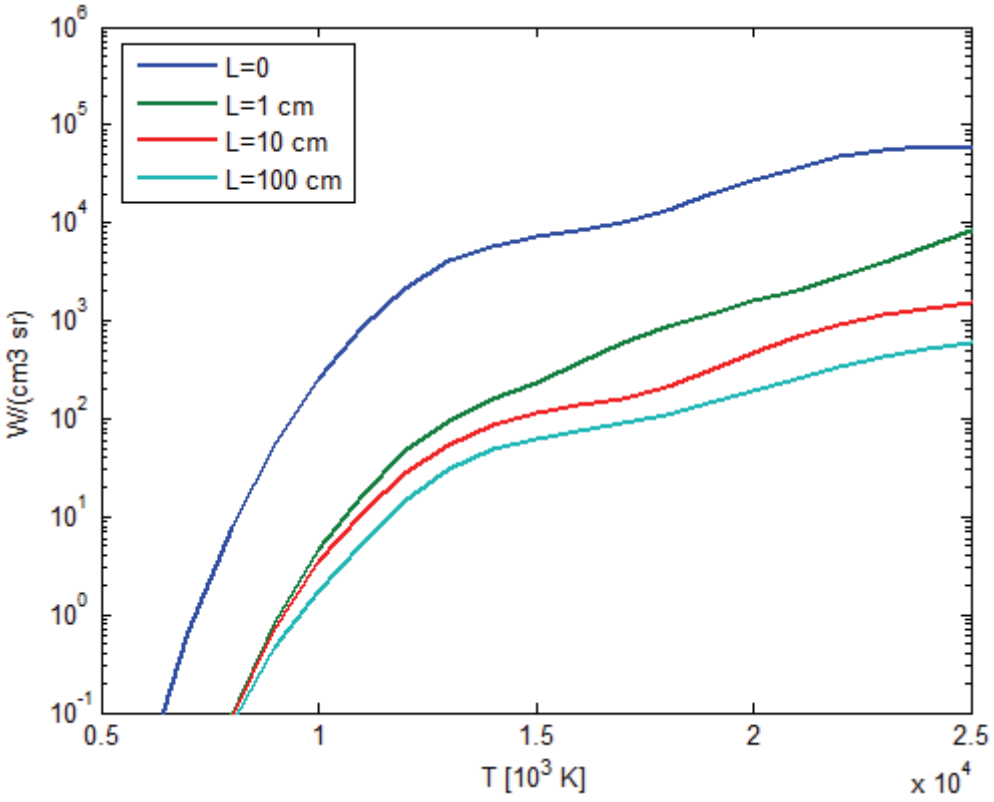

Fig. 4. 18 NEC of Ar plasmas for at different plasma thicknesses, 50 kPa.

As previously mentioned, although Ar plasmas have been widely studied, measurements of optically thin emission coefficients have been accomplished only over a portion of the spectrum. This is due to the fact that a method to measure the vacuum ultraviolet portion of the spectrum is not known [68]. However, Evans and Tankin (1967) [69] managed to measure the optically thin emission coefficients for argon in the 0.2–3.5 μm spectrum range. The model described in this work was compared with the measurements of Evans and Tankin and model of Menart et al [70], by imposing the corresponding spectrum range in the high temperature region. Excellent agreement was obtained with theoretical data of 74, with only slight differences between 15000 K and 20000 K, possible due to the use of different atomic data sources (Fig. 4.19). reasonably, the experimental data are slightly lower than computed ones, as in experimental measurements the optically thin conditions cannot actually be achieved due to the impossibility of getting completely rid of auto absorption.

Interestingly, one can observe that the fractional contribution of different emission mechanism significantly change in the restricted spectrum range. The

contribution of continuum exceed in this case 50% at 17000 K, with a relevant portion of *bremsstrahlung* emission (Fig. 4.20).

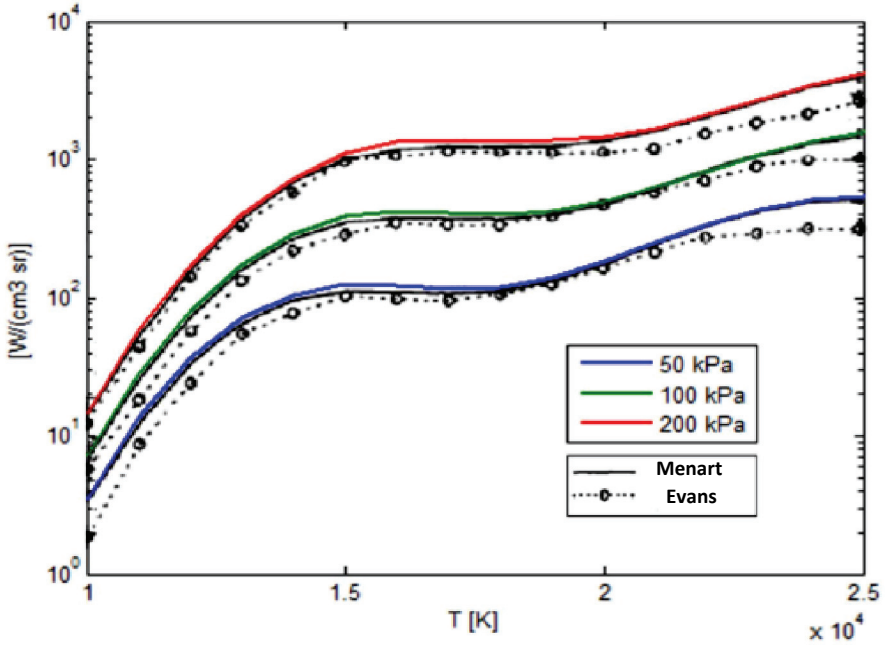

Fig. 4.19 Volumetric emission at different pressures for wavelength range 0.2-3.5 μm and comparison with [69, 70].

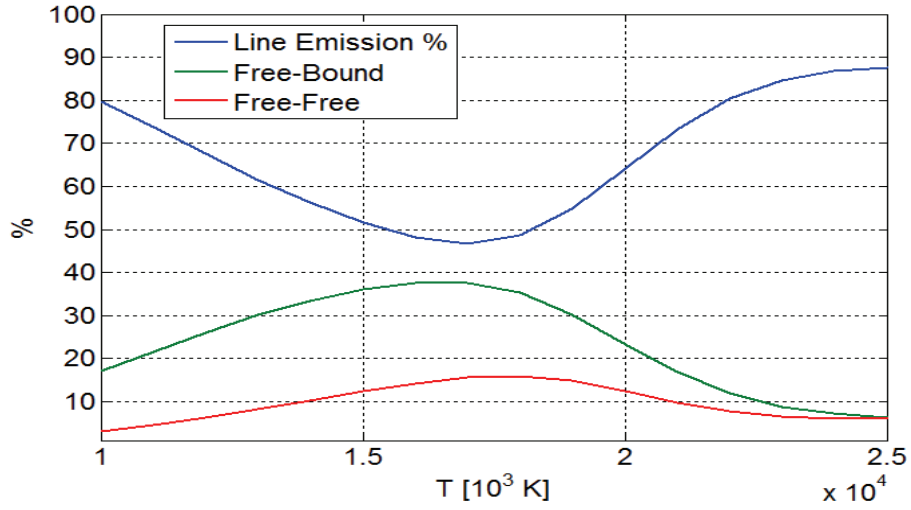

Fig. 4.16 Fractional contribution to volumetric emission for λ=0.2-3.5.

Fig. 4.21 finally reports the total emission coefficient and net emission coefficient at R=10 and 100 cm, according to the present model and in comparison with the work of Menart and Malik [68].

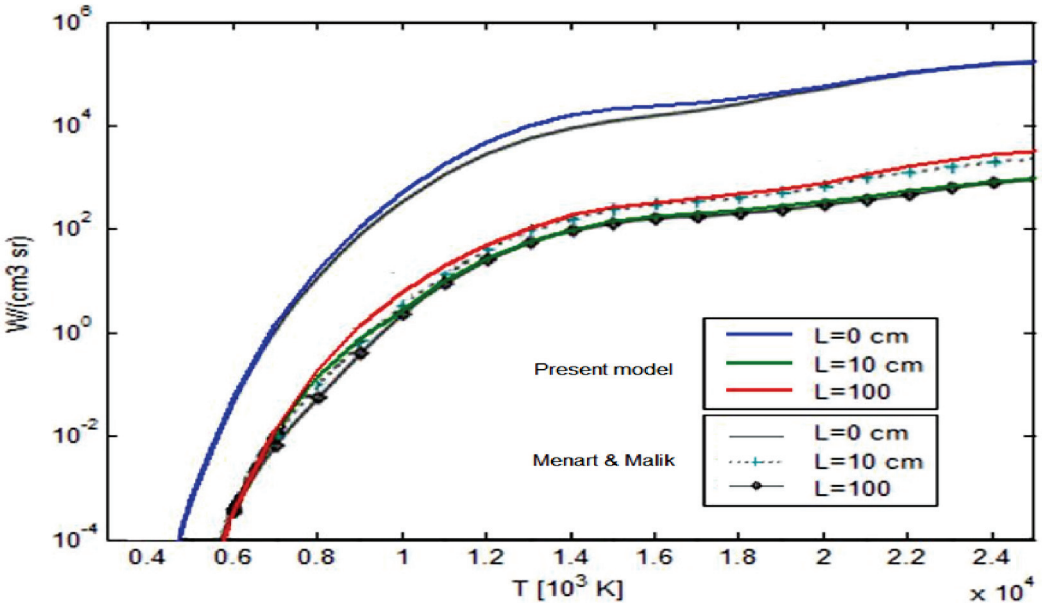

Fig, 4.21 Volumetric emission coeffient and NEC at atmospheric pressure and comparison with [68]

Slight differences in the relative contribution of the free-free and free-bound continuum mechanism are attributed to uncertainties concerning the different Biberman factors and the use of different databases for fundamental atomic data.

CONCLUSIONS

The emission coefficient of Ar plasmas was computed by means of a detailed line-by-line method in the 3000 K - 25000 K temperatures range and 50 kPa – 200 kPa pressure range. The absolute and relative contribution of considered species (Ar neutrals and first two ions) and emission mechanisms contribution on the volumetric emission coefficient were analysed for optically thin and partially auto-absorbed plasmas. The computed code is suitable for performing calculation of the net emission coefficient at different plasma thickness by considering the absorption over the entire spectrum.

At temperatures ranging from 5000 K to 25000 K free-bound continuum emission contributes at maximum with 7% of the total volumetric emission, while the contribution of *bremsstrahlung* to the total emission is negligible.

Results obtained from the present model compare favourably to published theoretical and experimental data, although some discrepancies exist, possibly related to the use of different data sources.

Future works could include the study of the influence of metallic vapour and the investigation of the feasibility of using the NEC model to compute the radiative source term in non-equilibrium plasmas.

CONCLUSIONS

Consumables components for high definition plasma arc cutting (PAC) torches were studied and developed in the first part of the present thesis. Experimental activities have in particular focussed on the modifications of the emissive insert with respect to the standard electrode configuration, comprising a press fit Hf insert in a copper body holder, with the final aim of improving its endurance performances. Different solutions were proposed and tested on the basis of both scientific and patent literature, which was analysed in the first Chapter.

In the second Chapter, the behaviour in oxidizing atmosphere of high current (250 A) electrodes in plasma arc cutting were investigated by means of morphological analysis during first cycles. An iterative experimental procedure for the optimization of the initial recess shape of the Hf insert was proposed and validated: starting the investigation with an initially plane emission surface, subsequent optimization steps are defined on the basis of the evolution of the recess depth naturally created during the first few *CCs*.

Experimental evidences showed that an initial planar emission surface gives rise to massive Hf ejections during first *CCs*, inducing a preferred concave shape on the emitter. The resulting massive Hf deposition on the inner nozzle surfaces negatively affects cut quality and nozzle service life. The modified experimental procedure was used to demonstrate that the optimization of the initial recess shape of the Hf emitter surface not only minimizes the deposition of HfO_2 on the nozzle but positively affects the subsequent trend of the Hf erosion rate, improving the electrode's service life on the whole.

In the same Chapter, the microstructural modifications occurring in hafnium (Hf) cathodes during first PAC cycles, operating at high current level in oxidizing atmosphere, were experimentally investigated and interpreted also by means of

thermodynamics and kinetics of the Hf high temperature oxidation. Microstructural analysis, including Raman spectroscopy, optical and electron scanning microscopy on the electrodes surface and cross section, allowed the identification of three typical zones in the insert after cutting: monoclinic HfO_2 layer; remelted transition zone with O_2-Hf solid solution; unmodified Hf. The erosion cavity and the oxide layer thickness were found to increase with the number of cutting cycles. Macrocracking was observed in the oxide layer, while microcracking and grain growth were detected in the remelted Hf. Detrimental detachment, worsening the heat dissipation and accelerating oxidation and erosion phenomena, was found at the Hf/Cu interface.

The analyses of the deposited HfO_2 morphologies confirmed that massive emissive material ejections occur both during the arc-on and arc-off transient phases. The action of convective forces due to Marangoni effect probably contributes to deepen the erosion cavity with increasing cutting cycles.

Finally, since the oxide layer thickness was found to increase with the number of cutting cycles, it is suggested the use of different current ramp at subsequent erosion stages, as to avoid thermal shocks which would possibly break the brittle oxide layer.

The work presented in Chapter III was aimed at producing, characterizing and testing prototypes of composite inserts, combining powders of a high thermal conductibility (Cu, Ag) and high thermionic emissivity (Hf, Zr) materials, to achieve better electrode durability. The results presented demonstrated the feasibility of using composite inserts comprising high conductivity material such as Cu or Ag and a high emissivity material, such as Zr or Hf, to produce PAC electrodes inserts. The small number of prototypes did not allow to draw a reliable evaluation concerning the effective performance of such electrodes with respect to traditional pure Hf inserts. Nevertheless, the erosion tests, together with microstructural and HSI analysis, suggested that the potential of such electrodes has to be considered for industrial applications, although further experimental testing would be required.

Concerning the modelling of physical phenomena occurring in the thermal plasma environment, a detailed line-by-line method was developed to compute the net emission coefficient of Ar plasmas at temperatures ranging from 3000 K to 25000 K and pressure ranging from 50 kPa to 200 kPa, for optically thin and partially auto-absorbed plasmas, as described in Chapter IV. It was found that, at temperatures ranging from 5000 K to

25000 K, free-bound continuum emission contributes at maximum with 7% of the total volumetric emission, while the contribution of bremsstrahlung to the total emission is negligible.

The results obtained with the described model compare favourably with published theoretical and experimental data, although some discrepancies exist, possibly related to the use of different data sources. Future works could include the study of the influence of metallic vapour.

APPENDIX

PROTOTYPAL COMPONENTS FOR AN ATMOSPHERIC PRESSURE NON-THERMAL PLASMA SOURCE

INTRODUCTION

Since the past two decades, considerable efforts have been dedicated by the scientific community to the development Atmospheric Non-Thermal Plasma (ANTP) sources. In NTPs, the collisional regime between electrons and heavy species is characterized by low impact frequencies and/or energies, so that the plasma ions and neutrals remain at or near room temperature. Being the electrons' temperature higher than that of heavy species, NTPs are classified as non-equilibrium plasmas. With respect to the widely studied low pressure NTP, ANTPs do not require any expansive equipment for attaining a controlled low pressure environment.

Atmospheric Non-Thermal Plasma may be obtained by a diversity of electrical discharges, generated under a wide range of driving frequencies and with various electrode configurations [94-97]. Significant examples include corona discharges, atmospheric pressure plasma jets and dielectric barrier discharges.

Further than a strong thermodynamic non-equilibrium nature and low gas temperature, characteristic features of "cold" plasma include the presence of highly reactive chemical species and a high selectivity. Since ions and the neutrals remain near room temperature, ANTPs are attractive candidates for the treatment of heat sensitive materials such as polymers and biological tissues.

In particular, some non-thermal (cold) plasma treatments have been recently indicated as potential breakthrough biomedical applications in biology and medicine. Relevant examples of medical applications of plasmas are represented by the treatment

of dental cavities and skin diseases, wound healing, induced apoptosis of cancerous cells in vivo and in vitro [98, 99]. Thanks to the synergic action of several mechanisms, including the UV radiation, electric field, charged particles, and generated radicals, cold plasma generated by electrical discharges can be employed for bio-decontamination and sterilization of various surfaces, such as medical instruments, water, air, food and even living tissues without collateral damages [99, 100].

However, a deeper understanding of the mechanisms of interaction of non-equilibrium gas discharges with substrates in the different plasma treatments is necessary, in particular to satisfy the stiff requirements of medical treatments. A key step in this direction is the development plasma sources optimised to control crucial treatment parameters.

For the above mentioned reasons, a novel multi-gas non-thermal plasma device has been recently developed by the Plasma Research Group at the University of Bologna. Although the characterization of the source is in progress at the time this thesis is being completed, a brief presentation of some of its components and features is given in this appendix.

UNIBO PLASMA NEEDLE

The novel plasma source is devoted to the generation of non-thermal radio-frequency plasmas at atmospheric pressure. It is based on the plasma needle concept [101], although with an advanced configuration. Relevant features of this type of plasma source comprise the possibility of operating at or near room temperature and to treat irregular surfaces.

Fig. A1. Rendering of the Unibo plasma needle.

The Unibo plasma needle comprises a tubular thermoplastic holder hosting gas and electrical supplies. The configuration and dimensions of the source were optimized to improve the ease of handling, in order to allow precise treatments operations. A render of the torch body is given in Fig. A1.

One of the specific feature of the described plasma needle is that the treatment can be performed at controlled distance from the substrate. A protection shield allows the plasma products to flow towards the treated substrate, while avoiding the contact of this substrate with the electrode tip for safe operations mode (Fig. A2). Moreover, primary gas flow, in which the plasma is ignited, and secondary gas flow, impinging on the plasma forming region as to benefit from its ionizing action, can be independently controlled. Such a design configuration allows the decoupling of the process of plasma formation from the production of reactive species as to optimize their composition. Primary plasma gases include argon and helium.

Fig. A2. Example of treatment with the Unibo plasma needle.

The needle electrode is supplied with high voltage generators capable of producing nanosecond and microsecond pulses. The electrode comprises a 0.3 mm stainless steel wire and it is inserted in a Pyrex capillary tube, which allows to localize the plasma formation on the protruding needle tip, as shown in Fig. A3. In a second embodiment, the body of the needle-like electrode is electrically insulated by means of an irradiated polyolefin heat shrinking tube. The treated substrate acts as a floating electrode. The

length of the protruding plasma jet can be varied depending upon voltage, frequency and gas flow supplies.

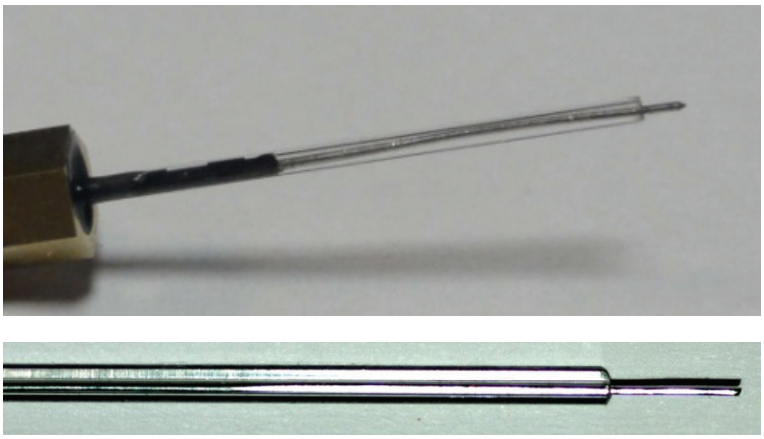

Fig. A3. Prototypal needle electrode.

FUTURE WORKS

Different diagnostic methods will be used to investigate plasma behaviour in terms of gas temperature, heat flux, effluent chemical composition and fluid dynamics, for different flow combination of primary and secondary gas and varying the operative conditions of the plasma source. Diagnostic methods will include time-resolved emission spectroscopy and Schlieren photography.

Once a complete characterization will be accomplished, the effects of the different treatment parameters on biological, polymeric and various inorganic substrates will be studied.

REFERENCES

1. M.I. Boulos, P. Fauchais, E. Pfender. Thermal Plasmas - Vol. 1: Fundamentals and Applications. New York : Plenum Press, 1994.
2. V.A. Nemchinsky, W.S. Severance, J. Phys. D: Appl. Phys. 39 (2006) R423-R438.
3. P. Freton, Ph.D. Thesis, Universite Paul Sabatier, Toulouse III, 2002.
4. ISO 9013:2002(E)
5. D.R. Lide (Ed.), CRC Handbook of Chemistry and Physics, CRC Press, Boca Raton, 2009, p.4-97.
6. D.Eastman, Phys. Rev B, 2 (1) (1970) 1-2.
7. R.T. Webster, in: Properties and Selection: Nonferrous Alloys and Special-Purpose Materials, Vol. 2, ASM Handbook, ASM International, 1990, pp. 661–669.
8. D.R. Holmes in: S.D. Cramer, S. Bernard, Jr. Covino (Eds.), Corrosion: Materials (ASM Handbook: Volume 13B), ASM International, 2005, pp.354-359.
9. V. Colombo, A. Concetti, E. Ghedini, S. Dallavalle, M. Vancini, Plasma Sour. Sci. Tech. 18(2) (2009) 023001.
10. V.A. Nemchinky, N.Ya. Moizhes, Sov. Phys.-Tech. Phys. 18 (1973) 1460–4.
11. V. A. Nemchinsky, J. Phys. D: Appl. Phys. 36 (2003) 1573-1576.
12. J. Peters, F. Yin, C.F.M. Borges, J. Heberlein, C. Hackett, J. Phys. D: Appl. Phys. 38 (2005) 1781-1794.
13. X. Zhou, J. Heberlein, Plasma Sources Sci. Technol. 3 (1994)564–74
14. V. A. Nemchinsky, M.S. Showalter, J. Phys. D: Appl. Phys. 36 (2003) 704-712
15. B.Y. Moizhes, V.A. Nemchinsky, Sov. Phys.-Tech. Phys. 29 (1984) 612–6
16. P. Tzantrizos W.H. Gauvin, Plasma Chem. Plasma Process. 12 (1992) 17–33
17. A. Marotta, J. Phys. D: Appl. Phys. 27 (1994) 49–53
18. W. Neumann, Beitr. Plasmaphys. 9 (1969) 499–526
19. M. S. Benilov, A. Marotta, J. Phys. D: Appl. Phys. 28 (1995) 1869-1882

20. M.F. Zhukov, F. Kozlov, A.V. Pustogarov, A.S. Anshakov, V.I. Khvesuk, G.A. Gjuzhev, G.-N. B. Dandaron, Near-Electrode Processes in Arcs (Novosibirsk. Nauka) (1992)

21. R. Gage, Union Carbide corp. patent US 2,806,124 (1955)

22. H. Weatherly Merle, Union Carbide corp. patent US 3,198,932 (1964)

23. O. Toshihiko, U. Masanobu, Daihen corp. patent US 5,200,594 (1993)

24. D. G. Bykhovsky, A. Y. Medvedev, Y. V. Rossomakho, V. A. Koss, patent US 3,546,422 (1970)

25. D. G. Bykhovsky, A. Y. Medvedev, patent US 3,597,649 (1971)

26. G. Bykhovsky, A. Y. Medvedev, Y. V. Rossomakho, M.N. Butova, patent US 3,930,139 (1975)

27. G. Bykhovsky, A.I. Danilov, M.S. Brodsky, patent US 3,944,778 (1976)

28. J. Johansson, J.-E. Andersson, T. Niklewski, L.E. Edshammar ,Aga AB patent US 4,766,349 (1988)

29. W.S. Severance Jr., Esab Group Inc. patent EP 437915 (1992)

30. W.S. Severance Jr., Esab Group Inc. patent US 5,097,111 (1993)

31. A.W. Marner, W.S. Severance, L.W. Stokes, T.Z. Turner, R.AL. Rue Allen, V. Nemchinsky, Esab Inc. patent US 6,020,572 (2000)

32. A.W. Marner, W.S. Severance, L.W. Stokes, T.Z. Turner, R.AL. Rue Allen, V. Nemchinsky, Esab Inc. patent EP 0980197 (2003)

33. T. Okada, M. Uchida, H. Fujiwara, Daihen Corp. patent US 5,200,594 (1992)

34. T. Okada, M. Uchida, H. Fujiwara, Daihen Corp. patent EP 0465109 (1992)

35. R.W. Couch, N. Sanders, L. Luo, Z. Lu, P. Baeckander, J. Sobr, Hypertherm Inc. patent US 5,310,988 (1994)

36. R.W. Couch Jr., N. Sanders, L. Luo, Z. Lu, P. Baeckander, J. Sobr, Hypertherm Inc. patent EP 0641269 (1994)

37. R.W. Couch Jr., L. Luo, Hypertherm Inc. patent US 5,464,962 (1995)

38. R.W. Couch Jr., L. Luo, Hypertherm Inc. patent EP 0772957 (1994)

39. V. Nemchinsky, Esab Group Inc. patent US 6,066,827 (2000)

40. L. Luo, R.W. Couch, Hypertherm Inc. patent US 6,130,399 (2003)

41. L. Luo, R.W. Couch, Hypertherm Inc. patent EP 1099360 (2003)

42. M.C. Mcbennett, Esab Group Inc. EP 1263268 (2002)

43. W.S. Severance Jr., V. Nemchinsky, G.W. Diehl, Esab Group Inc. patent US 6,563,075 (2003)

44. W.S. Severance Jr., V. Nemchinsky, G.W. Diehl, Esab Group Inc. patent EP 1322144 (2003)

45. Y. Yamaguchi, K. Kuraoka, T. Kabata, Komatsu Ind Corp. patent US 6,583,378 (2003)

46. V. Krink, F. Laurisch,W. Moehler G. Lotze, H. Loebl, Kjellberg Inc. Patent EP 1481574 (2004)

47. V. Krink, F. Laurisch,W. Moehler G. Lotze, H. Loebl, Kjellberg Inc. Patent US 7,098,422 (2007)

48. D.J. Cook, K.H. Ferland, C.M. Hackett, Y. Yang, R.W. Couch Jr, Z. Lu, Hypertherm Inc. patent US 7,659,488 (2006)

49. D.J. Cook, K.H. Ferland, C.M. Hackett, Y. Yang, R.W. Couch Jr, Z. Lu, Hypertherm Inc. patent application EP 1369000 (2003)

50. J.P. Mather, D.J. Cook, D.L. Bouthillier, J. Sobr, S.T. Eickhoff, Hypertherm Inc. patent EP 1765046 (2005)

51. J.P. Mather, D.J. Cook, D.L. Bouthillier, J. Sobr, S.T. Eickhoff, Hypertherm Inc. KR 20080041731 (2008)

52. Gmelin Handbook of Inorganic and Organometallic Chemistry / Gesellschaft Deutscher Chemiker e.V. (GDCh), available from CrossFire Gmelin http://info.crossfiregmelin.com/, Elsevier Information Systems Gmbh, 2010/01

53. S. Sakuragi, Komatsu Ind Corp. patent US 5,214,263 (1990)

54. V. Colombo, A. Concetti, E. Ghedini, F. Rotundo, S. Dallavalle, Plasma Sour.Sci. Tech. 19(6) (2010) 065023.

55. Y. He, Z. Li, H. Qi, W. Gao, Materials Research Innovations 1(3) (1997) 157–160.

56. P.J. Spencer, O. von Goldbeck, R. Ferro, R. Marazza, K. Girgis, and O. Kubaschewski, in K.L. Komerek (Ed.): Hafnium: Physico-Chemical Properties of Its Compounds and Alloys, Atomic Energy Review Special Issue No.8, International Atomic Energy Agency, Vienna, 1981

57. M. Tanaka, K. Yamamoto, S. Tashiro, K. Nakata, E. Yamamoto, K. Yamazaki, K. Suzuki, A. B. Murphy and J. J. Lowke, J. Phys. D: Appl. Phys. 43 (2010) 434009.

58. V. B. Voitovich, V. A. Lavrenko, E. I. Golovko and V. M. Adejev, Oxidation of metals, 42(3) (1994) 249-263.

59. R. Ruh, V.A. Patel, J.Amer.Cer.Soc., 56 (11) (1973) 606-607.

60. International Centre for Diffraction Data (ICDD), Powder Diffraction File, 2002

61. J. Lowke,J. Quant. Spectrosc. Radiat. Transfer 14 (1974) 111

62. V. Aubrecht, J. Lowke, J. Phys. D: Appl. Phys. 27 (1994) 2066–73

63. J. Menart, J. Quant. Spectrosc. Radiat. Transfer 67 (2000) 273–91

64. V.G. Sevastyanenko, L. Gu, J. Bakken, Heat Trans. Soviet Res. 9 (1977) 36–41

65. G. Raynal, A. Gleizes, Plasma Sources Sci. Technol. 4 (1995) 152–60

66. Y. Naghizadeh-Kashani, Ph.D. Thesis, Universite Paul Sabatier, Toulouse III, 1999

67. V. Aubrecht, M. Bartlova, N. Bogatyreva, 29th International Conference on Phenomena in Ionized Gases (ICPIG), July 12-17, 2009, Cancún, México, PB11-1

68. J. Menart, S. Malik, J. Phys. D: Appl. Phys. 35 (2002) 867–874

69. D. L. Evans, R. S. Tankin, Physics of Fluids 10, 1137 (1967)

70. J. Menart, J. Heberlein, E. Pfender, J. Quant. Spectrosc. Radiat. Transfer 56, 3 (1996) 377-398

71. J. Menart, J. Heberlein, E. Pfender, Plasma Chem. Plasma Proc. 16, 1 (1996) 377-398

72. R.W. Liberman, J.J. Lowke, J. Quant. Spectrosc. Radiat. Transfer 16 (1976) 253-257

73. B. Rahmani, Ph.D. thesis, Univ. of Toulouse, 1989

74. F. Cabannes, J. Chapelle, Reactions under plasma conditions, 1, Chapter 7, Wiley-Interscience, 1971

75. A.T.M. Wilbers, G.M.W. Kroesen, C.J. Timmersmans, D.C. Schram, J. Quant. Spectrosc. Radiat. Transfer 45 (1991) 1-10

76. D. Hofsaess, At. Data Nucl. Data Tables 24 (1979) 285

77. D. Hohaess, Quant. Spectrosc. Radiat. 19 (1978) 339-52

78. D.G. Andrews, Atmospheric radiation. An Introduction to Atmospheric Physics, Cambridge University Press, 55–96, 2000.

79. H.R. Griem, Spectral line broadening by plasmas, Academic Press, New York, 1974

80. S. Djurovic, N. Konjevic, Plasma Sources Sci. Technol, 18 (2009) 035011

81. S. Hofmann, A.F.H. van Gessel, T. Verreycken, P, Bruggeman, Plasma Sources Sci. Technol. 20 (2011) 065010

82. C.Yubero, M.S. Dimitrijevic, M.C. Garcia, M.D. Calzada, Spectrochim. Acta B 62 (2007) 169–76

83. A. Essoltani, P. Proulx, M. I. Boulos, A. Gleizeset, Plasma Chem. Plasma Proc, 14, 3 (1994) 301-315

84. G. Traving, in W. Lochte-Holtgreven Plasma Diagnostics, New York: AIP Press, p 66, 1968

85. A. Bartecka, A. Baclawskia, T. Wujec, J. Musielok, Eur. Phys. J. D 37 (2006) 163–169

86. P. Sanibondi, Ph.D Thesis, Alma Mater Studiorum - University of Bologna, 2011

87. NIST atomic spectra database: http://www.nist.gov/pml/data/asd.cfm

88. R.L. Kurucz Atomic spectral line database: http://www.cfa.harvard.edu/amp/ampdata/kurucz23/sekur.html

89. D. Schluter, Z. Phys., 210 (1968) 82-91

90. C. Trassy, A. Tazeem, Spectroc. Acta Part B 54 (1999) 581-602

91. E. E. Whiting, J. Quant. Spectrosc. Radiat. Transfer, 8 (1968) 1369

92. T. E. Horton, NASA Jet Propulsion Laboratory, Technical Report 32- 1425, 1970

93. E. Pfender, "Diagnostic Techniques," in Continuing Education: Plasma Technology and Applh·ations, (2nd World Congress of Chemical Engineering and World Chcmical Montreal, 4-9 Oct., 1981).

94. M. Laroussi, T. Akan, Arc-Free Atmospheric Pressure Cold Plasma Jets: A Review, Plasma Process. Polym., 4 (2007) 777–788

95. E. E. Kunhardt, IEEE Trans. Plasma Sci., 28 (2000) 189.

96. U. Kogelschatz, IEEE Trans. Plasma Sci., 30 (2002) 1400.

97. U. Kogelschatz, Contr. Plasma Phys. 47 (2007) 80.

98. D. Dobrynin, G. Fridman, G. Friedman, A. Fridman, New Journal of Physics 11 (2009) 115020

99. NATO Advanced Research Workshop: Plasma for bio-decontamination, medicine and food security, Book of Abstracts edited by K. Hensel and Z. Machala, Jasná (Slovakia), March 15-18, 2011

100. J. Heinlin, G. Morfill, M. Landthaler, W. Stolz, G. Isbary, J. L. Zimmermann, T. Shimizu, S. Karrer, Journal of the German Society of Dermatology, 8 (2010) 1-9

101. E. Stoffels, A. J. Flikweert, W. W. Stoffels, G. M. W. Kroesen, Plasma Sources Sci. Technol. 11 (2002) 383